SANDIA REPORT
SAND2022-12249
Printed September, 2022

Sandia National Laboratories

Development of a Novel Electrical Characterization Technique for Measuring Hidden Joint Contacts in Weapons Cavities LDRD Final Report 218470

Jon W. Wallace, Ian J. Timmins, John J. Himbele, Isak C. Reines, Roy K. Gutierrez, Jeffery T. Williams

Prepared by
Sandia National Laboratories
Albuquerque, New Mexico 87185
Livermore, California 94550

Issued by Sandia National Laboratories, operated for the United States Department of Energy by National Technology & Engineering Solutions of Sandia, LLC.

Available to DOE and DOE contractors from

U.S. Department of Energy
Office of Scientific and Technical Information
P.O. Box 62
Oak Ridge, TN 37831

Telephone: (865) 576-8401
Facsimile: (865) 576-5728
E-Mail: reports@osti.gov
Online ordering: http://www.osti.gov/scitech

Available to the public from

U.S. Department of Commerce
National Technical Information Service
5301 Shawnee Road
Alexandria, VA 22312

Telephone: (800) 553-6847
Facsimile: (703) 605-6900
E-Mail: orders@ntis.gov
Online order: https://classic.ntis.gov/help/order-methods

This report summarizes research performed in the context of a REHEDS LDRD project that explores methods for measuring electrical properties of vessel joints. These properties, which include contact points and associated contact resistance, are “hidden” in the sense that they are not apparent from a computer-assisted design (CAD) description or visual inspection. As is demonstrated herein, the impact of this project is the development of electromagnetic near-field scanning capabilities that allow weapon cavity joints to be characterized with high spatial and/or temporal resolution. Such scans provide insight on the hidden electrical properties of the joint, allowing more detailed and accurate models of joints to be developed, and ultimately providing higher fidelity shielding effectiveness (SE) predictions. The capability to perform high-resolution temporal scanning of joints under vibration is also explored, using a multitone probing concept, allowing time-varying properties of joints to be characterized and the associated modulation to SE to be quantified.

CONTENTS

LIST OF FIGURES

LIST OF TABLES

GLOSSARY

1D	One-dimensional
2D	Two-dimensional
3D	Three-dimensional
AM	Amplitude modulation
AWG	Arbitrary waveform generator
CAD	Computer-assisted design
CEM	Computational electromagnetic(s)
CW	Continuous wave (unmodulated carrier)
DOE	Department of Energy
EIGER	Electromagnetic interactions generalized
EM	Electromagnetic(s)
GA	Genetic algorithm
GTEM	Gigahertz transverse electromagnetic cell
LDRD	Laboratory directed research and development
LNA	Low noise amplifier
LPF	Low-pass filter
mil	0.001 inches
MOM	Method of moments
PA	Power amplifier
PAR	Peak to average ratio
PB	Power balance
PEC	Perfect electrical conductor
PMC	Perfect magnetic conductor
POE	Port of entry
Q	Quality factor
RF	Radio frequency
RLC	Resistor, inductor, capacitor
SDR	Software-defined radio
SE	Shielding effectiveness
SMA	Sub-miniature version A connector
SNR	Signal-to-noise ratio
VNA	Vector network analyzer

1. INTRODUCTION

Metal enclosures are commonly used in electronic systems to prevent the transmission of electromagnetic radiation (EMR) either into or out of the system. One example is the battery system for an electric vehicle, where high current delivered from the main battery may produce strong fields that could interact with and impair nearby electronic devices [6]. Placing these high-current systems in metal shields can reduce the harmful electromagnetic interference (EMI) that would otherwise be radiated. As another example, in aerospace and military applications, sensitive avionics and weapon system components may malfunction due to external EMI, which could have catastrophic effects [3]. Although we focus in this report on modeling the EM shielding of weapon systems, where the goal is to minimize coupling of external EM energy into the system, the methods developed herein apply to many other shielding scenarios as well.

Weapon cavities typically consist of several cylindrical or conical sections that are separated by joints or seams. From a shielding perspective, a welded joint provides a continuous metal contact with nearly perfect shielding. However, welded joints can be problematic for inspection, maintenance, and repair. Figure 1-1 shows examples of common joints that allow for easy assembly and disassembly: a flange joint, a lap joint, and a threaded connection. Non-threaded connections, such as lap and flange joints, may be held together by fasteners (bolts or rivets), or they may use compression fittings. A common characteristic of all non-welded joints is that small gaps or seams are present, referred to herein as ports of entry (POEs). These gaps allow coupling of EM energy from outside the vessel to the inside, possibly presenting a hazard for sensitive electronic systems. Characterizing this coupling and the associated susceptibility to external EM interference is important for assessing system robustness.

A traditional method for measuring EM shielding of a weapon system is to perform a direct shielding effectiveness (SE) measurement [4], as depicted in Figure 1-2. One port of a multi-port vector network analyzer (VNA) provides a transmit microwave signal that is amplified to moderate or high power and delivered to a transmit antenna that illuminates a weapon cavity being tested. Several EM probes are placed on the test article that reach into the cavity and can sample internal field levels. An additional probe is typically placed outside the vessel to sample $\overline{E}_{\text{inc}}$. The output of these probes is fed to the available VNA input ports, allowing the relative level of receive signals to be computed.

For the purpose of this report, the shielding effectiveness can be defined as

$$\text{SE} = 20\log_{10}\frac{\|\overline{E}_{\text{probe}}\|}{\|\overline{E}_{\text{inc}}\|}, \tag{1.1}$$

where $\|\overline{E}_{\text{probe}}\|$ is the magnitude of electric field intensity sampled at a probe location inside the vessel and $\|\overline{E}_{\text{inc}}\|$ is the electric field intensity of the planar wave incident on the weapon system.

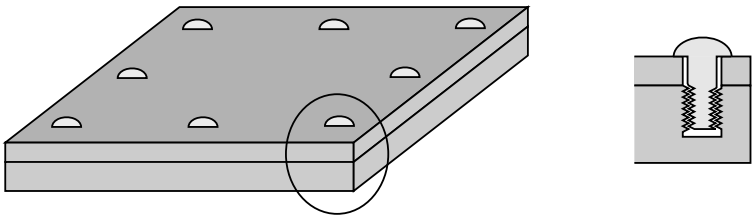

(a) Flange Joint

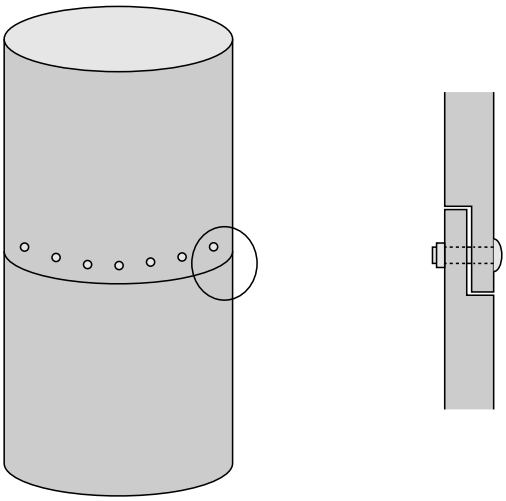

(b) Lap Joint

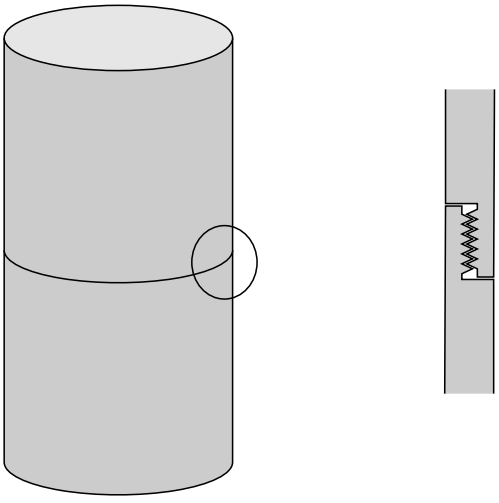

(c) Threaded Joint

Figure 1-1. Common types of enclosure joints. The shielding can also be enhanced using EMR gaskets, which are not shown here.

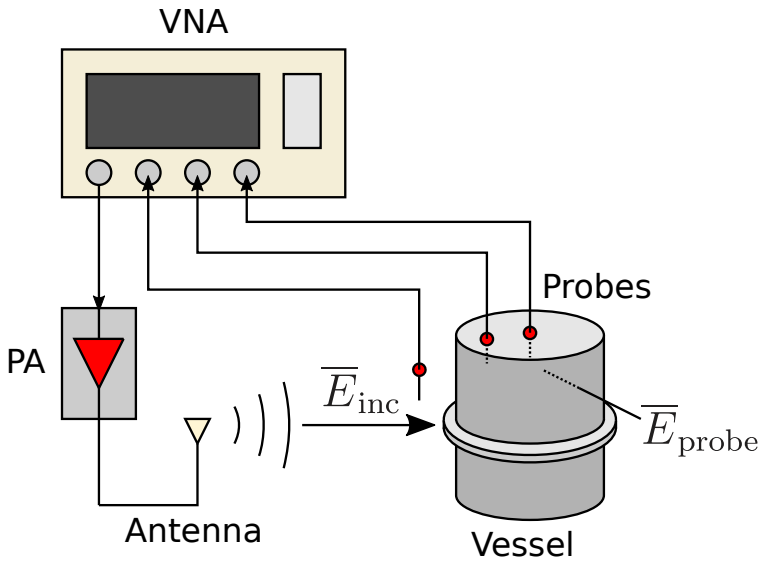

Figure 1-2. SE measurement employing a multiport VNA.

According to this definition, a higher SE value indicates higher penetration of EM energy into the weapon system, which indicates poorer shielding performance.

Although measurement provides a direct characterization of the shielding of a given weapon system, it has several drawbacks. First, such measurements can be expensive and time consuming, allowing relatively few systems to be characterized this way. Second, due to limited time and physical constraints, only a few directions of incident illumination and probe locations can be tested, which creates uncertainty about the actual worst-case SE. Third, the measurement based characterization is often not appropriate in the design stage of a weapon system, due to the need to rapidly test many competing design alternatives. Finally, a measurement often provides little insight as to the nature of coupling into the system and what measures could be taken to improve the shielding.

Numerical simulation of weapon cavities using computational electromagnetic (CEM) tools can be performed to predict SE from a computer-assisted design (CAD) model of the system. Although such simulations can be time consuming, algorithmic acceleration and advances in parallel computing may allow quite complicated models to be analyzed in moderate time on large computing clusters. Simulation overcomes the previously stated disadvantages of measurement. In a simulation, an arbitrarily large number of incident directions and field probe locations can be specified, ensuring that worst-case performance is characterized. Many competing designs can be analyzed in parallel, allowing performance to be compared without needing to build prototypes. Also, since fields that couple into the weapon cavity can be directly observed in a simulation, significant insight can be obtained about the coupling mechanisms and how to improve shielding.

Although simulation has many advantages, the main weak point of simulation is the accuracy of the underlying weapon system models. Several aspects of the models cannot be deduced from a CAD drawing, such as the location and size of gaps that will be present at joint seams, the exact

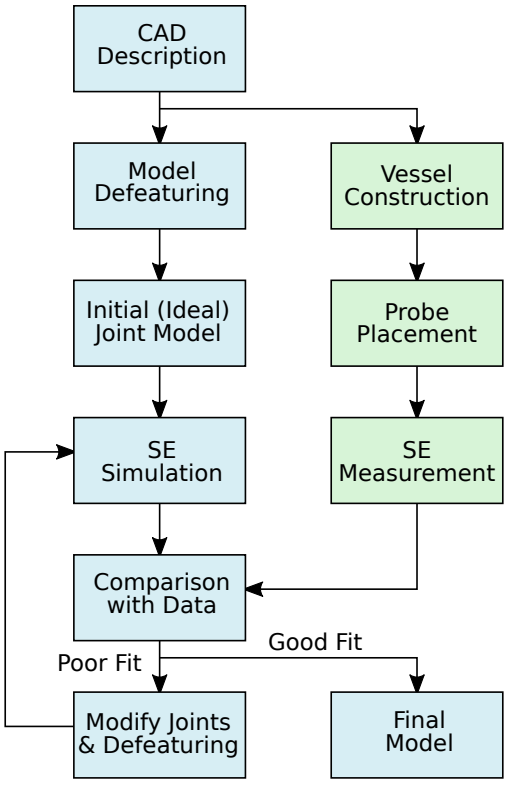

Figure 1-3. Typical workflow for modeling and simulating shielding effectiveness of weapon cavities with joints.

locations of electrical contact, and the electrical properties (such as contact resistance) of the contact points. For this reason, state-of-the-art simulation of weapon cavities still relies to a large degree on measurements to provide ground truth that can calibrate simulation results.

Figure 1-3 shows a typical workflow for the development of an accurate model of a weapon cavity with seams. Beginning with a CAD description of the vessel, the EM analyst removes small features unlikely to affect the EM response, referred to as "defeaturing." Joint parameters, such as slot widths, contact points, and contact resistances, are set to ideal values, such as a constant slot gap width, contact at bolt locations only, and zero contact resistance. Next, the model is simulated using commercial or in-house CEM tools to predict SE. In parallel, the vessel is constructed, probes are placed on the vessel, and direct SE measurements are performed. A comparison of modeled and measured SE will typically show discrepancies, such as resonant SE peaks not matching in terms of center frequency and/or amplitude. Modifications can then be made to the joint parameters or defeaturing to try to improve the fit. For example, the contact resistance at bolt locations or the gap width between bolts can be incrementally increased until a good fit is seen between simulation and measurement. Although this procedure sounds straightforward, it can be very difficult if there are complicated joints with many parameters to be optimized. Further, even if a model is developed that is able to provide a good fit to a limited set of measurements, the model may still fail to predict performance for excitation frequencies or probe locations that were not considered in the measurement.

The purpose of this LDRD project is to overcome the limitations of the current modeling workflow for weapon system cavities, where ad-hoc fitting of simulation and measurement is required. Specifically, this project explores methods of probing vessel joints directly, allowing points of contact to be identified and the electrical properties of contacts (such as resistance) to be estimated. Such methods would allow models of cavities with joints to provide good accuracy on the first iteration, obviating the need for parameter tuning that can be error-prone or even not possible when there are too many parameters. Additionally, if many types of vessels and joints are probed using the developed methods, databases or libraries of slot parameters could likely be compiled, reducing the required number of vessel measurements dramatically.

The report begins in Chapter 2 by simulating slots with one-dimensional (1D) transmission line models and three-dimensional (3D) full-wave simulations, where the goal is to understand how fields in and around the slot are connected to the contact resistance at a joint. The results of these simulations suggest methods for probing and estimating contact resistance at controlled contact points, which is studied in subsequent chapters. Chapter 3 explores a straightforward approach for probing slots, where coaxial probes are placed directly in a flanged joint. Given the undesired sensitivity of this method to mechanical probe placement, an alternative approach is developed in Chapter 4, where near fields are scanned outside, but in close proximity, of the slot. The near-field scanning method is then used to measure joint properties of two different types of vessels. Chapter 5 presents near-field measurements of a vessel having a bolted flange joint, referred to as Vessel 2. Next, Chapter 6 briefly considers near-field probing of a more practical lap-joint vessel. Given the importance of characterizing slots and vessels under mechanical vibration, Chapter 7 develops a method for probing the time evolution of coupling into vessel POEs. Finally, Chapter 8 summarizes the work of this LDRD project and considers the future outlook of this effort.

2. VESSEL SIMULATIONS

2.1. Introduction

This chapter uses simulations to explore the possibility of extracting the resistance of hidden joints using field measurements in or near vessel ports of entry (POEs). We will focus on the resistance of contact points in Vessel 2 slots, using similations to determine how sensitive embedded and/or near-field probes need to be to provide useful estimates of this resistance. Section 2.2 applies a one-dimensional (1D) transmission line model to show the dependence of embedded field probe signals on slot edge resistance. Section 2.3 presents three-dimensional (3D) CST Microwave Studio simulations of Vessel 2, showing the dependence of slot near fields on shim resistance.

2.2. Embedded Probe Simulations

The most direct approach to probing slots to determine contact resistance is to place probes directly in the slot, which is explored experimentally in Chapter 3. Here we use the 1D transmission line model for the slot to consider the required sensitivity of embedded probes. Details of the 1D numerical model are provided in Section D.1 in Appendix D.

Here we analyze Vessel 2, where we model the slot radius as 6.5 inches, which is the radial distance to the center of the slot. The width and depth of the slot are assumed to be 0.005 inches and 1 inch, respectively. The complex shape of the shims complicates defining the length of the slot. The inner and outer angular length of the shims is 7.5° and 19.32°, respectively. We will assume an angular length that is the average of these, or 13.4°, which translates into 6.7° degrees of shim on each side of the slot relative to the bolt center. As shown in the drawing of Vessel 2 in Appendix A, probes can be placed in the slot at locations -22.5°, 0°, and $+22.5^\circ$ relative to the slot center, and bolts are at angles -45° and $+45^\circ$.

Figure 2-1 shows the slot voltage as a function of angle around the slot for four different DC shim resistances. Note that the DC shim resistance has been converted to a (radio-frequency) RF shim resistance of the slot edge using (D.20), and the RF resistance value is the one used in the 1D model. At the shim edge, there is significant variation in the voltage with changing shim resistance, suggesting the ability to extract contact resistance based on slot voltage measurements. Figure 2-2 shows the variation of the probe voltage with shim resistance for the probe closest to the shim at -22.5°. This result indicates that an order of magnitude change in the DC shim resistance corresponds to a change in the probe signal on the order of 0.2 dB to 0.6 dB. This suggests that for the chosen probe locations, very stable embedded probe measurements will be required, which will be expored expermientally in Chapter 3.

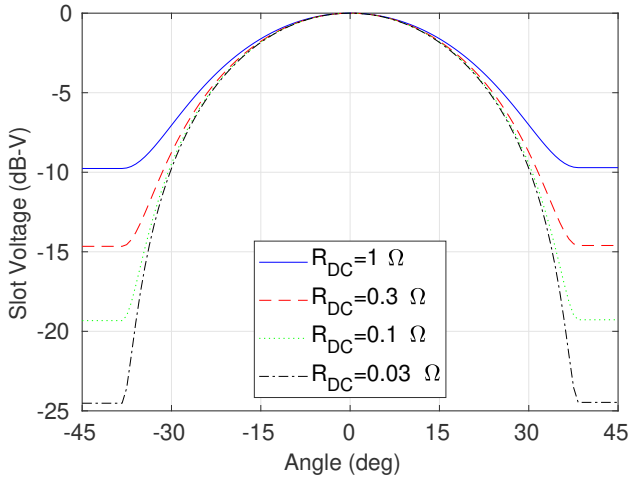

Figure 2-1. 1D slot simulation of a single slot of Vessel 2 for various equivalent DC shim resistances. Note that the slot voltage at the edge of the slot has been extended to the bolt location for easier visualization.

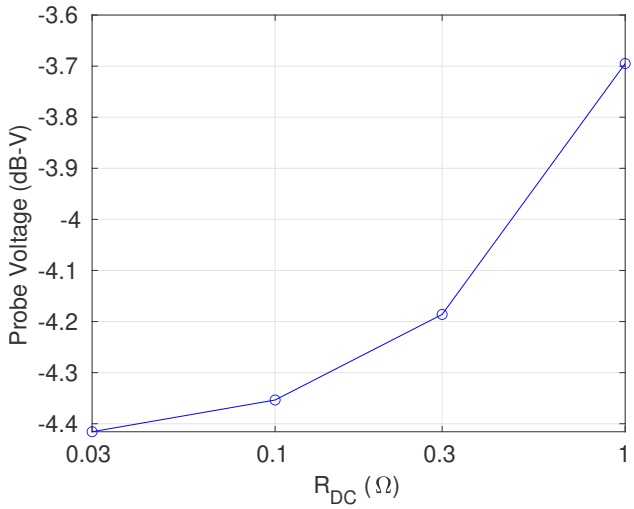

Figure 2-2. Variation of the probe voltage at the probe position at $-22.5°$ with respect to the equivalent DC shim resistance.

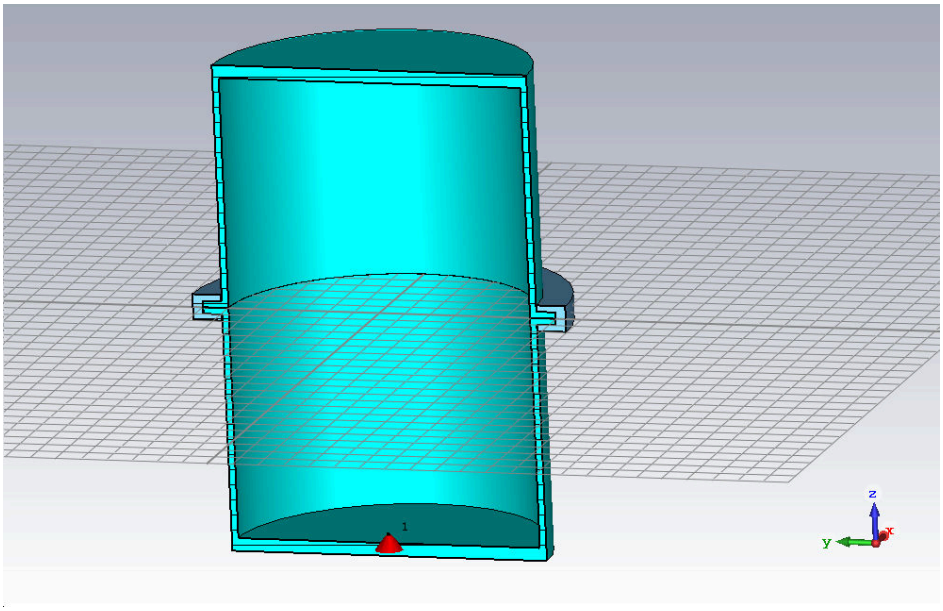

Figure 2-3. Cutaway of the 3D model used for CST Simulation of Vessel 2.

2.3. Near-Field Scanning Simulations

An indirect way to estimate slot fields that are connected to contact resistance is to probe fields that are near the slot. This section explores this possibility through full-wave 3D CST simulation of Vessel 2.

To reduce the number of simulations that need to be performed, the simulation is performed in "transmit mode," where a 1 cm monopole probe at the bottom of the cylinder is excited, producing near fields around the slots and radiated far-fields. As shown in Appendix E, shielding effectiveness (SE) for the excited probe location can be computed for arbitrary angle of incidence using the resulting radiated far-fields by applying reciprocity considerations. This can be more efficient than running many "receive mode" simulations for each plane wave angle of incidence.

The CST model for Vessel 2 that was developed is shown in Figure 2-3. For details on dimensions of Vessel 2, see Appendix A. Although a default mesh size of 10 cells per wavelength was used in most of the model, it was found that obtaining field predictions with high fidelity in and around the slot required explicit control of the mesh size in and near the slot region. Specifically, an air buffer around the flange was added, which has radial and vertical extents of 0.4 and 0.25-inches, respectively. Likewise, an explicit air region was defined as a cylinder occupying the 5-mil slot gap. The flange buffer and slot region were set to have a maximum mesh cell size of 50 mil.

Slot shims were modeled as resistive bulk material, having a conductivity of

$$\sigma = \frac{w}{A\,R_{\mathrm{DC}}}, \tag{2.1}$$

where $w = 5$ mil $= 1.27 \times 10^{-4}$ m is the width of the gap, $A = 1.0197 \times 10^{-3}$ m^2 is the area of the shim, and R_{DC} is the assumed DC resistance of a single shim. Local mesh properties of the shim

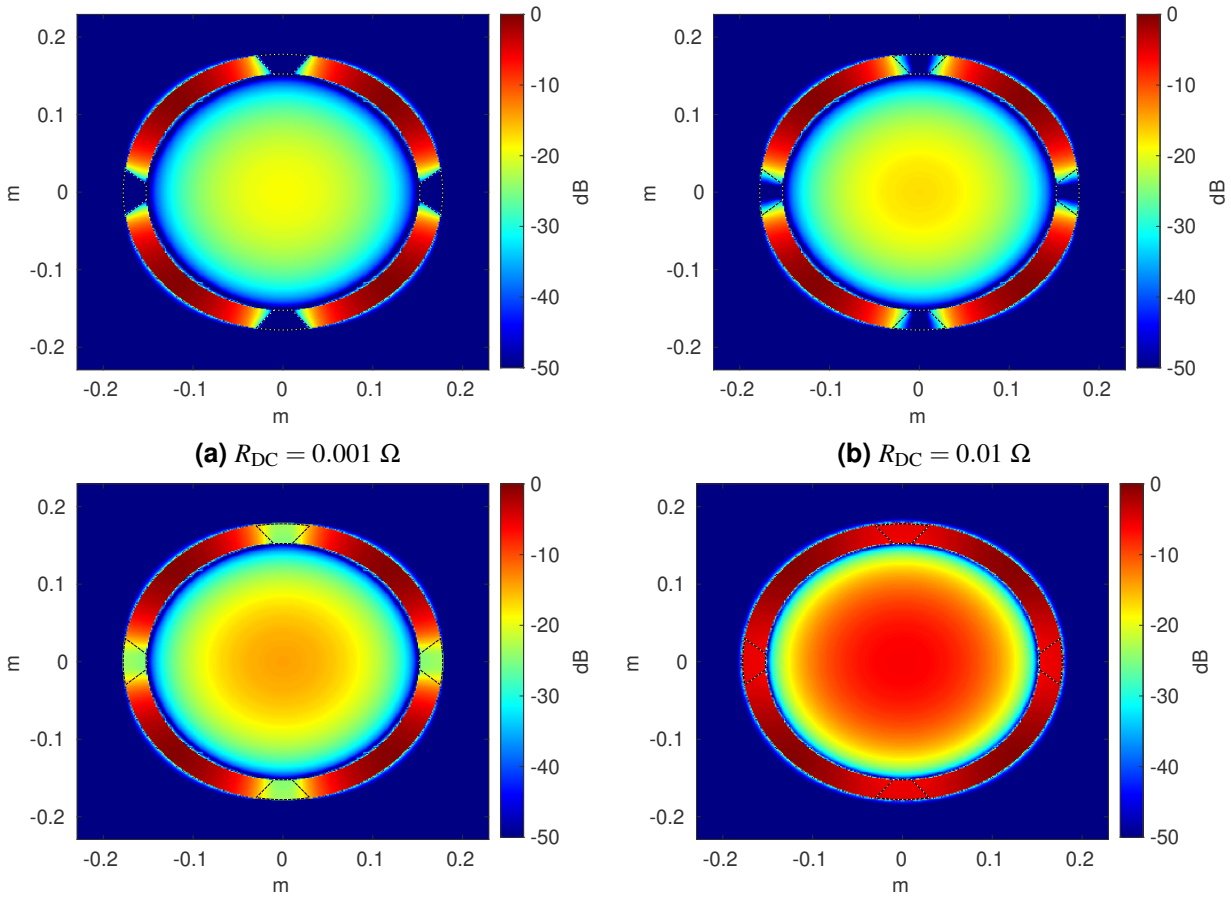

(a) $R_{\mathrm{DC}} = 0.001\ \Omega$ **(b)** $R_{\mathrm{DC}} = 0.01\ \Omega$

(c) $R_{\mathrm{DC}} = 0.1\ \Omega$ **(d)** $R_{\mathrm{DC}} = 1\ \Omega$

Figure 2-4. Vessel 2 near-field E_z in the plane $z = 0$ that cuts through the center of the slot. Shim areas have been highlighted with dotted lines.

regions were set to have a maximum cell size of 50-mil. Perfectly matched layers were used on all sides of the domain to absorb outward radiating waves. To improve efficiency, symmetry planes were used in x and y to reduce the size of the domain by a factor of four. Single-frequency simulations were performed about a center frequency of 753.35 MHz, from 748.35 MHz to 758.35 MHz in 2.5 MHz steps (5 simulation points). Nine DC resistances were used for the shims in the set $R_{\mathrm{DC}} \in \{0.0001, 0.0003, 0.001, ..., 0.3, 1\}\ \Omega$.

Figure 2-4 shows near fields in a plane cutting through the center of the slot at 753.35 MHz (the TM_{010} resonance). As R_{DC} increases from 0.001 to 1 Ω, conductivity of the shim material is decreasing from 125 S/m down to 0.125 S/m, where the lower conductivity allows more penetration of fields into the shim.

It is interesting to consider the angular distribution of fields in the slots as depicted in Figure 2-4. The shape of the shims was chosen to realize slots that have parallel side walls, in order to ensure that the slot length is effectively constant with depth. However, it is apparent that the slot fields tend to prefer a nearly constant angular distribution irrespective of radial dimension. Therefore, a shim shape that conforms more closely to the slot fields would be one with a constant angular

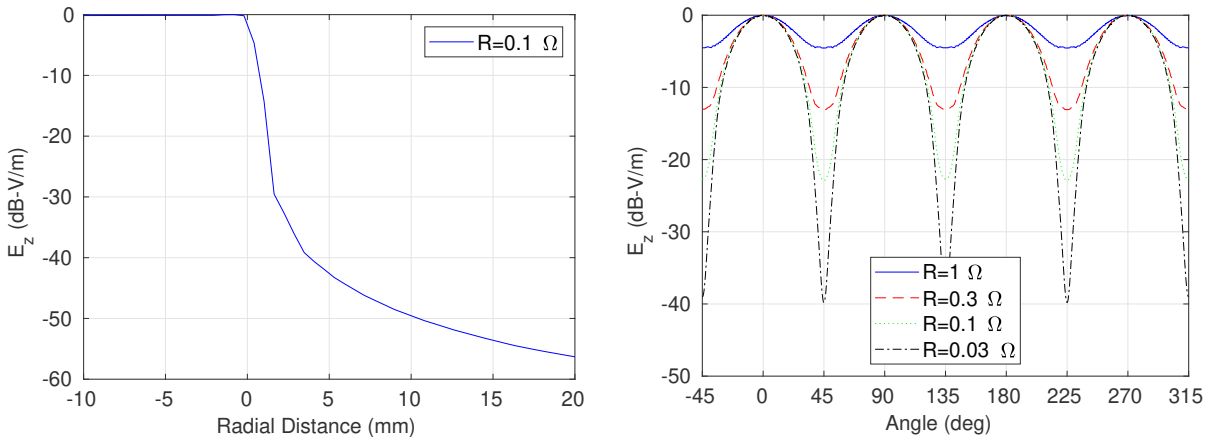

(a) Radial cut ($\phi = 45°$) **(b) Circumferential cut (5 mm from flange)**

Figure 2-5. Vessel 2 near-field E_z in and near the slot: (a) fields as a function of radial distance relative to the outside flange edge, where the cut was taken at the slot center, (b) fields as a function of angle at a distance of 5 mm from the flange.

extent on both the inside and outside of the flange.

Figure 2-5 shows cuts of the near-field E_z near the flange on the outside of the slot, where each plot has been normalized to a maximum of 0 dB. Figure 2-5(a) illustrates how slot fields drop off very rapidly with distance for the narrow 5-mil slot width. Although having a probe as close as possible to the slot would seem advantageous for SNR, it is likely that a probe this close will cause unwanted loading of the slot fields and experience error due to high positioning sensitivity. At a distance of 5 mm, we note that the decay in the slot near fields becomes more gradual and therefore less sensitive to positioning error.

Figure 2-5(b) plots slot near fields as a function of angle at a radial distance of 5 mm, where the curve for each resistance value has been normalized to a maxmimum value of 0 dB. The angles have been shifted such that $-45°$, $45°$, …, $315°$ are bolt/shim positions, and $0°$, $90°$, …, $270°$ are slot centers, which was done to be compatible with angles used in later measurements. The curves show that a maximum field value is seen at the center of the slots in each case, and that the slot edge resistance controls how deep of a null is seen at the bolt locations. This plot illustrates the method for estimating contat resistance developed in this report, which can be summarized as follows:

Slot near fields are measured and normalized as shown in the Figure 2-5(b). A steeper drop in the near field near a contact indicates a lower contact resistance. To obtain an estimate of the slot edge contact resistance, the normalized measured near fields are simply compared with the simulated behavior in Figure 2-5(b), declaring the closest fit to give the estimated resistance.

2.4. Conclusion

This chapter has explored the connection of joint contact resistance to slot near fields for Vessel 2. The results show that by sampling fields in or near the slot, estimates of the slot edge contact resistance can be obtained. The 1D slot simulation for embedded probes suggests that very stable probe measurements will be required, on the order of tenths of a dB, to provide useful contact resistance estimates. CST 3D simulations of near fields at a probe distance of 5 mm show that a single near-field probe could theoretically provide the information required to estimate contact resistance. Given the ability to place a near-field probe at arbitrary points around the slot, this approach may be more practical than the embedded probe arrangement.

3. EMBEDDED PROBES

3.1. Introduction

This chapter describes experiments with an embedded probe concept, where a coaxial probe is placed directly inside a port of entry (POE) in a vessel. The potential advantage of this method is the ability to observe internal slot fields directly. However, this approach suffers from high sensitivity of the probe response with respect to probe positioning, as will be shown in the remainder of this chapter.

3.2. Probe Construction

Figure 3-1(a) depicts the coaxial probe that was fabricated for this work. The probe is constructed from 0.141-inch semi-rigid coaxial cable, where a female SMA connector is attached on one side. The other side of the semi-rigid cable (the probe end) is press fitted into a brass collar. The diameter of the brass collar is chosen to be slightly larger than vessel probe holes to provide a tight fit. Also, careful machining of the probe end of the brass collar and open semi-rigid cable ensures a flat surface.

Vessels to be probed are drilled with 0.250-inch diameter holes in flanges that surround the POEs of interest, as described in Appendix A. The probe assembly is press fitted into the POE probe holes using pushing hardware that was specially designed for this purpose, as depicted in Figure 3-1(b). The probe pusher is a screw clamp with a flat end or stop, providing leverage to press the probe into the hole and stopping when the probe reaches the flat end that is flush with the vessel flange. By swapping out one of the plates shown in Figure 3-1(b), the pusher hardware can also push a probe out of a probe hole to allow easy removal.

Ideally the end of a probe is perfectly flush with the vessel flange after insertion, and from caliper measurements the positioning error is estimated to be within ± 2 mil. Figure 3-1(c) shows a probe embedded in the flange in Vessel 2 using this procedure.

3.3. Probe Calibration

Since each probe is manufactured using a manual procedure, identically constructed probes are expected to exhibit slightly different response due to manufacturing variations. To check differences in probe response, a few identically fabricated probes were measured in a gigahertz transverse electromagnetic (GTEM) cell (Ametek GTEM 250A SAE). Here each probe is pushed

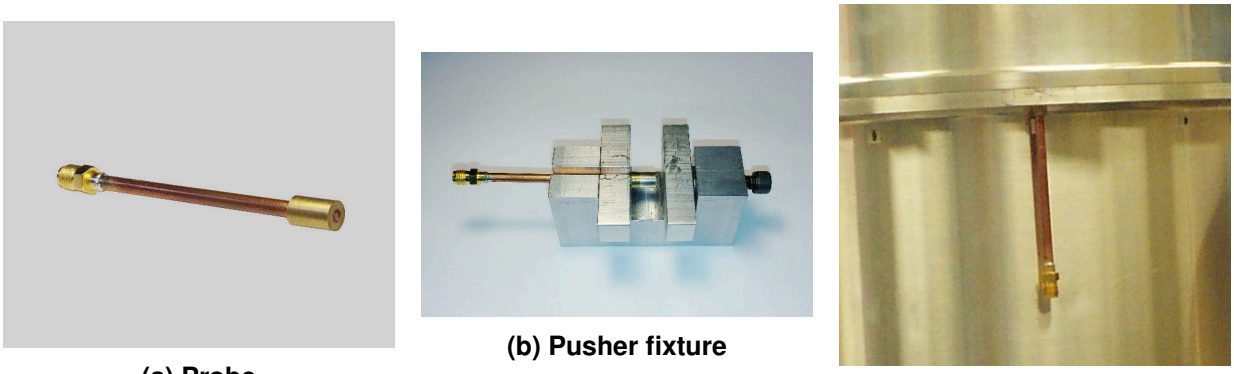

(a) Probe

(b) Pusher fixture

(c) Mounted probe

Figure 3-1. Embedded coaxial probes: (a) closeup of fabricated probe, (b) pushing hardware for press fitting probe into vessel holes, and (c) an example of a probe after being pressed into a vessel hole.

into a sample plate that is inserted into the bottom of the GTEM, where plate edges and adjoining GTEM surfaces are electrically connected using copper tape.

Measurements were performed with an Agilent N5230 VNA using 1601 points from 200 MHz to 2 GHz. The VNA was calibrated using an electronic calibration unit, removing the effect of cables used to connect to the probe and GTEM. Unlike monopoles of appreciable electrical length, coaxial probes have weak response to transverse EM field. Measurement SNR was improved here using a narrow resolution bandwidth of 100 Hz and coherently averaging over 10 sweeps.

Figure 3-2 shows the repeatability of the calibration measurement, where Probe 1 is pressed into the GTEM plate, measured, and then removed for each trial. The response looks nearly identical for the three trials in Figure 3-2(a). The small differences in the trials can be better seen by smoothing the responses with a 100-point rectangular window and removing the mean smoothed response from each probe response. The result of this procedure is depicted in Figure 3-2(b), showing that worst-case repeatability is approximately ± 0.1 dB.

Next, three identically constructed coaxial probes were measured in the GTEM as shown in Figure 3-3 and analyzed in a similar way to the repeated measurements. For the different probes, maximum deviation in the probe response is approximately ± 0.3 dB.

3.4. Vessel Measurements

Section 3.3 suggests that the coaxial probes that have been manufactured have nearly identical responses. Further, the repeatability of measurements when pushing probes into a plate and measuring in the GTEM is good. However, there is a concern that probes pushed into a flange next to a narrow slot may exhibit higher sensitivity to placement error. To put this in perspective, controlled slot widths of 5 mil were used in this work, yet the error in the probe placement is approximately ± 2 mil.

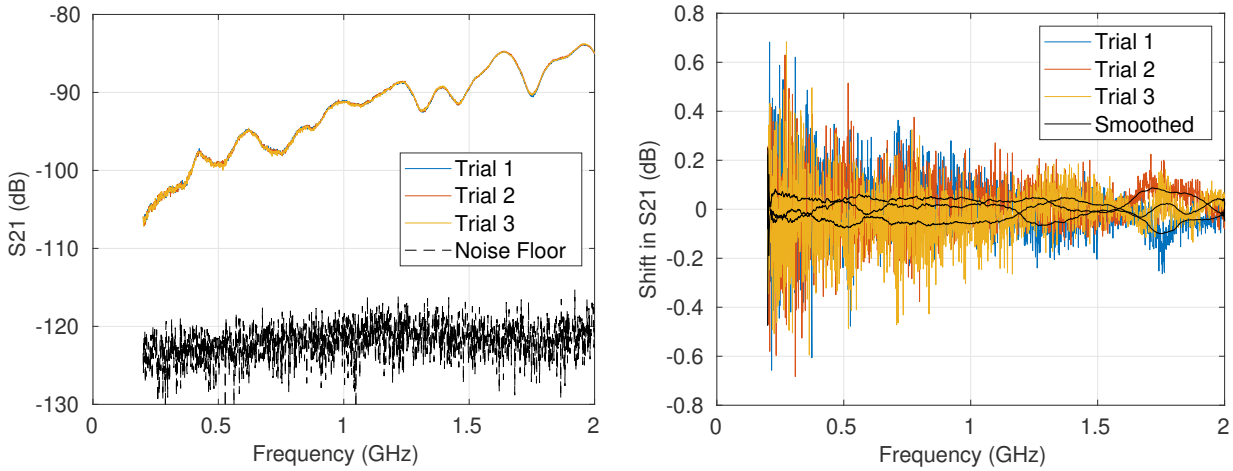

(a) Raw **(b) Normalized**

Figure 3-2. Repeated GTEM measurements of a single coaxial probe, where the probe is removed and pressed again into a plate between measurements: (a) raw measurement, and (b) normalized probe responses where the mean smoothed response has been removed from each measured response.

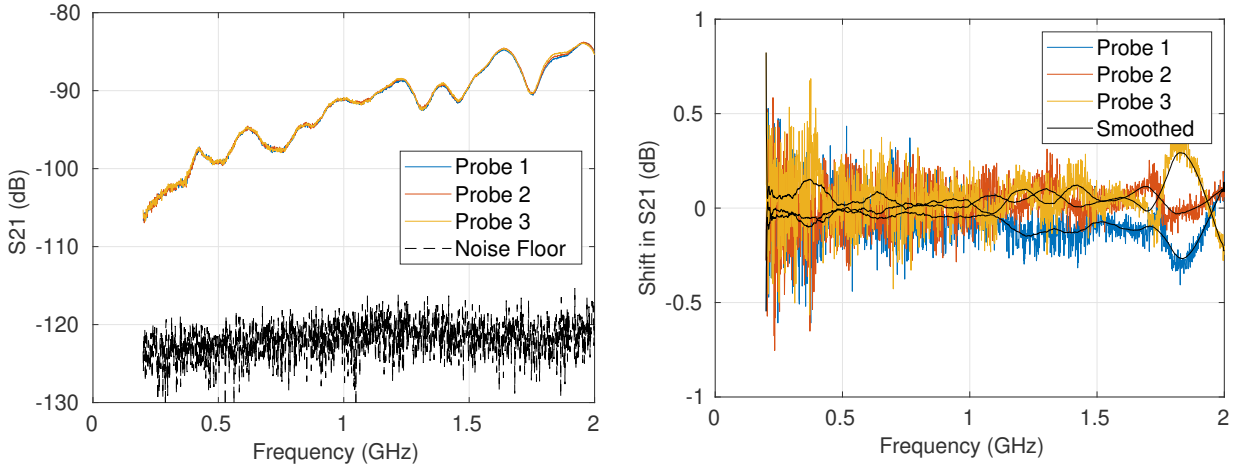

(a) Raw **(b) Normalized**

Figure 3-3. GTEM measurements of three identically constructed coaxial probes: (a) raw measurement, and (b) normalized probe responses where the mean smoothed response has been removed from each probe response.

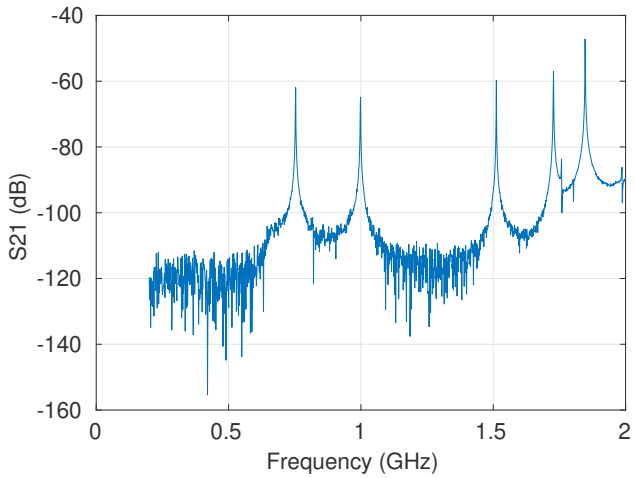

Figure 3-4. Typical S_{21} measurement using an embedded probe. Peaks correspond to natural EM resonances of the cylindrical cavity.

	TM_{010}	TM_{012}	TM_{014}	TM_{020}	TM_{022}
Measured Freq. (GHz)	0.7535	0.9988	1.5118	1.7278	1.8470
Ideal Freq. (GHz)	0.7527	0.9981	1.5117	1.7277	1.8479

Table 3-1. Resonant frequencies of Vessel 2 measured with an embedded probe, compared with ideal values computed using a closed-form expression.

Initial vessel measurements with embedded probes were performed using Vessel 2 as described in Appendix A. A 1-cm monopole probe was placed in the top probe hole along the axis of the vessel. The coaxial probe under test was pressed into the hole of the flange that is at the center of a slot (equi-distant between bolts). For this test, 5-mil shims were used to create a controlled slot gap width. Bolts in this measurement were torqued to 50 in-lbs.

The VNA was set to measure 1601 points from 200 MHz to 2 GHz with a resolution bandwidth of 100 Hz, with Port 1 connected to the 1-cm probe that excites the vessel, and Port 2 connected to the coaxial probe that samples fields in the flange slot. The VNA was calibrated to the ends of the SMA cables used in the measurement. Figure 3-4 shows a typical measurement of S_{21} for these measurements, where peaks correspond to natural EM resonances of the cylindrical cavity. Table 3-1 lists the identified resonances from the measurement, along with theoretical values given by the closed-form expression given in Appendix B. Some slight discrepancies can be seen in the resonant frequencies, but this is partly due to the frequency resolution of 1.1 MHz used in the measurement.

Measurement variation with respect to several system parameters was checked by performing the following actions to the system and performing a VNA sweep before and after each action:

1. No action (control case).
2. Disconnecting and reconnecting SMA connections to the probes.
3. Moving the SMA cables and the cart with the vessel by a small amount.

	TM_{010}	TM_{012}	TM_{014}	TM_{020}	TM_{022}
1. No Change	0.0043	0.013	0.007	0.0095	0.0063
2. SMA Connections	0.14	0.16	0.16	0.17	0.16
3. Moving Cables	0.015	0.018	0.0091	0.0053	0.026
4. Replacing Lid	2.4	0.2	0.21	0.23	1.3
5. Replacing Probe/Lid	3.8	3.4	3.4	3.4	3.5

Table 3-2. Variation of repeated measurements in dB, performing the stated actions on the system between VNA sweeps.

4. Unbolting, removing, replacing, and bolting the top vessel half.
5. Unbolting and removing the top vessel half, pushing out the flange probe, pushing it back in, and replacing and rebolting the top vessel half.

For each case above, the action was performed three times, providing four measurement trials. Variation is quantified as the standard deviation of $|S_{21}|$ in dB at the identified resonant peaks given in Table 3-1, or

$$\text{Variation}_m = \text{std}_n \left\{ 20\log_{10} |S_{21}^{(n)}(f_m)| \right\} \tag{3.1}$$

where n is the nth trial, $\text{std}_n(\cdot)$ is the standard deviation function with respect to index n, f_m is the mth resonant frequency, and $S_{21}^{(n)}(f)$ is the nth trial of the VNA transmission measurement at frequency f.

Table 3-2 gives the variation seen in the repeated measurements while performing the described actions between them. The experiment shows that most actions have a small effect on the measurement. Even removing the lid and bolting it down again had a small impact for some resonances. Clearly the repeatability of measurements is degraded the most by removing the flange probe and pushing it back into place, where variation is worse than 3 dB. It would be interesting to be able to decouple this effect from that of removing the vessel lid, but currently the lid must be removed to remove and reinsert the flange probes.

3.5. Simulation of Probe Sensitivity

To see if 3 dB variation due to probe insertion uncertainty is reasonable, simulations of an idealized slot setup were performed in CST as depicted in Figure 3-5. The simulated geometry consists of two metal plates of dimension 10×10 cm^2 separated by a gap of 5 mil. A coaxial probe penetrates into the bottom plate, and the top of the probe is ideally flush with the top surface of the bottom plate (zero vertical offset). The simulated coaxial probe closely models the fabricated probes. The simulated probe has an inner conductor diameter of 0.91 mm, a dielectric outer diameter of 1.5 mm, and a dielectric constant of 2.1.

The vertical offset of the probe relative to the ideal location is varied from -2.5 mil (recessed into the bottom plate) to +2.5 mil (extending above the bottom plate). A wave port is used to launch a TEM wave on one side of the structure toward the probe. Boundary conditions on the source side and opposite side are set to be absorbing boundaries. Boundaries on the remaining lateral sides

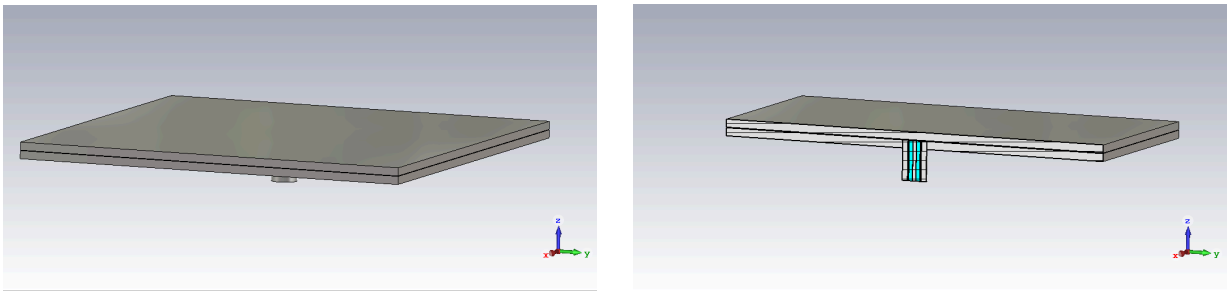

(a) Parallel plate geometry **(b) Cutaway showing coaxial probe**

Figure 3-5. CST simulation setup for a coaxial probe pushed into a parallel plate waveguide with plates spaced 5 mils apart.

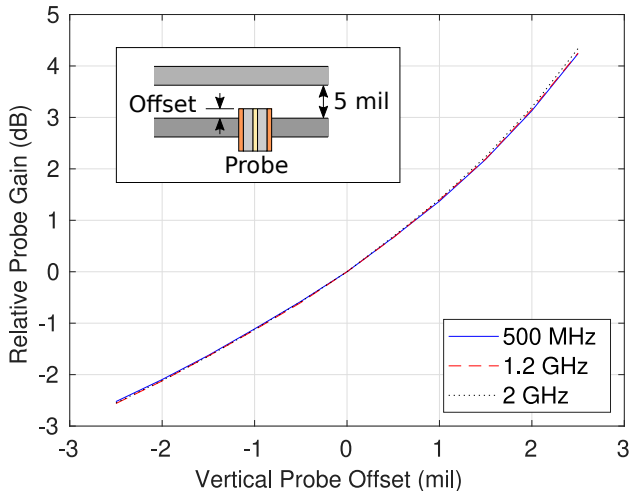

Figure 3-6. Changes of probe gain with respect to probe vertical offset from the CST simulations depicted in Figure 3-5.

are set to be perfect magnetic conductor (PMC). CST simulations provide S_{21} between the wave port and the probe over a frequency range of 500 MHz to 2.0 GHz, which is normalized to 0 dB for the zero offset case, referred to as relative probe gain.

Figure 3-6 shows the simulated probe gain, indicating that the change of gain with respect to vertical probe offset is largely independent of frequency for this frequency range. The slope of the curves is approximately 1.33 dB/mil of offset, indicating that a 3 dB change in the response only requires about 2 mil of shift in the vertical offset. This result is in line with the expected accuracy of the pusher hardware and observed variations with repeated probe placement.

3.6. Conclusion

This chapter has described calibration and measurement variability experiments that were performed with embedded coaxial field probes that are placed directly in vessel POEs. As simulations of Vessel 2 showed in Section 2.2, embedded probes must be sensitive to field changes on the order of tenths of a dB to allow useful measurement of joint contact resistance. The results

of this chapter suggest that errors in excess of 3 dB can occur due to random variation associated with probe insertion. Therefore, the current situation is that embedded probes are not suitable for measuring spatial variation of slot fields that allow joint contact resistance to be estimated.

Shortcomings of the embedded probe concept could be remedied in at least two ways:

- More advanced pusher hardware could be developed that allows probes to be placed more accurately, say within 0.1 mil, thus providing sufficiently small error due to placement uncertainty.
- Advanced metrology could be used to measure the vertical offset of the probes, allowing differences in probe response to be predicted and calibrated out of measurements.

Given the advantages of the near-field scanning concept explored in Chapter 4, the embedded probe concept will not be studied further in this report.

4. NEAR-FIELD SCANNING

This chapter explores a near-field scanning method that was used to overcome the challenges of the embedded field probe concept introduced in Chapter 3. Section 4.1 introduces near-field scanning of points of entry (POEs), highlighting relative advantages with respect to embedded probes. Section 4.2 presents the near-field setup and components used in this work. The specific near-field probes that were used are described in Section 4.3. This information provides the foundation for contact resistance measurements performed in Chapters 5 and 6.

4.1. Introduction

As was demonstrated in Chapter 3, directly embedding field probes into POEs is problematic due to high sensitivity of probe response with respect to mechanical placement. This chapter explores an indirect method of probing slot fields by placing a field probe in close proximity of the POE on the outside of the vessel. By moving the vessel in a controlled way, near fields all along the POE can be scanned using a single probe. Advantages of the near-field probing method include the following:

- Since a single field probe is used, there is no need to calibrate relative probe responses.
- The method is practically non-invasive as long as the field probe is not too close to the POE being probed.
- Vessels to be probed do not require modification, which is in contrast to embedded probes, where probe holes needed to be drilled along the POEs.
- High spatial resolution of fields can be obtained, which is only limited by the precision of the vessel positioning hardware and the inherent resolution of the probe.

4.2. Measurement System

Near-field and SE measurements in this report were performed using the setup depicted in Figure 4-1, where the goal is to probe both vessel near fields and far-field SE around natural cavity resonances.

The chamber size was $4\times4\times6$ ft^3, which is large enough to support near-field scanning in a closed configuration, but too small to allow far-field antenna separation for SE measurements. To allow both near-field scanning and SE measurements to be performed in succession, the chamber was used in a semi-anechoic configuration, where one wall of the chamber was left open as depicted in Figure 4-1. The chamber is placed on two tables with a space in between, allowing

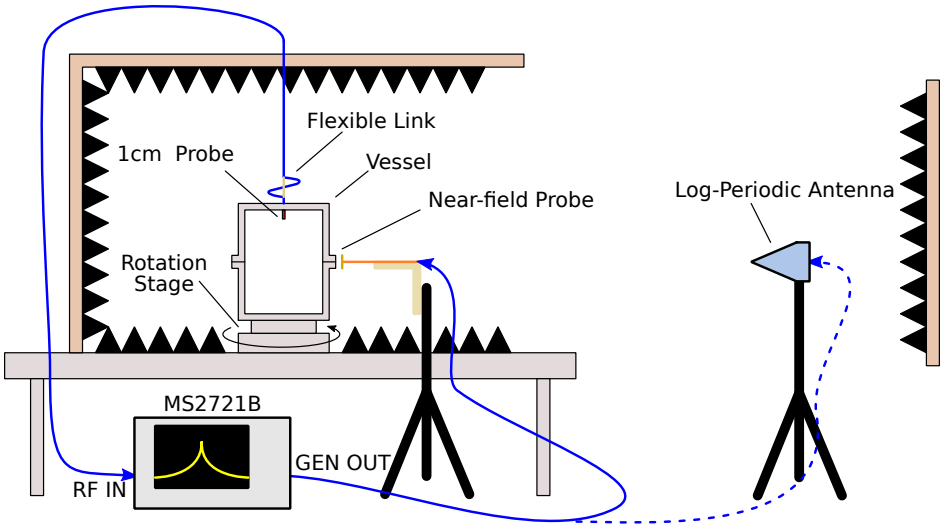

Figure 4-1. Diagram of the semi-anechoic measurement setup. The MS2721B spectrum analyzer has a tracking generator whose output (GEN OUT) is alternatively connected to the near-field probe or the far-field log-periodic antenna. The spectrum analyzer input (RF IN) connects to the 1 cm internal vessel field probe. Note that the near-field probe and tripod are moved away when performing far-field measurements with the log-periodic antenna.

cables and tripods to reach up through a center slot between the tables. Additional absorber was placed in the lab on surfaces where reflections are expected, such as on the back wall behind the far-field log-periodic antenna.

All near-field and SE measurements were performed with an Anritsu MS2721B spectrum analyzer having an integrated tracking generator with 0 dBm output power. The spectrum analyzer input (RF IN) was always connected to the 1 cm field probe inside the vessel. The generator output (GEN OUT) was connected alternatively to a near-field probe or the far-field log-periodic antenna (Aaronia Hyperlog 7040, covering 700 MHz to 4 GHz). The near-field probe and log-periodic antenna were placed on individual tripods to facilitate repeated positioning between measurements. In this work, we concentrate on natural resonances of the vessel under test. In order to sufficiently resolve such resonances, a maximum frequency span of 10 MHz was used around each resonant peak with 551 measurement points.

In the near-field probing case, the tracking generator was connected to the near-field probe, which was placed 5 mm from the POE. A wood holder is used as depicted in Figure 4-2 to avoid placing extra metal near the vessel. The rotational symmetry of the vessels used in this work allowed POE fields to be probed along the entire circumference of the flange using a computer-controlled rotation stage. Rotation of the vessel was performed in a stepped fashion, where for each rotation angle, the vessel was stopped and the required spectrum analyzer sweeps were performed before rotating to the next angle. As a tradeoff between measurement time and spatial resolution, an angular step of 2° was used in this work. Automatic control of data acquisition and vessel rotation was accomplished using MATLAB.

It is worth discussing the choice of the transmit and receive probe for the near-field measurement. Intuitively, it seems that exciting the internal 1 cm antenna with the source would provide a more

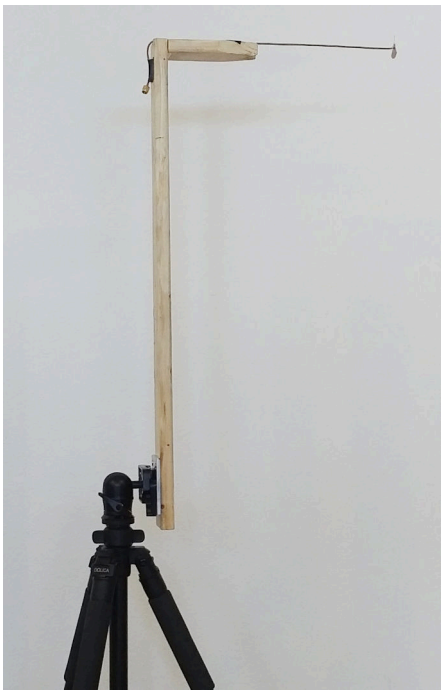

Figure 4-2. Wood holder used for near-field probe placement.

sensitive measurement, because strong resonant fields inside the vessel would be generated. However, it was realized (and verified through measurement) that the reciprocal arrangement shown in Figure 4-1 measures the same transmission coefficient, but with higher immunity to external RF interference. This arrangement was therefore used for the results presented in this report.

For SE measurements, the tracking generator output was disconnected from the near-field probe, and the near-field probe and tripod were moved away from the measurement area. The generator output was then connected to the log-periodic antenna, spaced 2.5 m away from the vessel POE. The same stepping procedure was then used to allow SE to be measured for incident angles all around the vessel circumference. Note that the near-field probe and log-periodic antenna were placed so that near-field probing angles and far-field incident angles coincide.

Measurements were calibrated using a through measurement, where the transmit path is connected directly to the receive path through a known 50-dB of attenuation. The measured signal strength was then used to remove cable and connector losses of the system. Noise, self-interference (cable cross coupling), and external interference were checked by connecting the transmit cable end to a 50-ohm terminator and measuring the usual received signal on the internal 1 cm probe. The resulting signal level due to noise and/or interference sets the effective noise floor of the measurement. In all measurements presented in this report, this measured noise level was -120 dBm or lower, allowing the SNR of subsequent measurements to be bounded.

Initial experiments used a rotary SMA joint between the tracking generator output and the 1 cm probe to allow continuous rotation of the vessel. However, even though the isolation of the rotary joint was approximately 70 dB or better, it was found that this was insufficient for the very low

Figure 4-3. Flexible cable link connection used to allow vessel rotation while maintaining high isolation.

signal levels measured in this work. Therefore, instead of a usual rotary joint, the simple flexible link arrangement was used as depicted in Figure 4-3. The flexible link was created using a 12-inch length 0.086-inch diameter SMA cable (Molex 0897621542), which coils up as the vessel rotates. A thick rubber band placed between the vessel connection and the top of the flexible cable allows the cable to be held in place as it winds or unwinds, avoiding the cable becoming caught during a scan. The flexible link allows 360° of non-continuous rotation with excellent isolation.

4.3. Probe Designs

This section introduces and characterizes the near-field scanning probes used in this report.

4.3.1. Monopole Probe (1 cm)

The internal probe used in vessel measurements was the 1-cm monopole probe depicted in Figure 4-4. The probe consists of a bulkhead SMA connector with a machined 1-cm brass pin that fits into the center conductor of the connector. The bulkhead connector is cut to allow the pin base and outer coax ground to be flush with the inner vessel surface. Without this cut, the SMA connector would have an extra sheath around the monopole base, slightly changing its effective length. For gain measurements of the 1 cm monopole, two 9-inch aluminum plates with a thickness of 0.075-inch and tapped center holes were fabricated, as depicted in Figure 4-4.

Gain of the 1-cm probe was measured using the semi-anechoic chamber configuration described in Section 4.2, where identical 1 cm probes with 9-inch ground planes were connected to the two ports of the spectrum analyzer. The two probes were spaced by 2.32 m, with one probe inside the chamber and another outside. The measurement was calibrated by performing an initial through measurement using a known 50-dB of attenuation. The resulting antenna gain for a single 1 cm

(a) 1-cm probe in a ground plate

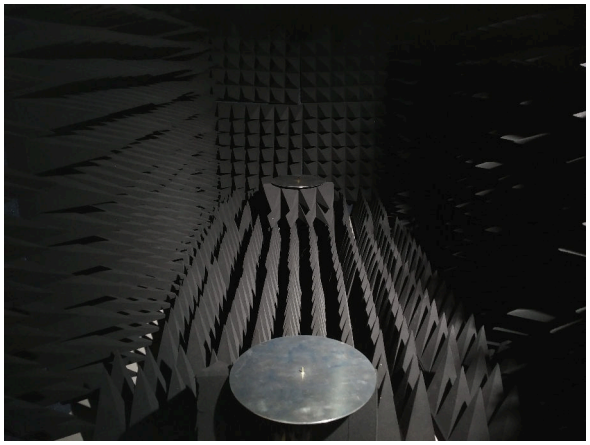

(b) Anechoic gain measurement

Figure 4-4. The 1-cm monopole probe used as the internal vessel field probe, as a reference antenna for antenna gain measurements, and as an external near-field probe in initial experiments. The figure shows the probe mounted in 9-inch aluminum plates that were used for characterizing the gain of the 1-cm probe.

probe is shown in Figure 4-5. The measurement is corrupted by noise (mainly at low frequency) and likely by multipath in the semi-anechoic configuration. To partially remove these effects, the gain was smoothed by fitting it to a quadradic polynomial. Figure 4-5 also shows CST simulations that were performed of the same monopole probe in a 9-inch ground plane. Approximately 1.5 dB of error is seen between measurement and simulation. Given the uncertainties of the measurement, the CST simulations of the 1-cm probe will be used to characterize its gain hereafter.

Some initial near-field scanning experiments were performed with the 1 cm probe without a ground plane as depicted in Figure 4-6. One expected disadvantage of the simple monopole is the unbalanced nature of the probe, which could cause surface currents in the cable sheath to corrupt the measurement. This concern is amplified by the fact that the probe lead cable would typically align with the vessel axis, which is the orientation of the dominant component of electric field produced by slots that run along the circumference of a vessel. Another practical disadvantage is that the SMA connector at the base of the probe is fairly large, limiting how close the probe can be to the POE. For these reasons, the monopole probe was only used for initial testing.

4.3.2. Skirt Probe

The “skirt” probe that was developed is depicted in Figure 4-7. The basic design is a monopole with a skirt below that acts as a small ground plane. The reason for using a flat skirt rather than a conical one is to allow the probe to be placed very close to the POE as desired.

The probe is constructed from 0.086-inch semi-rigid coaxial cable, where the outer sheath and dielectric have been removed to provide a short 1-cm monopole on one end. The skirt is a filled 90° arc having a radius of 0.75-inch, which has been constructed from Rogers 4003C circuit

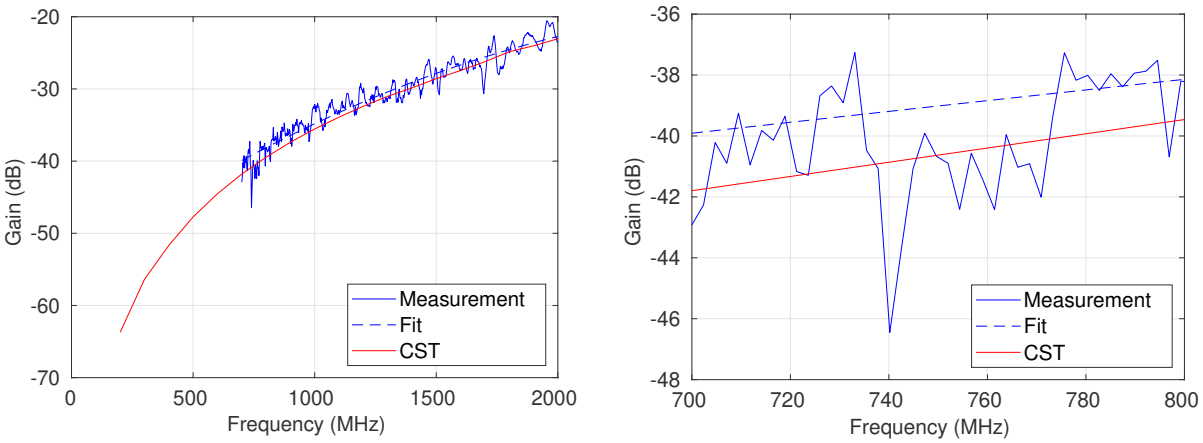

(a) Measured and simulated 1-cm probe gain

(b) Detailed response around 750 MHz

Figure 4-5. Measured gain of the 1-cm monopole probe in a 9-inch diameter circular ground plane, compared with CST simulations. The smoothed measured response was generated by fitting the measurment to a quadratic polynomial.

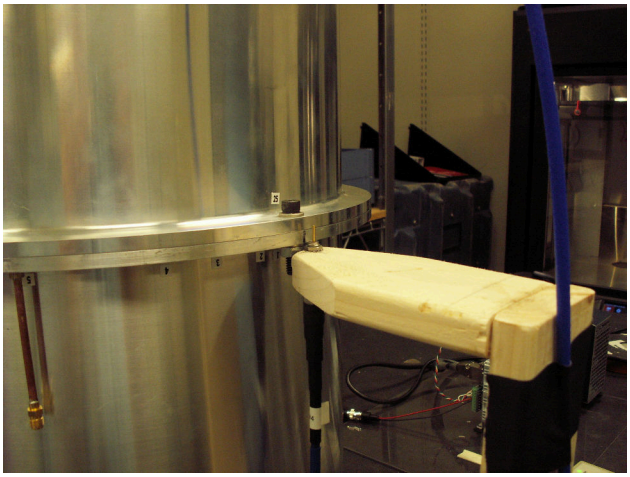

Figure 4-6. The 1-cm probe used without a ground plane to create a simple near-field probe for initial experiments.

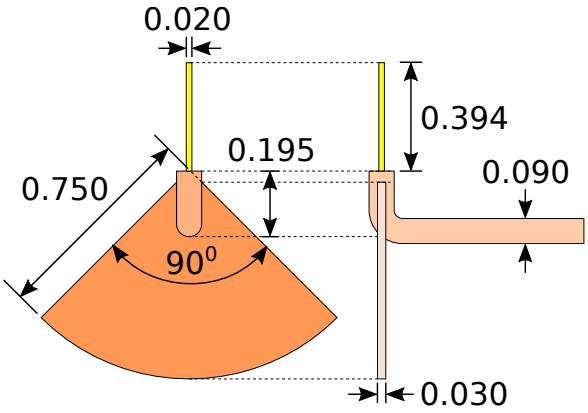

(a) Skirt probe dimensions

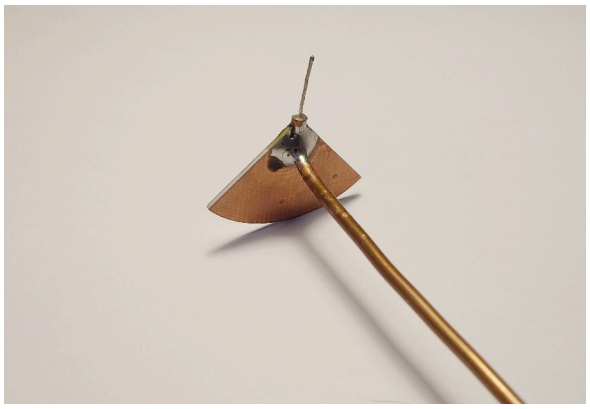

(b) Fabricated probe

Figure 4-7. "Skirt" probe, consisting of a 1-cm monopole and a flattened ground skirt. In (a), units are inches, and the skirt is fabricated from Rogers 4003C substrate material.

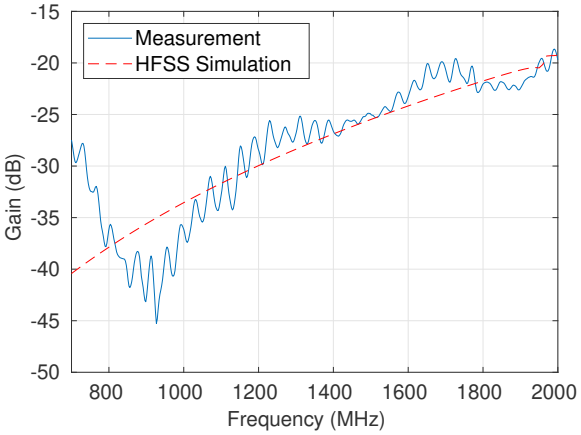

(a) Skirt probe gain

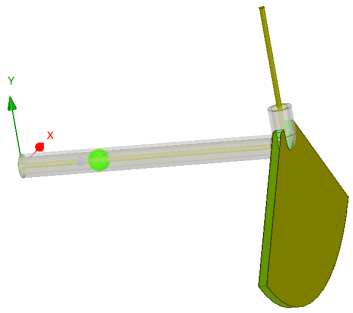

(b) HFSS model

Figure 4-8. Gain characterization of the skirt probe from semi-anechoic measurement and HFSS simulation.

board material having a thickness of 0.030-inch. The skirt has a small notch at its apex, allowing the cable to pass through and to be soldered on.

A long lead line with a 90° bend at the end allows the probing end to be placed relatively far from tripods and mounting hardware that could adversely affect the near-fields being measured. In practice, the probe is oriented such that the lead line is oriented radially with respect to a cylindrical vessel. POEs of interest, such as a flanged joint, will produce fields that are nearly orthogonal to the lead line, minimizing coupling into the sheath of the lead.

The gain of the skirt probe was measured in the semi-anechoic configuration using the HyperLog 7040 antenna as the reference and a separation distance of 1.4 m. Figure 4-8 shows measured gain compared with "realized gain" simulated in HFSS. The measurement and simulation show good agreement above 1 GHz, whereas below 1 GHz up to 10 dB of difference is seen. It is not clear whether the deviation reflects actual response of the fabricated probe, or rather a limitation of the

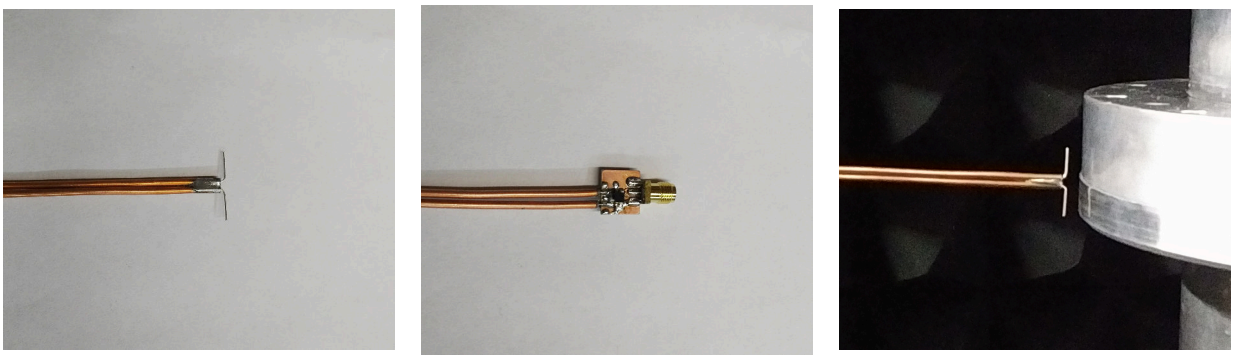

(a) Probe end (b) Lead side with balun exposed (c) Vessel probing

Figure 4-9. Dipole probe that was developed in this work as an alternative to the skirt probe.

semi-anechoic setup. Fortunately, knowing the gain of the near-field probes is not necessary in this work, since probe gain is normalized out when estimating contact resistance. The important consideration is whether the probe provides adequate gain (and SNR) for frequencies of interest. This report focuses mainly on cavity resonances near 750 MHz, where we will consider the gain of the skirt probe to be no worse than -39 dB (the simulated value).

4.3.3. Differential Dipole Probe

One concern of the skirt probe in Section 4.3.2 is that the relatively large skirt will limit its spatial resolution when used in field scans. As a possible alternative, a true differential dipole probe design is depicted in Figure 4-9. Here two sections of 0.086-inch semi-rigid cable are run in parallel (and soldered together), thus providing a differential feed line. The sheath and dielectric at the probe end of the differential line are stripped, and the center conductors are bent at 90° angles relative to each other, forming a 2-cm dipole antenna, which is electrically short for the frequencies probed in this report.

Two options exist for the lead side of the differential lead. The first method is to solder two separate connectors onto the differential lead, one on each side of the differential pair. This arrangement requires measurement with a multi-port oscilloscope or VNA, where the two-port differential to single-ended transformation (subtraction) is performed in post processing. A second method, which is the one used in this work, is to place a balun at the end of the lead to convert the differential signals to single ended ones. The advantage of this second approach is that only a single port is required on instrumentation for the port. Also, since a reciprocal balun can be used, the same probe could be used as both a transmitter and receiver as required. The disadvantage is that the balun will have a finite bandwidth and imperfect phase balance, which could corrupt experiments. The type of balun used in this work is the Mini-Circuits TCM2-33X+ transformer. Note that when in use, the small balun circuit board in Figure 4-9(b) is enclosed in copper tape.

The gain of the differential dipole probe was not measured in this work, since this probe was only used to check the spatial resolution of the skirt probe. As shown in Section 5.3.3, virtually

identical results are obtained with the skirt probe and differential dipole probe, indicating that the relatively large ground skirt does not adversely affect the probe's spatial resolution.

4.4. Conclusion

This chapter presented the near-field scanning concept that was used in this work to overcome sensitivity limitations of embedded probes. A straightforward measurement setup using a spectrum analyzer with a tracking generator was presented, allowing slot near fields and far-field shielding effectiveness to be conveniently measured. A few near-field probes were developed that find use in later measurements. The measurement system described here was used for the data collection described in Chapters 5, 6, and 7.

5. VESSEL 2 MEASUREMENTS

5.1. Introduction

In Chapter 2, CST simulations of Vessel 2 revealed the close connection of slot near fields to effective contanct resistance at the shims. This chapter presents measurements of Vessel 2 using the hardware setup described in Chapter 4 to estimate contact resistance using near-field scans. This chapter also considers whether including estimated contact resistance of the joints improves shielding effectiveness (SE) predictions of the simulated vessel. Measurement and modeling of Vessel 2 without controlled slot gaps (without shims) is also considered briefly.

5.2. Measurement with Shims

We first consider the controlled case of Vessel 2 with shims at the bolt positions, which sets the slot gap to be 5 mil. The semi-anechoic setup described in Chapter 4 was used to measure slot near fields using the skirt probe for a probe distance of 5 mm. The setup was also used to measure SE at a distance of 2.5 m using the log-periodic antenna.

5.2.1. Signal and Noise Power

The power level seen from the near-field skirt probe is demonstrated in Figure 5-1. The four measurement bands have been chosen to be approximately centered on the first four identified resonances of Vessel 2. The sample angles of 0° and 45° correspond to the slot center and bolt location, roughly showing maximum and minimum probe power, respectively. The plots also show the result of measuring the receive power seen from the 1 cm vessel probe connected as normal when a terminator is placed on the end of the transmit cable. Thus the "noise" curve includes noise and possibly self and external interference as well. The noise/interference floor is seen to be approximately -120 dBm or better for all of the bands probed. The plots show that even in the case of relatively lower power seen at bolt positions, SNR of the measurement technique is approximately 30 dB or better.

5.2.2. Near-field Scan Repeatability

Repeatability of the near-field measurements is of concern, given the sensitivity of the embedded probes seen in Chapter 3. Two near-field scans of Vessel 2 were performed with the skirt probe, performed approximately one day apart. Bolt torque was 80 in-lbs during each measurement, and

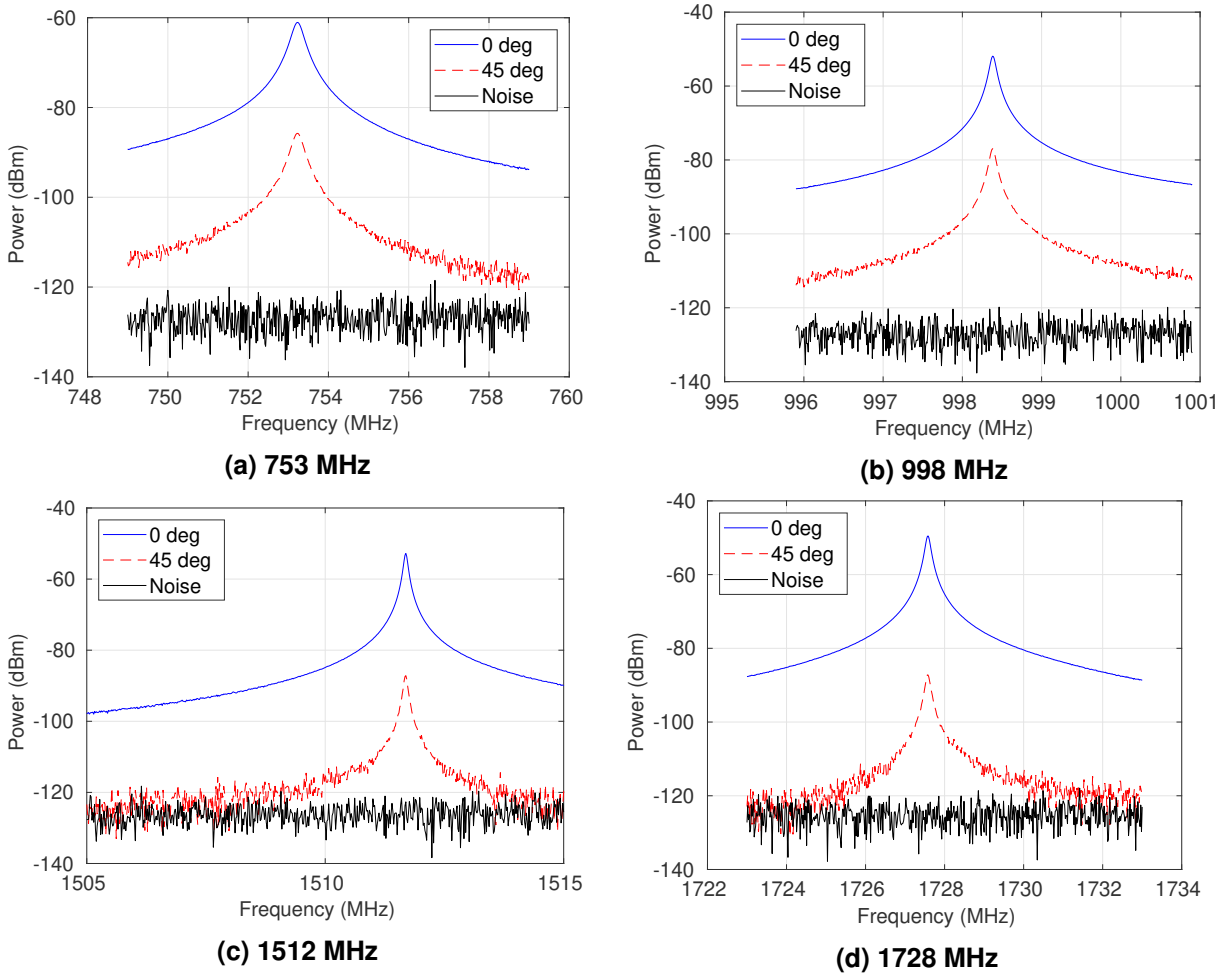

(a) 753 MHz

(b) 998 MHz

(c) 1512 MHz

(d) 1728 MHz

Figure 5-1. Raw power level seen at the slot center (0 deg) and bolt position (45 deg) using the skirt near-field probe at 5 mm spacing.

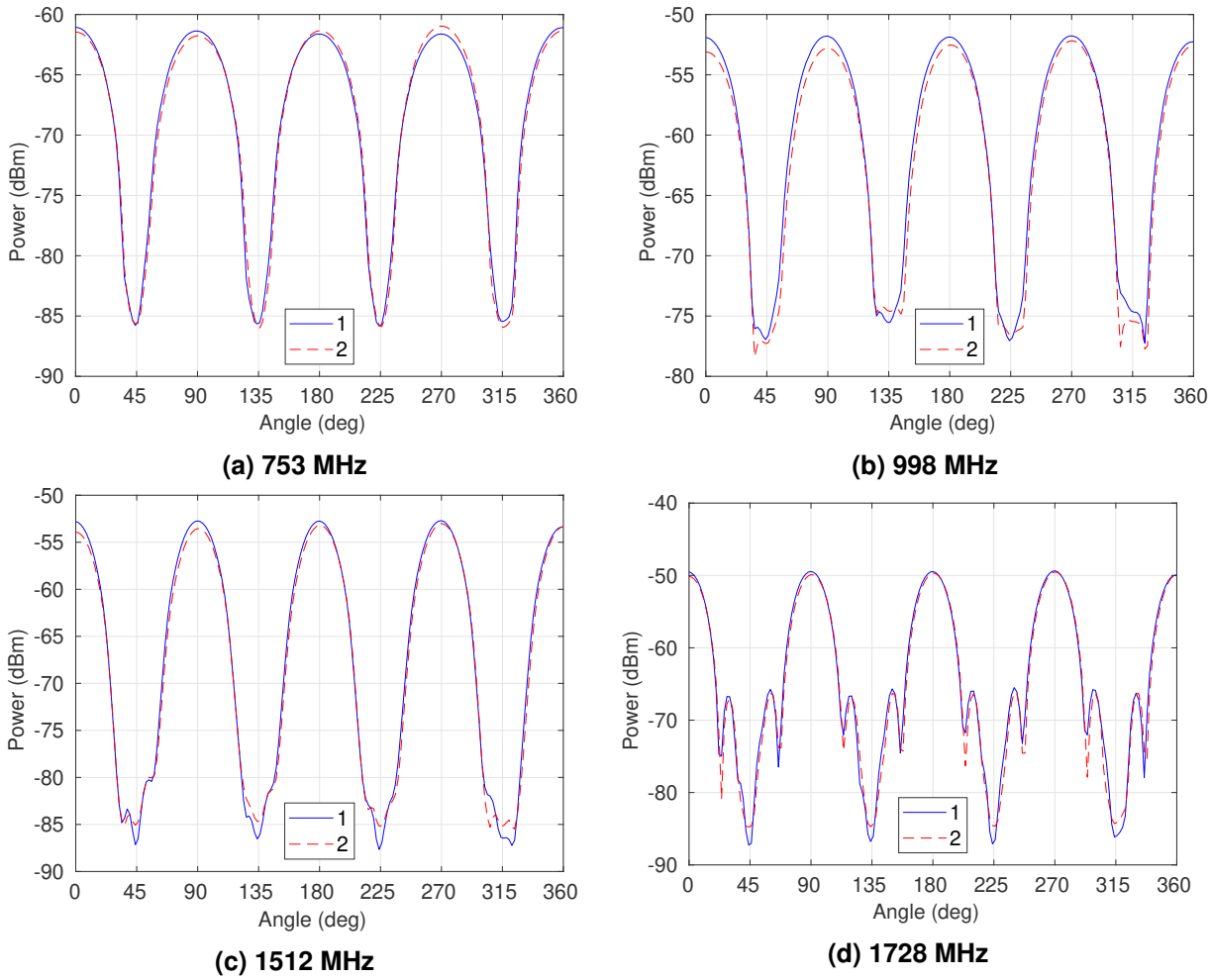

Figure 5-2. Repeatability demonstrated by performing two near-field scans of Vessel 2, where bolts were loosened and retorqued and the near-field sensor was moved between measurement trials.

the bolts were loosened and retightened between the separate measurement trials. Also, the near-field sensor tripod was moved away and then repositioned between trials. Thus, we expect to see some variation in the measurement due to retorquing the bolts and moving the sensor slightly.

Figure 5-2 compares the response for the four bands of interest. Here we select the frequency bin in the measurement band giving the highest amplitude, and plot that versus scan angle. Overall, very little difference is seen in the measured near-field scans for the two trials, except for the near nulls at the bolts, where 2-5 dB of variation can be seen in some bands. Since this variation only occurs right at the bolt, it is not expected to significantly hinder estimation of the contact resistance. Although we do not plot an example here, it has been observed that when the measurement hardware and vessel are not touched or moved by the operator, back-to-back scans provide much better repeatability, usually within 0.5 dB in the worst case.

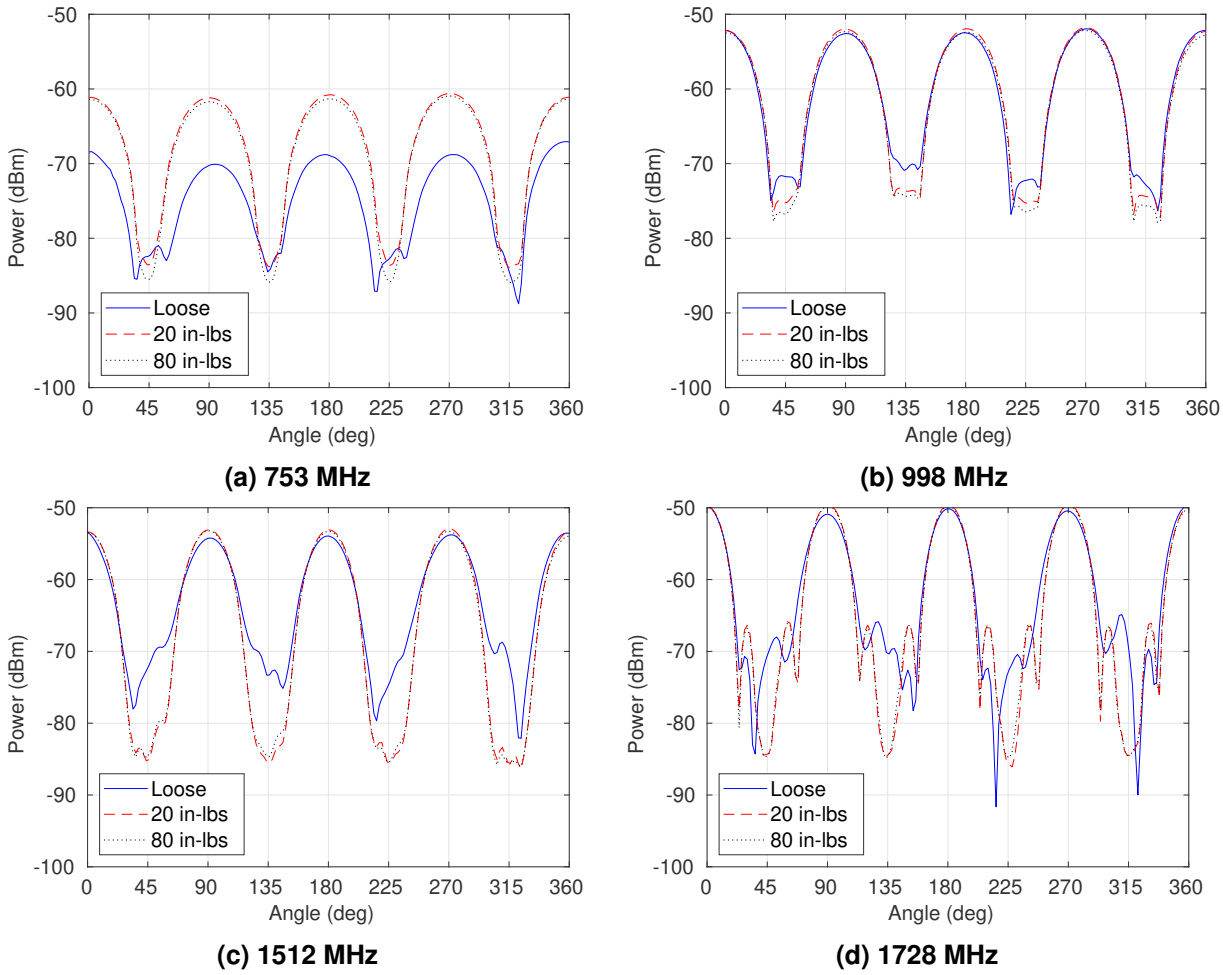

Figure 5-3. Raw near-field scans of Vessel 2 with respect to bolt torque.

5.2.3. Torque Dependence

We next consider the effect of torque on the near-field scanned response. An experiment was performed where near-field scans were measured with three different torques: no torque (loosened bolts), 20 in-lbs, and 80 in-lbs. Figure 5-3 shows raw power level from the near-field scan, where the noise floor is approximately -120 dBm. The results show that only at the lowest resonance do we see a significant shift in the peak power level (as much as 8 dB) when comparing loosened and torqued bolts. For all frequency bands, one can see that the effective contact resistance is higher for the loosened case, evidenced by the smaller amplitude difference of the peak amplitude at the center of the slot and the amplitude at the bolt. We note that for all the bands, the responses for 20 and 80 in-lbs of torque look almost identical, suggesting that the contact resistance changes little after 20 in-lbs.

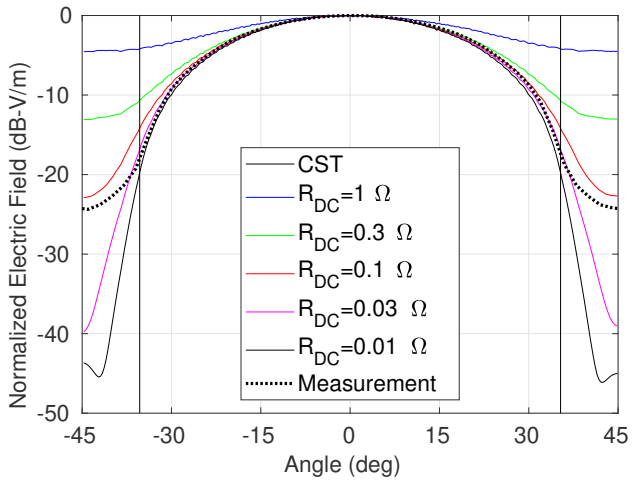

Figure 5-4. Measured Vessel 2 slot near fields compared with CST simulations from Chapter 2. Measured near fields for the four slots have been averaged and normalized to obtain a single response. Note that $-45°$ and $45°$ represent bolt locations. The vertical black lines shows the angular extent of the shims on the outside flange.

5.2.4. Contact Resistance Estimation

In this section, we focus on the lowest resonance at 753 MHz and Vessel 2 with bolts torqued to 80 in-lbs. As was shown in Figure 5-3, at 80 in-lbs of torque, the near-field maxima (at the slot centers) as well as the near-field minima (at bolt locations) are fairly constant for the four slots and four bolts, respectively. Therefore, measured data from the four different slots of Vessel 2 will be averaged to get a single average slot response.

Figure 5-4 compares the measured and CST-simulated near fields sampled 5 mm away from the flange of Vessel 2. For CST simulations, the multiple curves show the field shape for different values of the DC contact resistance at each bolt position. Note that since we are interested in the shapes of the curves, not the absolute levels, each curve has been normalized to a maximum value of 0 dB.

Figure 5-4 suggests that the effective contact resistance lies between 0.03 Ω and 0.1. It is interesting that in the slot region, the measured response conforms closely to the $R_{\mathrm{DC}} = 0.03\ \Omega$ case, while in the shim region, the contact resistance looks effectively higher, closer to the $R_{\mathrm{DC}} = 0.1\ \Omega$ case. This discrepancy reveals that the constant conductivity model for the shim is likely too simple to fully capture the effect a bolted contact. However, given the simplicity of the model, the qualitative agreement of the measurement and model is encouraging.

5.2.5. Shielding Effectiveness (SE) Comparison

In the previous section, a contact resistance value between $R_{\mathrm{DC}} = 0.03\ \Omega$ and $0.1\ \Omega$ was estimated for the shims of Vessel 2 with 80 in-lbs of torque. In this section, we consider whether

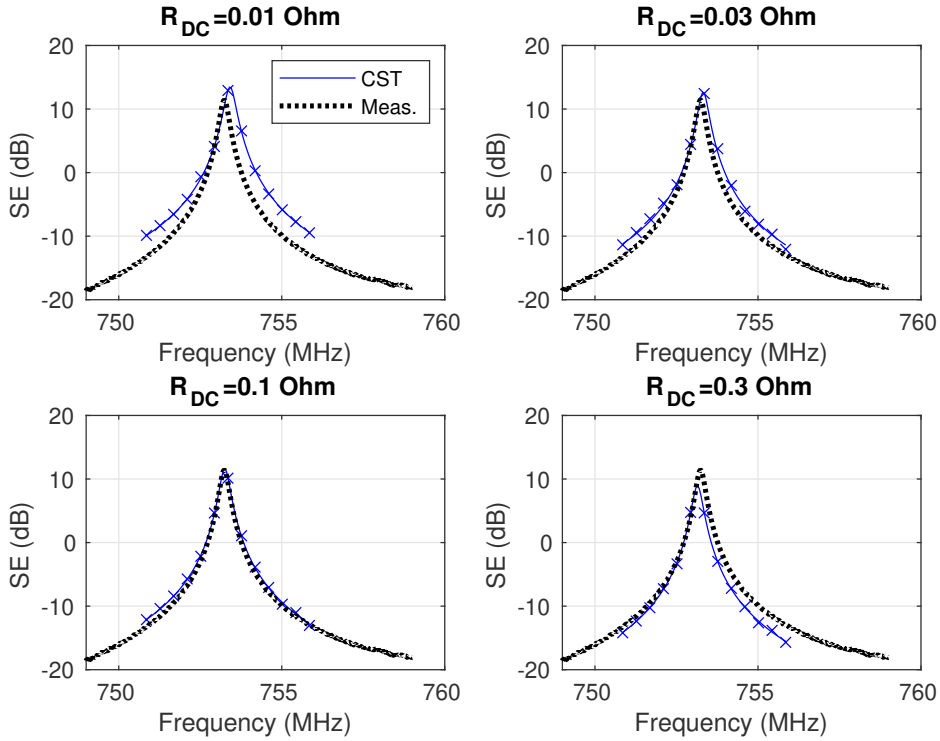

Figure 5-5. Measured Vessel 2 SE compared with CST simulations from Chapter 2 for a plane wave incidence of $-45°$ (aligned with bolt).

including that estimated contact resistance in a simulation of the vessel provides good predictions of measured SE.

SE values can be computed for different shim resistances using radiated far-fields given by "transmit mode" CST simulations in Chapter 2, computed using (E.25) in Appendix E. Note that when checking agreement between transmit and receive mode simulations in CST, it was found that CST apparently uses an available power of $P_{\text{in}} = 0.5\ W$ for the S-parameter port and radiated electric far field computations normalize the measurement distance to $d = 1$ m. CST simulations were performed using 13 discrete frequency points from 750.85 MHz to 755.85 MHz, and interpolated using the parallel RLC resonance fitting method described in Appendix C. The semi-anehcoic measurement setup described in Chapter 4 that was used here also provides measured SE versus incident scan angle, where SE is computed from the raw RF measurement using expression (E.8) from Appendix E.

Figure 5-5 compares measured and simulated SE for plane wave incidence at $-45°$ (aligned with a bolt). The four separate plots show CST simulated SE response for the four closest candidates for shim contact resistance. The result shows that the $R_{\text{DC}} = 0.1\ \Omega$ case appears to provide the closest fit, in terms of SE level and center frequency. Although more difficult to judge, the fit in Q for the $R_{\text{DC}} = 0.1\ \Omega$ also appears to be good.

Figure 5-6 compares measured and simulated SE for plane wave incidence at $0°$ (aligned with the slot center). In this case the $R_{\text{DC}} = 0.1\ \Omega$ case provides a good fit for the resonant frequency and Q, but underestimates the SE level by approximately 1 dB. Note that the measurement

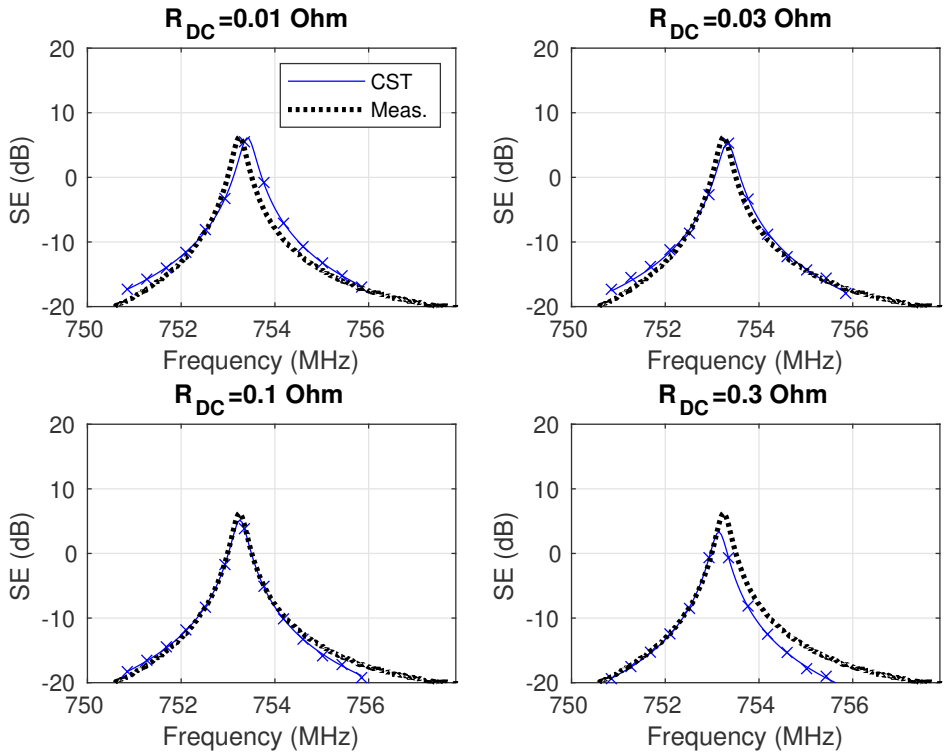

Figure 5-6. Measured Vessel 2 SE compared with CST simulations from Chapter 2 for a plane wave incidence of 0° (aligned with slot center).

uncertainty is likely greater than 1 dB, given the semi-anechoic nature of the measurement setup. Also, a nominal gain of 5 dBi was assumed for the log periodic antenna based on the datasheet, but the actual gain could be slightly different.

Table 5-1 lists parameters of the measured and simulated resonances for -45° and 0° plane wave incidence. For both incident angles, the resistance $R_{\mathrm{DC}} = 0.1\ \Omega$ provides the best fit in terms of resonant center frequency f_0. The quality factor (Q) does not change appreciably over the resistance values considered here. It is surprising that the Q appears to increase slightly with increasing shim resistance in some cases, but the amount of increase is likely not significant given the sensitivity of the RLC fitting method. As explained previously, the SE level is well predicted for -45° by the value of $R_{\mathrm{DC}} = 0.1\ \Omega$. For 0° incidence, this value underpredicts SE by approximately 1 dB.

Figure 5-7 tracks the peak SE value as a function of scan angle for simulation and measurement. The result shows that for bolt directions, the $R_{\mathrm{DC}} = 0.1\ \Omega$ is the most accurate model. However, for incidence centered on the slot centers, the level is underpredicted by this model, and a lower DC resistance actually gives a more accurate prediction of SE level.

-45° Incidence				
	R_{DC}	f_0	SE	Q
Measurement	-	753.24 MHz	11.4 dB	2591
Simulations	0.01Ω	753.41 MHz	13.5 dB	2159
	0.03Ω	753.32 MHz	12.7 dB	2376
	0.1Ω	753.25 MHz	11.6 dB	2399
	0.3Ω	753.14 MHz	9.0 dB	2335
0° Incidence				
	R_{DC}	f_0	SE	Q
Measurement	-	753.24 MHz	6.2 dB	2581
Simulations	0.01Ω	753.42 MHz	6.1 dB	2175
	0.03Ω	753.33 MHz	5.3 dB	2108
	0.1Ω	753.25 MHz	5.2 dB	2321
	0.3Ω	753.14 MHz	3.3 dB	2218

Table 5-1. Numerical comparsion of resonances for measured SE and SE from CST simulations for various shim resistances.

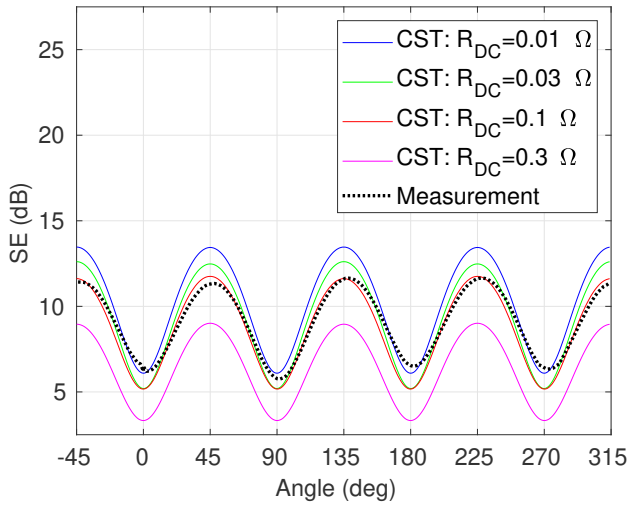

Figure 5-7. Measured peak SE of Vessel 2 compared with CST simulations from Chapter 2 as a function of the plane wave angle of incidence. Note that -45° and 0° correspond to alignment with a bolt and a slot center, respectively.

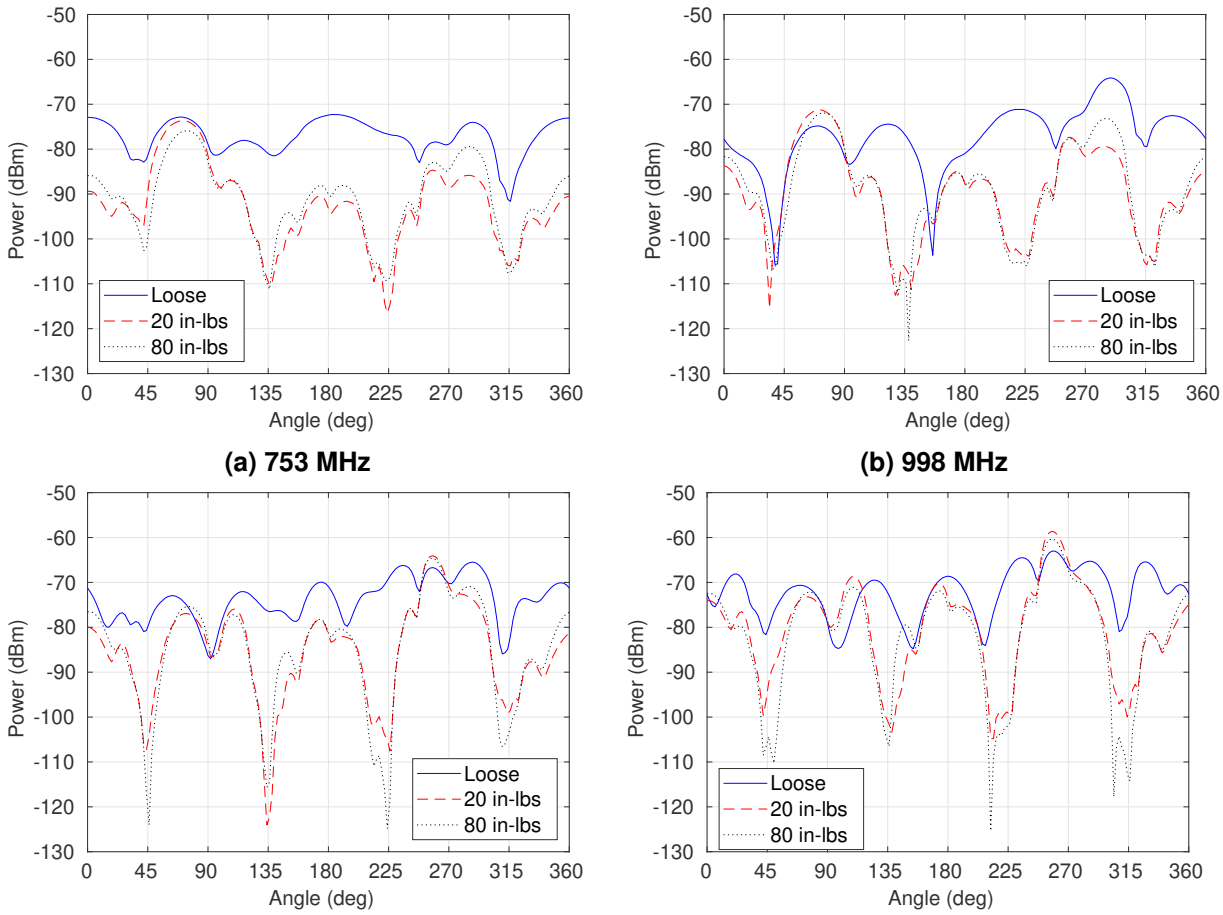

Figure 5-8. Near-field scans of Vessel 2 with respect to bolt torque for bolts without shims. Here, fields were scanned using the skirt probe at 5-mm separation.

5.3. Measurement Without Shims

This section presents near-field scans that were performed of Vessel 2 without shims, leading to a very narrow slot gap and a random contact pattern in the slot regions. The purpose of this section is to explore the structure of fields in uncontrolled slots and to consider whether the slot models presented in Appendix D can capture the observed behaviors.

5.3.1. Torque Dependence

This section shows the dependence of slot fields scanned using the skirt probe with 5-mm separation from the slot. Fields were scanned for three different torques: no torque (loosened bolts), 20 in-lbs, and 80 in-lbs. Raw near-field scanning data is shown in Figure 5-8, and the noise floor was approximately -120 dBm in these measurements. Interestingly, the results are very different from what was seen in Figure 5-3 when shims are present. Recall that in the case of

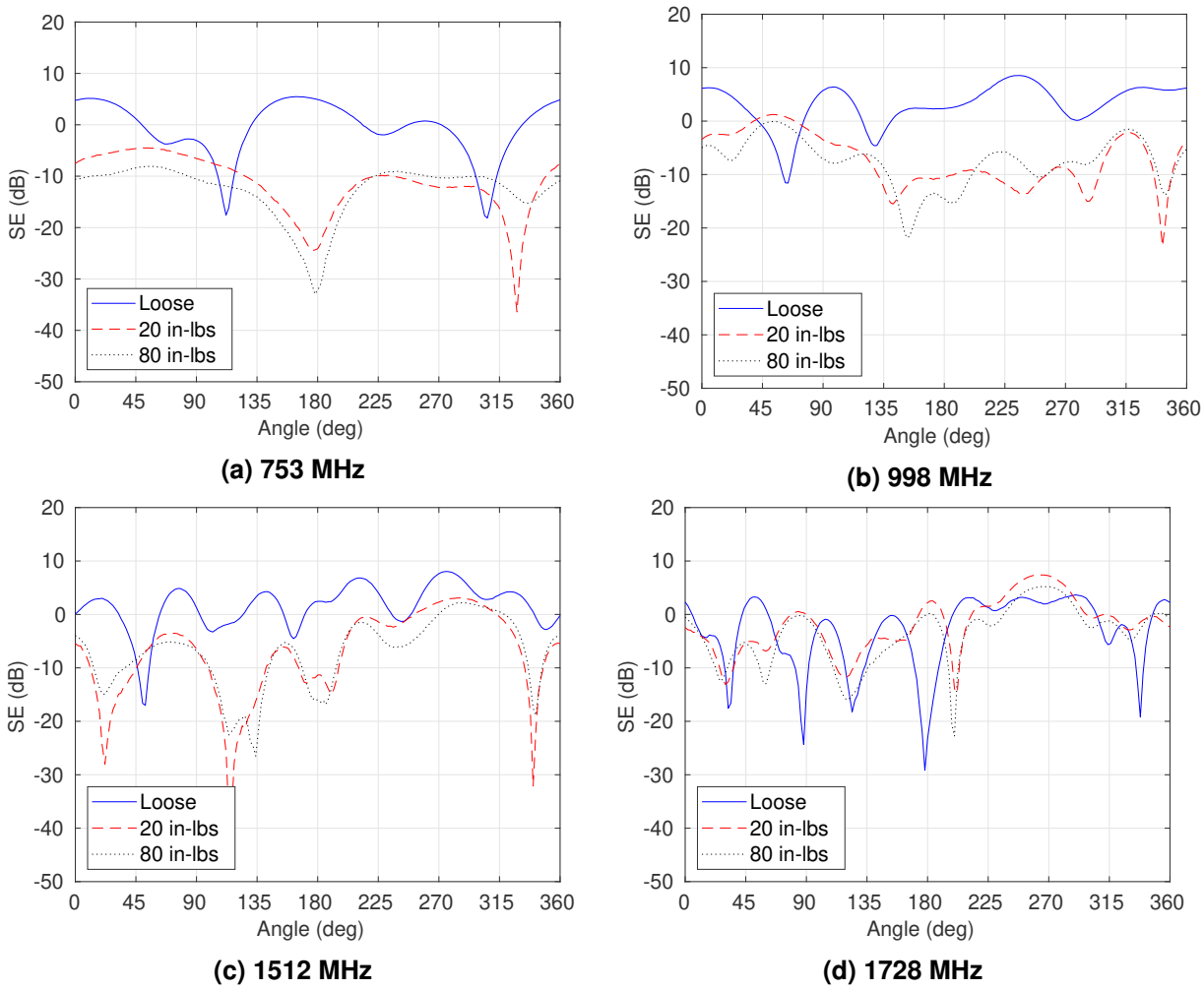

Figure 5-9. SE of Vessel 2 as a function of plane-wave incidence angle and bolt torque for bolts without shims.

shims, torque played a relatively weak role in the structure of the near fields leaking from the slot. Here we see that in the more realistic case of no shims, torque plays a strong role in the structure and level of the fields in the slot. As expected, the intensity of fields leaking from the slot decreases with increasing torque. Also, the distribution of slot fields becomes very complicated when the bolts are fully torqued, exhibiting many local minima that suggest the presence of numerous random contact points along the slots.

Despite the more complex field pattern, the presence of good contact still can be seen at the bolt positions at 45°, 135°, 225°, and 315°. However, the nulls seen at the bolt positions tend to be sharper here than in the case of shims.

Figure 5-9 shows the peak SE for four bands of interest as a function of plane-wave incidence angle and torque. It is important to note that the SE measurements were performed directly after the near-field scan for each torque value without moving Vessel 2 or changing bolt torque. For this reason, we should expect the slot configuration to be identical during the near-field scan and the subsequent SE measurement, allowing near-field and SE scans to be directly compared.

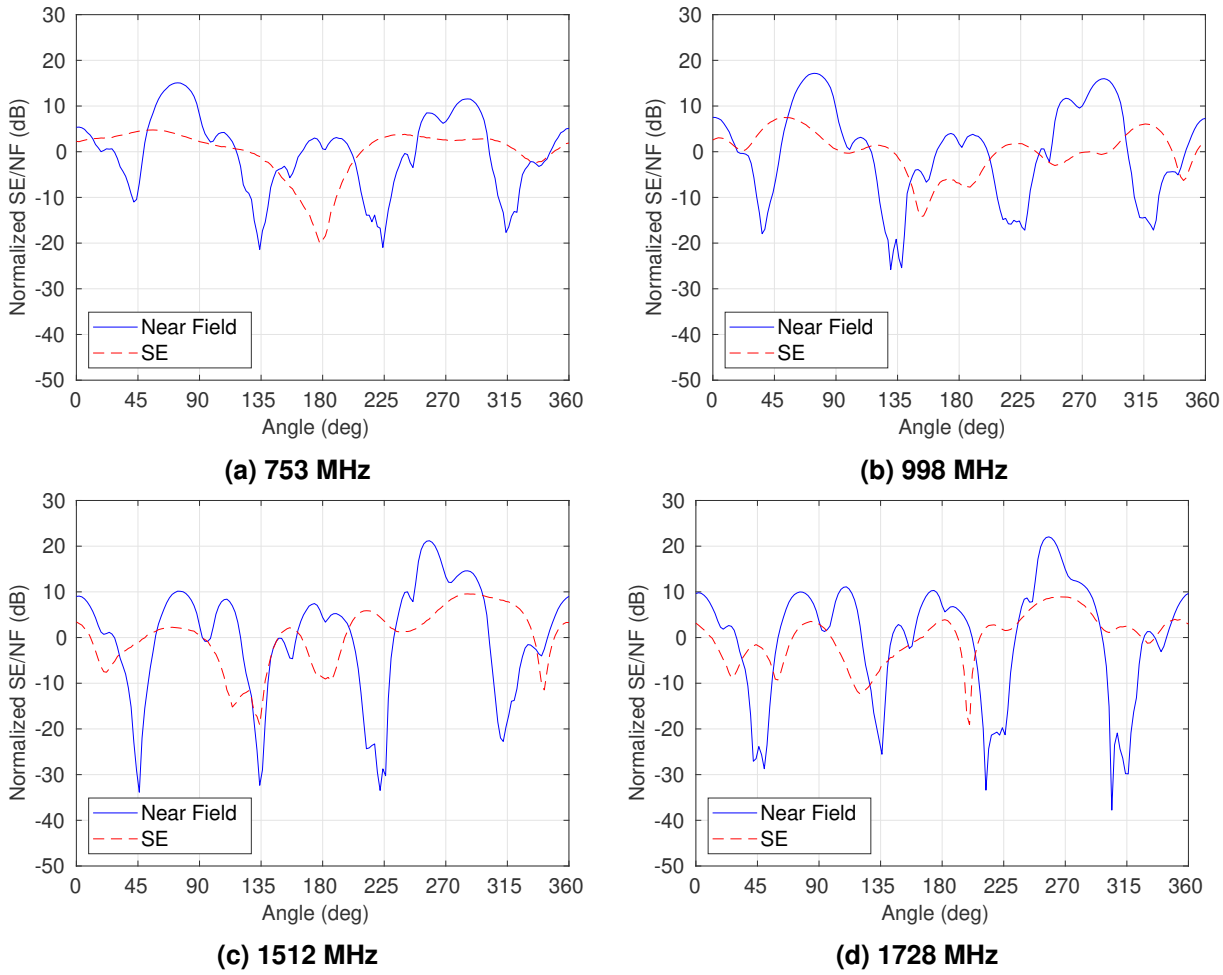

Figure 5-10. Near-field and SE variation with respect to scan angle for Vessel 2 without shims and bolts torqued to 80 in-lbs. Each curve has been normalized so the average value is 0 dB.

As expected, we see overall that SE decreases with increasing bolt torque. Interestingly, the direction of highest SE (highest EM penetration) changes as the bolts are torqued. The variation of SE with respect to incidence angle tends to be smoother than the near-field scanning information. This might be expected due to the fact that SE is a far-field measurement where the contribution of waves from many near-field directions are combined at each angle, leading to a smoother response.

To see the SE smoothing effect more clearly, Figure 5-10 plots near fields and SE values for 80 in-lbs of torque on the same axes for each of the four bands. For comparison, SE and near fields have been normalized to have an average value of 0 dB. As can be seen, the near-field scans exhibit a more complicated pattern relative to the smoother SE plots. This suggests that more detailed information can be collected about the slot behavior in the near field than with a far-field SE measurement. It is also worth noting that the dynamic range of near-field measurements is larger in general than the SE measurements, likely due to the mixing of fields that was mentioned previously. Finally, it is interesting to note that points of highest "leakage" in the near field do not

usually correspond to the angle of incidence giving peak SE. Although this might seem surprising at first, an SE measurement value results from a coherent sum of waves that penetrate different parts of the slot. The angles at which these multiple waves add up constructively will be somewhat random and not necessarily correlated with the direction of peak near-field leakage.

5.3.2. Fitting to Slot Models

Given the complicated structure seen in the slot fields shown in Figure 5-8, it is not possible to extract meaningful contact resistance parameters using the simple method that was used previously for a controlled slot width. However, it is of interest to explore whether the circuit-based slot models in Appendix D can capture the behavior seen in measurements.

To this end, a genetic algorithm (GA) was used to optimize contact point locations and conductance of those contact points for the 1D and 2D circuit models described in Appendix D. For simplicity, code for the 2D formulation was used for both 1D and 2D simulation, where one and five elements were used along the slot depth dimension for the 1D and 2D cases, respectively. A total of 180 circuit elements were used around the circumference of the cylinder, giving a resolution of 2° per element. The Green's function operator discussed in Appendix D was used to convert slot voltages to the fields that would be observed 5 mm from the slot. A constant slot width of 0.002-inch was assumed.

The GA optimizes both the positions and conductances of 50 contact points, where the value of 50 was chosen to be large enough to allow significant variation of the model behavior, but not too large to possibly overfit the data. Element conductance at contact points was allowed to vary over the range of 1 to 10,000 Ω^{-1}. A population size of 50 was used with a maximum of 500 iterations per run of the code.

The GA was run in three stages, where mutation/crossover probabilities and mutation variance for the contact positions and conductances were set to be incrementally smaller for each successive stage. Currently the GA developed here requires user interaction to run the code multiple times for each stage until the user decides that the fit is good enough to proceed to the next stage. A more ideal implementation would determine the required stage and number of iterations automatically.

Figure 5-11 shows the result of the GA fitting of the 1D and 2D models to the no shim near-field measurement of Vessel 2 for the case of 80 in-lbs of torque. The results show that very good agreement can be obtained between the modeled and the measured near fields. Visually comparing the 1D and 2D results, it can be seen that very similar contact point locations have been selected by the GA algorithm for the 1D and 2D cases.

The coincidence of contact points in the GA-optimized 1D and 2D models is further illustrated in Figure 5-12, which plots the optimized conductance at each contact point for the two models. For the case of the 1D model, there is a single conductance for a given contact angle, which is the value plotted. For the 2D model, there can potentially be multiple contact points along depth for a single angle, and the mean of those conductances is shown in the plot. The plot further highlights how similar contact point locations are selected by the GA for the 1D and 2D models. However,

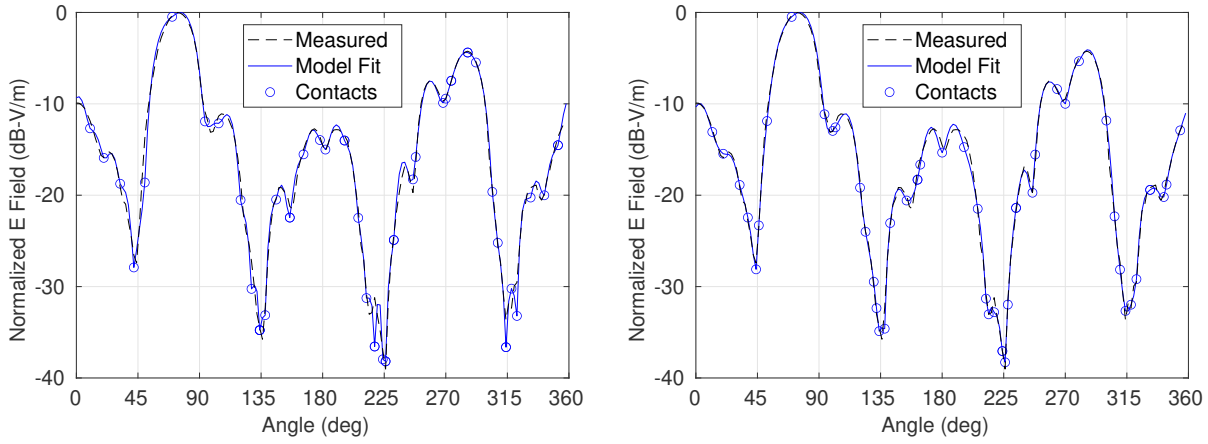

(a) 1D **(b) 2D**

Figure 5-11. Genetic algorithm (GA) optimized fit of the (a) 1D and (b) 2D circuit models to a measured near-field scan of Vessel 2 with no shims and 80 in-lbs of torque.

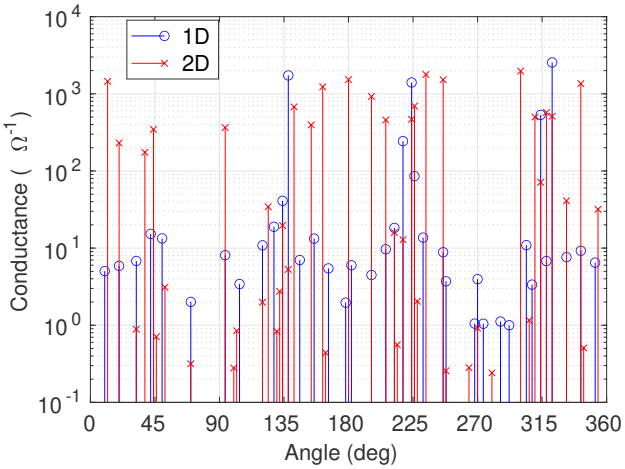

Figure 5-12. Contact points and associated conductances in the final GA-optimized fit of the 1D and 2D circuit models.

the conductance level can be quite different in the 1D and 2D models. This suggests that in the case of an uncontrolled slot, the slot conductance is likely less important than the contact position. Further, the differences in the fit of the 1D and 2D cases suggest that the single near-field probe measurement is insufficient to unambiguously determine a complicated slot configuration. It is expected that more information will be needed to reduce this model ambiguity. For example, the following additional information could be used:

- Response of magnetic field probes.
- Near-field scans of all 3 Cartesian field components.
- Responses at multiple frequencies.

The ability to obtain an unamiguous contact model by incorporating as much near-field information as possible could be explored in future work.

5.3.3. Differential Probe Measurements

Before ending this chapter, we briefly explore the use of the differential dipole probe described in Section 4.3.3 to measure near fields of Vessel 2. One concern of using the skirt probe is the relatively large skirt that could affect the spatial resolution of the probe. Although the dipole probe should measure the same axial E-field component as the skirt probe, it is more compact as it does not require the large balun feature.

Figure 5-13 compares normalized near-field scans using the skirt and dipole probes, each placed 5 mm from the flange. Here, the measurement was performed without shims, with bolts torqued to 80 in-lbs. The near-field plots look very similar for the skirt and dipole probes for the four different bands plotted. Some discrepancies are seen in the deep nulls seen at bolt locations. The noise floor level for the two probe types is indicated by the horizontal lines in the plots, and sometimes SNR at bolt locations is rather low, partially explaining the disagreement. However, the overall comparison shows that the skirt probe does not significantly reduce spatial resolution of probed fields, which was the main reason for checking results with the more compact dipole probe.

5.4. Conclusion

This section has explored near-field measurement of Vessel 2 as a way of extracting the contact resistance of joints. The case of Vessel 2 with 5-mil shims was studied in the most detail, where it was found that contact resistance at the bolted joints can be effectively extracted using information from near-field scans for the lowest resonance at 753 MHz. Using the extracted resistance value of 0.1 Ω also provided a good fit between measured and simulated shielding effectiveness. This result incidates consistency between the near-field behavior at the joints, from which resistance is extracted, and the far-field radiation behavior of the slots.

Vessel 2 was also measured without shims, where it was observed that the structure and intensity of near fields depended strongly on bolt torque and that a random and complicated contact pattern

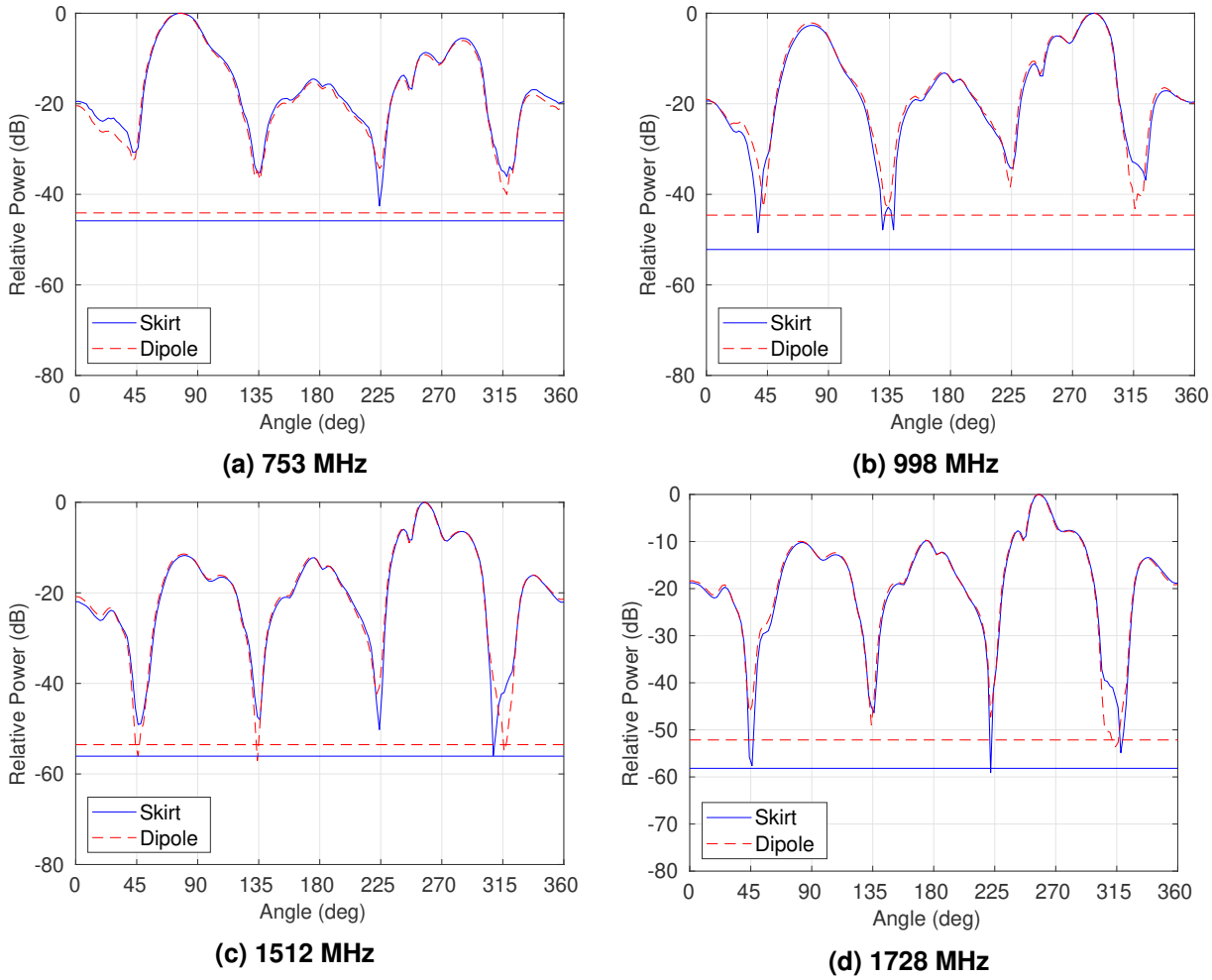

Figure 5-13. Near-field scans of the no-shim case of Vessel 2 performed with the skirt and dipole probes. Each probe type was placed 5 mm from the flange in a separate measurement run. Horizontal lines show the noise floor of the measurement for the two probe types.

likely exists in the slot. It was demonstrated that the behavior of near fields for this no shim case can be captured using the 1D and 2D circuit models for the slot models presented in Appendix D. Measurements of Vessel 2 without shims were performed with both the skirt probe and a more compact dipole probe, showing that the spatial resolution of the skirt probe is not significantly lower than the dipole probe for the frquency bands and measurement configuration considered herein.

6. LAP JOINT VESSEL MEASUREMENTS

6.1. Introduction

In this chapter, near-field measurements are presented for the Lap Joint Vessel. This vessel has a more complex joint, which when bolted together creates a slot that is a tortuous path. Only limited analysis of Lap Joint Vessel was performed in this work, and it is left for future work to model and extract meaningful slot parameters for this vessel type. See Section A.2 in Appendix A for information on the Lap Joint Vessel geometry.

As with Vessel 2, the Lap Joint Vessel was measured using the semi-anechoic setup described in Chapter 4, providing correlated near-field and shielding effectiveness (SE) measurements. Near-field measurements presented in this chapter used the dipole probe (described in Section 4.3.3) at 5-mm distance, as opposed to the skirt probe.

6.2. Frequency Response

First we consider the frequency response of the Lap Joint Vessel. The dimensions of the cylindrical cavity are identical to Vessel 2, having a radius and height of 6 and 18 inches, respectively. The frequency response of the near-field amplitude is shown in Figure 6-1 for four frequency bands of interest. Here, the probe scan angle has been chosen for each band and vessel type that gives the maximum amplitude. The plots also show a measurement that gives an estimate of the combined noise, interference, and cable coupling level, which was accomplished by disconnecting the cable to the 1 cm probe in the vessel and terminating the cable with a 50 Ω load. Note that peak SNR of the near-field measurements is approximately 40 dB or better for all of the measurements, allowing fairly deep nulls to be measured.

Table 6-1 shows numerical values of the resonant frequency (f_0), signal level (E_0), and quality factor (Q) for each vessel type for the five lowest resonances. Signal level is the highest for Vessel 2 with shims (as expected), and lowest for Vessel 2 without shims. It is interesting that the signal level for the Lap Joint Vessel falls between the cases of Vessel 2 with and without shims. For each frequency band, quality factor is comparable for the different vessel cases, with two notable exceptions: Q appears to be very high for Vessel 2 without shims for the TM_{010} mode near 753 MHz, which is the main resonance considered in this work. The much higher Q could be explained by fairly tight sealing of the flange with no shims, leading to less energy loss, and higher stored energy. The other case showing an unexpected change in Q is the TM_{012} resonance, where Q is much lower for the Lap Joint Vessel compared to the Vessel 2 cases. Here it is unclear what could cause this large difference.

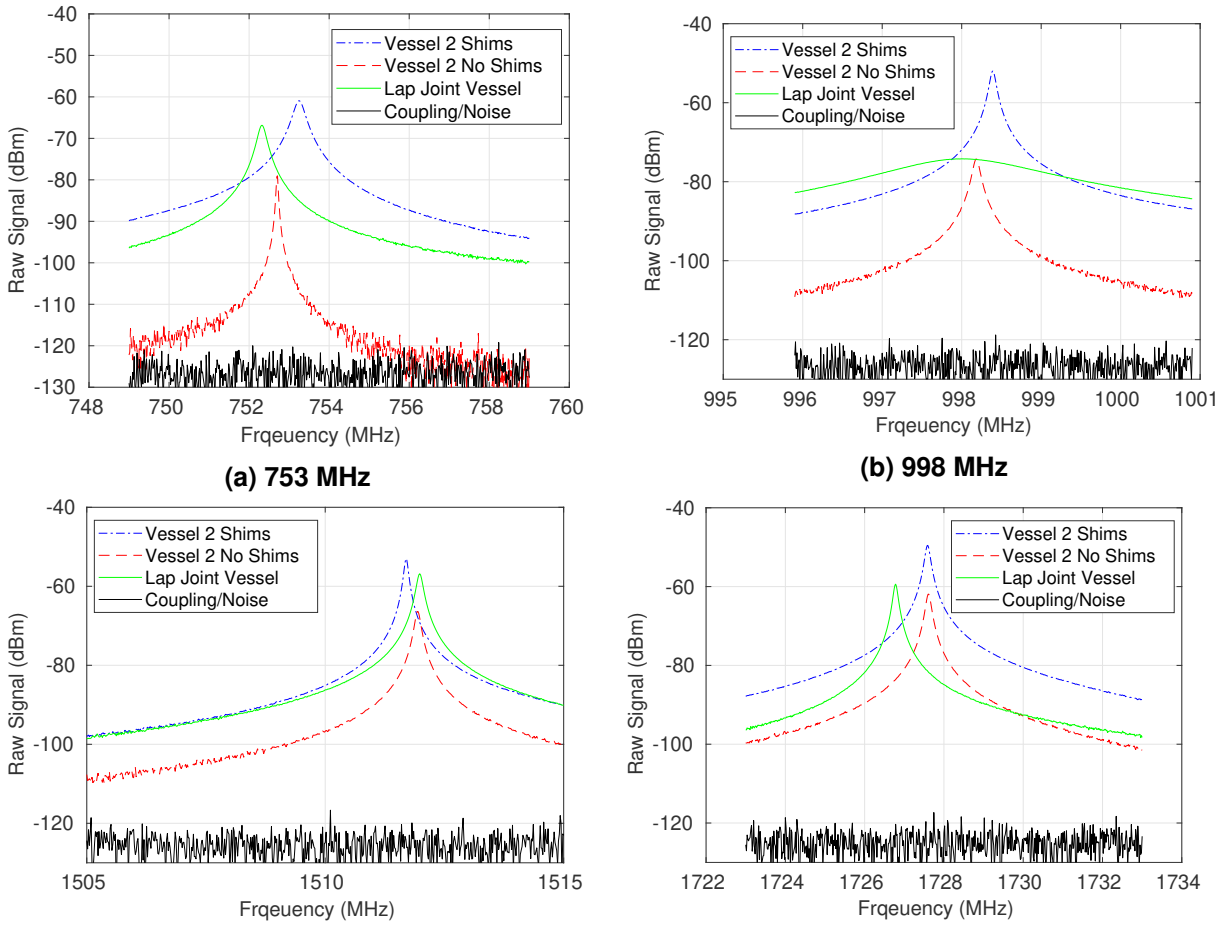

Figure 6-1. Peak signal level seen in near-field measurements of Vessel 2 and the Lap Joint Vessel for four bands of interest. The near-field scan angle used was the one giving highest signal power in each case.

TM_{010}: 752.68 MHz			
	f_0	E_0	Q
Vessel 2 Shims	753.22 MHz	-60.7 dBm	2743
Vessel 2 No Shims	752.71 MHz	-79.0 dBm	14655
Lap Joint Vessel	752.34 MHz	-67.6 dBm	2822
TM_{012}: 998.11 MHz			
	f_0	E_0	Q
Vessel 2 Shims	998.39 MHz	-52.0 dBm	12432
Vessel 2 No Shims	998.18 MHz	-74.2 dBm	10859
Lap Joint Vessel	998.06 MHz	-74.2 dBm	546
TM_{014}: 1511.74 MHz			
	f_0	E_0	Q
Vessel 2 Shims	1511.69 MHz	-53.0 dBm	16793
Vessel 2 No Shims	1511.95 MHz	-66.4 dBm	12162
Lap Joint Vessel	1511.98 MHz	-56.8 dBm	11168
TM_{020}: 1727.71 MHz			
	f_0	E_0	Q
Vessel 2 Shims	1727.58 MHz	-49.5 dBm	12541
Vessel 2 No Shims	1727.62 MHz	-61.9 dBm	12173
Lap Joint Vessel	1726.78 MHz	-59.4 dBm	13971
TM_{022}: 1847.89 MHz			
	f_0	E_0	Q
Vessel 2 Shims	1847.48 MHz	-47.9 dBm	7585
Vessel 2 No Shims	1847.58 MHz	-63.3 dBm	8223
Lap Joint Vessel	1846.79 MHz	-56.4 dBm	8680

Table 6-1. Comparison of resonances of Vessel 2 (with and without shims) and the Lap Joint Vessel for the five lowest resonances. Data was extracted from near-field scans using the scan angle giving the maximum response. The expected (analytical) resonant frequency is given in the heading for each mode/band.

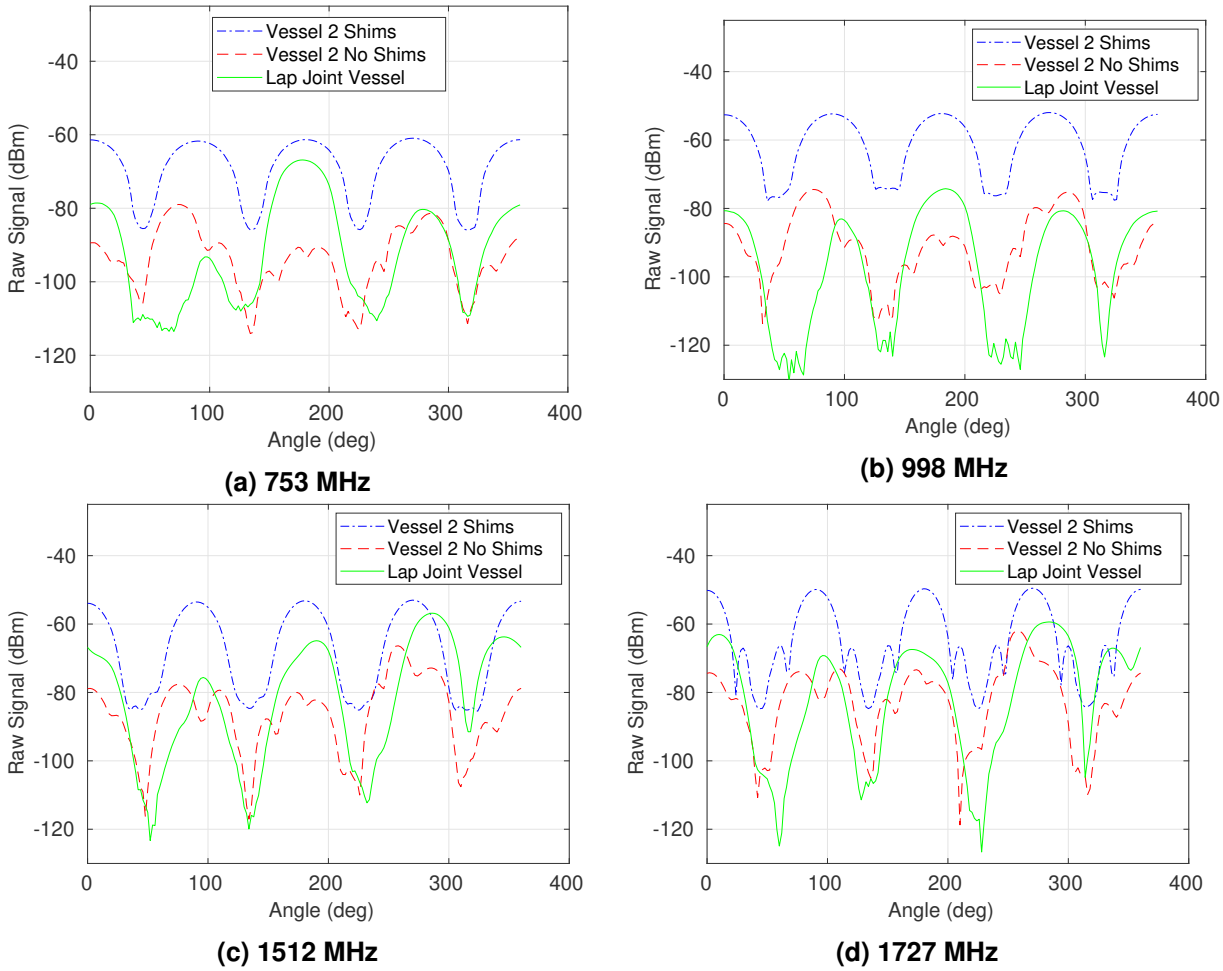

(a) 753 MHz

(b) 998 MHz

(c) 1512 MHz

(d) 1727 MHz

Figure 6-2. Variation of near-fields with scan angle at the resonant peak for four frequency bands.

6.3. Near-field Measurements

Figure 6-2 compares the variation of raw near-field measurements for the three different vessel cases. Clearly the variation of near fields for Vessel 2 with shims has the most regular behavior, and therefore is the easiest to model. In the case of no shims, it is interesting that the behavior of Vessel 2 appears to be more complicated than the Lap Joint Vessel. Specifically, Vessel 2 has many more local minima and maxima in each slot, suggesting more contact points than are present in the Lap Joint Vessel.

6.4. Conclusion

This section has briefly considered measurements of the Lap Joint Vessel, which has a complicated "tortuous slot" structure at the joint. The resonant response of the Lap Joint Vessel was similar to that of Vessel 2, except that Q was surprisingly low for the TM_{012} mode. Near-field

scans were performed for the Lap Joint Vessel, where less spatial variation of the Lap Joint Vessel fields was observed as compared to Vessel 2 without shims. This result suggests that that the Lap Joint Vessel has fewer contact points than Vessel 2 in the no-shim case.

7. VIBRATION MEASUREMENT

7.1. Introduction

This report has demonstrated the ability to extract high-resolution spatial information about slot fields using near-field scanning. The techniques developed so far can reveal information about slot contacts for a static vessel, i.e., one whose mechanical properties are not varying in time. In an end-of-year review of this LDRD project, it was suggested that vessels with time-varying mechanical properties should be studied, and that the near-field scanning technique should be extended to allow vessels under vibration to be probed, relating to the combined enviornments effort at Sandia [9]. To this end, this chapter explores a novel method for performing near-field slot measurements that allows the *time variation* of fields near slots to be tracked with high temporal resolution, possibly providing the key information required to understand the complex interaction of mechanical vibration, slot deformation, and the resulting modulation of EM fields.

An existing technique used at Sandia for measuring the EM response of vessels under vibration is shown in Figure 7-1 [9]. Typically, piezoelectric transducers are used to generate an acoustic resonance on the vessel, which in turn slightly modulates the shape of the vessel and slots, thus modulating EM fields as well. The degree of modulation of the EM response is probed by exciting the vessel with a high-power incident plane wave having a single frequency f_0. The internal vessel field is then measured using an internal field probe connected to a high-speed digital sampling oscilloscope (DSO). A hypothetical modulated EM waveform measured with this approach is shown in Figure 7-2. A simple amplitude demodulation operation can then be applied to this waveform, where $A_{\min}(f_0)$ and $A_{\max}(f_0)$ are the minimum and maximum envelope with respect to time, respectively, of the time-varying signal for illumination frequency f_0. The AM depth in the waveform seen at frequency f_0 can be computed as

$$\mathrm{AM}(f_0) = \frac{A_{\max}(f_0) - A_{\min}(f_0)}{2A_{\mathrm{avg}}(f_0)}. \tag{7.1}$$

where $A_{\mathrm{avg}}(f_0) = [A_{\max}(f_0) + A_{\min}(f_0)]/2$. The excitation frequency f_0 is then stepped in very fine increments in order to obtain $\mathrm{AM}(f)$ over a band of interest, where f usually covers a bandwidth of a few MHz centered on an EM cavity resonance.

The existing technique described above is straightforward and provides a direct measurement of AM. However, it is difficult to deduce what is physically happening to the vessel shape and slots under vibration using only $\mathrm{AM}(f)$. Figure 7-3 illustrates how AM at a cavity resonance can occur due to time-variation of the set of resonant parameters $\Psi = \{\nu_0, E_0, Q\}$, where ν_0 is the resonant frequency, E_0 is the resonant amplitude, and Q is the quality factor. Knowing the joint time evolution of Ψ, or $\Psi(t)$, would lend significant insight into what is physically happening to the

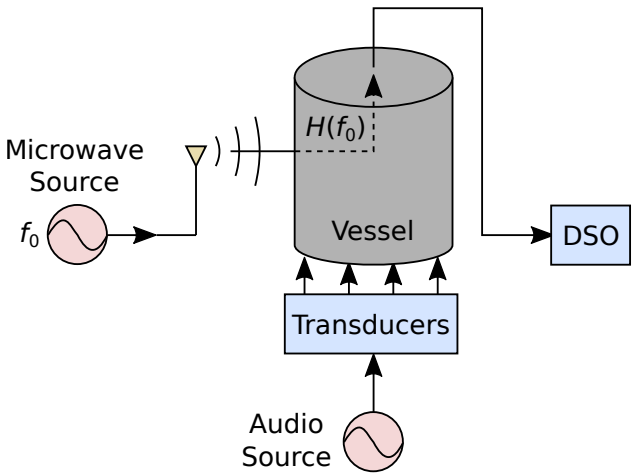

Figure 7-1. Existing measurement technique for characterizing modulation of EM response under vibration.

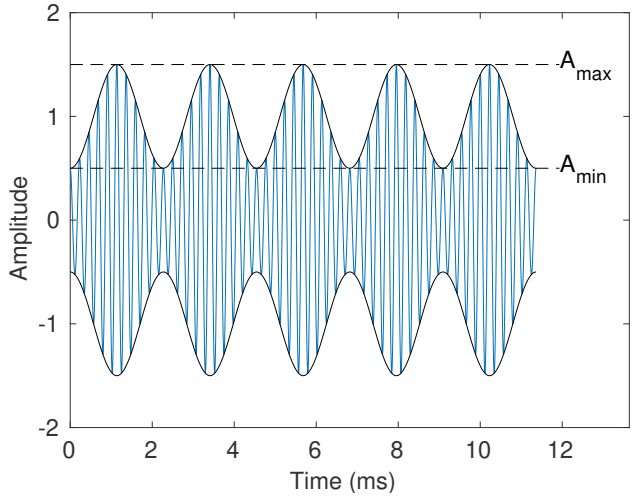

Figure 7-2. Hypothetical EM signal resulting from a cavity response modulated by mechanical vibrations. In this example, the amplitude modulation (AM) depth is set to $\mathrm{AM}(f_0)$ = 50%.

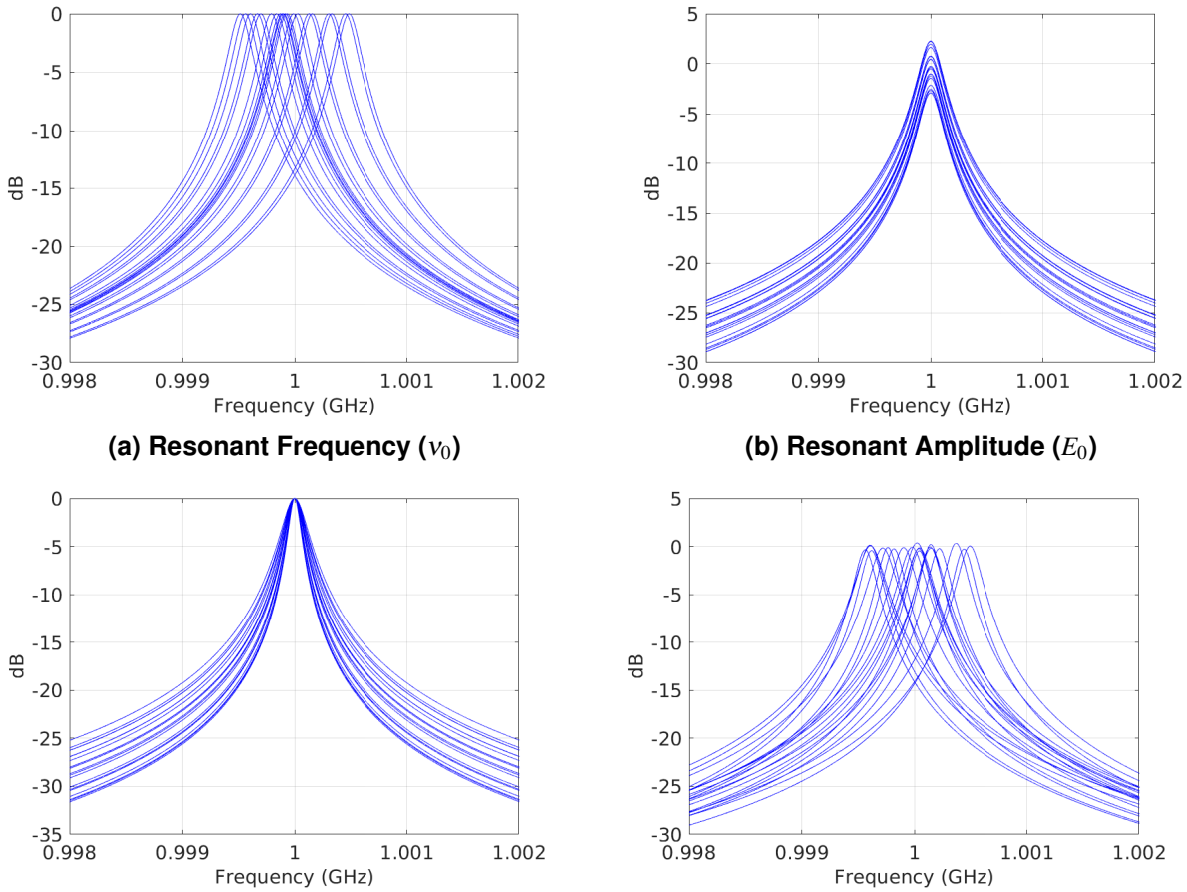

(a) Resonant Frequency (ν_0)

(b) Resonant Amplitude (E_0)

(c) Quality Factor (Q)

(d) Combined

Figure 7-3. Simulation of the random variation of the frequency response at a single resonant peak with respect to (a) the resonant center frequency ν_0, (b) the amplitude of the resonant peak E_0, (c) the quality factor Q, and (d) the combined variation of ν_0, E_0, and Q. Each plot shows 20 random realizations of the frequency response, where the parameter under consideration has a uniform random distribution.

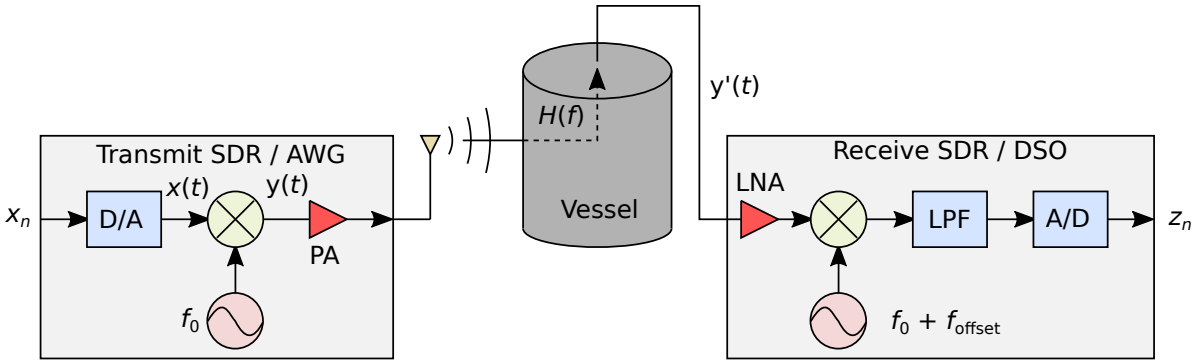

Figure 7-4. Basic multitone measurement setup.

slot and cavity under vibration, much more than can be extracted from AM that can obscure details of $\Psi(t)$.

The purpose of this chapter is to develop and demonstrate a method for measuring $\Psi(t)$ directly, providing more information about deformation of slots and vessels that occurs under vibration than can be obtained from AM plots. Combining high-resolution temporal sampling of the $\Psi(t)$ with the near-field scanning concept would then extend the slot-probing and parameter estimation concepts that have been developed previously to the dynamic case of vessels under vibration.

7.2. Multitone Probing

One method that has been used for probing the frequency response of propagation channels with high temporal resolution is to use waveforms consisting of a series of superimposed sinusoids, referred to herein as a "multitone" signal (see [5]). Unlike a VNA or spectrum analyzer measurement that uses a fairly slow frequency sweep to probe a finite bandwidth, the multitone signal allows numerous frequency points to be measured rapidly and simultaneously. The basic measurement setup is depicted in Figure 7-4, where a baseband digital multitone signal x_n is used as the probing waveform, represented mathematically as

$$x_n = \sum_{k=1}^{N_{\text{tone}}} a_k \cos\left(\frac{2\pi f_k n}{f_s} + \phi_k\right), \quad n = 0,\ldots,N-1, \tag{7.2}$$

where N_{tone} is the number of tones in one sideband, a_k, f_k, and ϕ_k are the amplitude, frequency, and phase of the kth tone, and f_s is the transmit sample frequency. The kth term in (7.2) actually produces two tones at $\pm f_k$, so that the waveform x_n has $2N_{\text{tone}}$ tones in total. The digital baseband waveform x_n is "up-converted" to a center frequency f_0 by performing digital-to-analog (D/A) conversion to obtain the continuous waveform $x(t)$, followed by multiplication by a carrier with frequency f_0, or

$$y(t) = x(t)\cos(2\pi f_0 t), \tag{7.3}$$

where the center frequency f_0 is chosen in this work to coincide with an EM cavity resonance of interest. The signal $y(t)$ is likely amplified with a power amplifier (PA) and then used to drive a transmit antenna that illuminates the vessel.

Typically, software-defined radios (SDRs) and arbitrary waveform generators (AWGs) programmed with a signal x_n having a finite record length of N samples can be set to a continuous output mode, where a signal of infinite duration x'_n is generated by repeating the signal (7.2) after every N samples, or

$$x'_n = x_{[(n-1) \bmod N]+1}. \tag{7.4}$$

On the receive side, the signal is "down-converted" to baseband by amplifying the signal with a low-noise amplifier (LNA), multiplying by a complex carrier having frequency $f_0 + f_{\text{offset}}$, and performing a low-pass filter (LPF) operation. Note that the down-conversion operation is often performed using multiple stages in practice, but such details are not relevant for the present discussion. The down-converted signal is converted to a digital signal using an analog-to-digital (A/D) converter, producing the digital output z_n. In an SDR, the complete amplification and down-conversion process is performed by the SDR hardware and software. However, if a high-speed DSO is used, the receive signal $y'(t)$ must be sampled at a sample rate of $2f_0 + f_s$ or higher to avoid aliasing, which can be many GS/s. The multiplication with the complex carrier and low-pass filtering must then be performed in software.

Uniform coverage of a frequency band is accomplished by enforcing a constant frequency separation Δf between tones, or

$$f_k = \Delta f/2 + (k-1)\Delta f, \quad k = 1, \ldots, N_{\text{tone}}. \tag{7.5}$$

By placing the first tone at $\Delta f/2$, we keep a frequency separation of Δf between the tones that are realized at $\pm\Delta f/2$, thus providing a separation of Δf between all adjacent tones.

Power amplifiers that are used in measurements usually have a non-linear response. For a continuous-wave (CW) probing signal, a PA can often be operated in saturation without detrimental effects. However, for a complex signal like that given by (7.2), a non-linear PA will effectively clip time-domain peaks of the signal, leading to distortion. The typical solution is to reduce the input signal to the PA to a level where the output power is well below saturation and the response is effectively linear, a method known as "backoff." For example, a PA with a saturated output power of 20 dBm could be operated at an output power of 10 dBm (10 dB backoff) to provide good linearity. The amount of backoff required is related to the sharpness of peaks in the signal, which can be quantified using the peak-to-average ratio of the signal, given by

$$\text{PAR} = \frac{N \max_n(x_n)}{\sum_{n=1}^{N} |x_n|}, \tag{7.6}$$

where N is the number of nonzero samples in the time window. In this work, the PAR is minimized by generating 1000 different multitone signals having uniform random phases for the tones (ϕ_k). The waveform that results in the lowest PAR is the one that is kept.

Table 7-1 shows the parameters of the multitone signal that were used in this work. The resulting time-domain waveform and single-sided frequency-domain spectrum are shown in Figure 7-5 (a) and (b), respectively. The PAR of the realized waveform is 2.3. By comparison, a single sinusoid has the lowest possible PAR value of 2.0.

Parameter	Variable	Value
Number of tones	N_{tone}	17
Sample rate	f_s	4.096 MS/s
Time samples	N	1024
Length of signal	$T = N/f_s$	250 μs
Spacing of tones	Δf	25.6 kHz
Total bandwidth	B	800 kHz

Table 7-1. Parameters of the multitone signal used in this work.

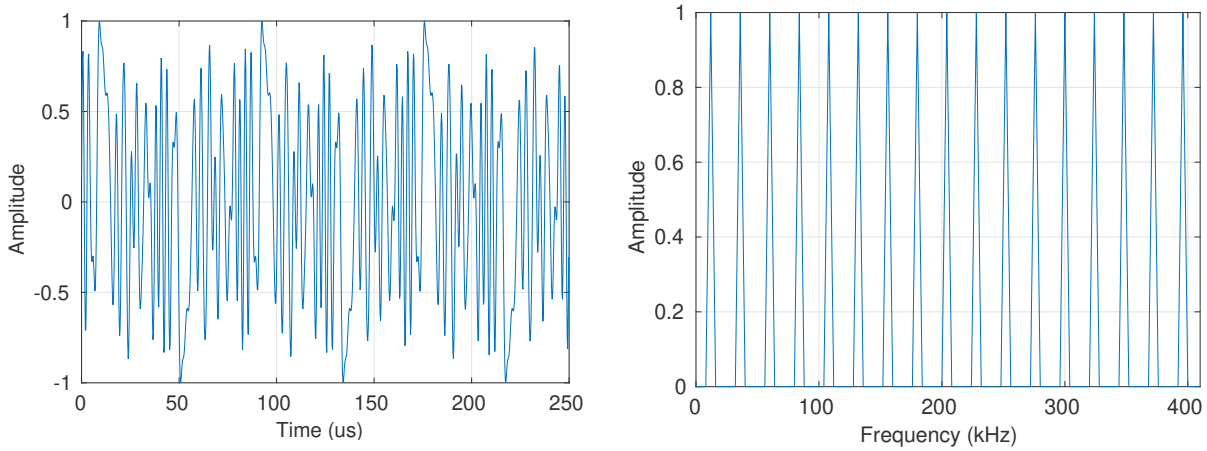

(a) Time-domain Signal

(b) Frequency-domain Signal

Figure 7-5. Multitone signal used in this work: (a) time-domain signal, and (b) one-sided frequency-domain spectrum.

Our goal here is to use the output waveform z_n in Figure 7-4 to estimate the time-varying voltage transfer function $H(f,t)$. In this chapter we will refer to the quantity $|H(f,t)|^2$ as the *power transmission coefficient* from the transmit antenna port outside the vessel to the output port of a probe embedded in the vessel. This quantity serves the same purpose as $|S_{21}(f)|^2$ in a VNA measurement and can be appropriately scaled to give SE when the transmit antenna is in the far field of the vessel (see Appendix E).

The time variation of $H(f)$ is obtained by processing successive records of temporal length $T = N/f_s$, providing estimates of the sampled frequency response $H(f, pT)$, where $p = 1, \ldots$ is the record number. We begin with the sampled down-converted complex baseband signal, which is of the form

$$z_n = \sum_{k=1}^{N_{\text{tone}}} a_k \big\{ H_{\text{raw}}(f_0 + f_k) \exp[j2\pi(f_k + f_{\text{offset}})(n/f_s' - \tau) + j\phi_k] + H_{\text{raw}}(f_0 - f_k) \exp[j2\pi(-f_k + f_{\text{offset}})(n/f_s' - \tau) - j\phi_k] \big\}, \tag{7.7}$$

where $H_{\text{raw}}(f)$ is the raw complex frequency response of the vessel and probing hardware at frequency f, f_{offset} is an offset frequency due to error between the center frequency used for up-conversion at transmit and down-conversion at receive, τ is a time delay between the transmit and receive hardware, and f_s' is the receive sampling rate. For this development it is assumed that f_s and f_s' are harmonically related, i.e., either f_s'/f_s or f_s/f_s' is a positive integer.

We next show how the instantaneous frequency response of the first record $H(f,0)$ can be obtained using the FFT of (7.7) using the samples $n = 0, \ldots, N' - 1$, where $N' = f_s' T$. Ideally, we would like to remove the effect of cables, SDR hardware, and antennas from the response $H_{\text{raw}}(f)$ to obtain $H(f)$. This can be approximately achieved using a simple through calibration procedure, where the transmitter output is temporarily connected to the receiver input through a known power attenuation L. This produces the "calibration signal"

$$z_{\text{cal},n} = \sum_{k=1}^{N_{\text{tone}}} \frac{a_k}{\sqrt{L}} \big\{ H_{\text{sys}}(f_0 + f_k) \exp[j2\pi(f_k + f_{\text{offset}})(n/f_s' - \tau) + j\phi_k] + H_{\text{sys}}(f_0 - f_k) \exp[j2\pi(-f_k + f_{\text{offset}})(n/f_s' - \tau) - j\phi_k] \big\}, \tag{7.8}$$

where $H_{\text{raw}}(f) = H(f)H_{\text{sys}}(f)$, and $H(f)$ is the desired ideal frequency response from the transmit antenna input to the receive probe output. We next take shifted FFTs (zero frequency placed at the center of the spectrum) of N' samples of (7.8) and (7.7), denoted $Z_{\text{cal},\ell}$ and Z_ℓ, respectively, where ℓ is the FFT bin index. We can identify the mth peak in $Z_{\text{cal},\ell}$, which we denote as $\ell_{\text{peak},m}$. Note that the mth peak corresponds to the transmit frequency

$$f_{\text{tx,m}} = \begin{cases} f_0 - f_{N_{\text{tone}}-m+1}, & 1 \le m \le N_{\text{tone}}, \\ f_0 + f_{m-N_{\text{tone}}}, & N_{\text{tone}} + 1 \le m \le 2N_{\text{tone}}. \end{cases} \tag{7.9}$$

For tones with uniform frequency sampling according to (7.5), we have the mapping shown in Figure 7-6, which yields

$$f_{\text{tx},m} = f_0 + \Delta f \left(m - N_{\text{tone}} - \frac{1}{2} \right), \quad m = 1, \ldots, 2N_{\text{tone}}. \tag{7.10}$$

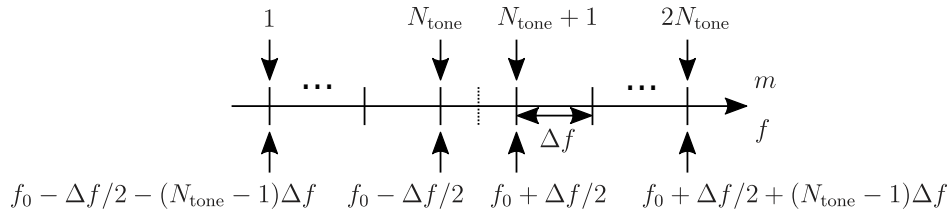

Figure 7-6. Mapping of successive receive peak number m to the corresponding transmit frequency f.

We can obtain $H(f_{\text{tx},m})$ by computing

$$H(f_{\text{tx},m})\exp(j\psi_0) = \frac{Z_{\ell_{\text{peak},m}}}{\sqrt{L}\, Z_{\text{cal},\ell_{\text{peak},m}}}, \tag{7.11}$$

where ψ_0 is a phase shift that depends on the relative Tx-Rx delay τ. The power frequency transfer function is then given by

$$|H(f_{\text{tx},m})|^2 = \frac{|Z_{\ell_{\text{peak},m}}|^2}{L\,|Z_{\text{cal},\ell_{\text{peak},m}}|^2}. \tag{7.12}$$

If $2N_{\text{tone}}$ frequency samples do not sufficiently resolve the resonant peak, the resonance fitting technique in Appendix C can be used.

Processing of the pth block to obtain an estimate of $H(f, pT)$ uses the same steps described previously, except that samples $(p-1)N'$ to pN' are used.

7.3. Measurement System Setup

The measurement setup that is used to illustrate multitone probing is depicted in Figure 7-7. The system components were fully surrounded with microwave absorber in the compact anechoic chamber. The up-converted multitone transmit signal was generated using an Analog Devices ADI ADRV9361 SDR evaluation module, which was fed directly to a log periodic antenna placed approximately 15 cm from the flange. The signal received on a 1 cm probe inside the vessel was fed to an inexpensive NooElec NESDR module that can sample 2.5 MHz of bandwidth centered from 25 MHz to 1.6 GHz. The reason for using two different SDRs is that in initial experiments the ADRV9361 was used for both transmit and receive, but it was found that the transmit/receive isolation was not sufficient for measuring SE. Bolts were torqued to 20 in-lbs in these experiments, where the rationale for the lower torque was to possibly see more effect from mechanical vibration. No shims were used at the bolt locations, also with the intent of seeing more modulation of EM fields due to vibration.

Mechanical vibration of the vessel was generated by placing an amplified loudspeaker (guitar amplifier) a few centimeters away from one of the ends of the vessel. The audio output from the laptop was used as the input to the audio amplifier. Two mechanical resonances of the vessel were identified by manually stepping the audio frequency in 1 Hz increments, where at resonance a

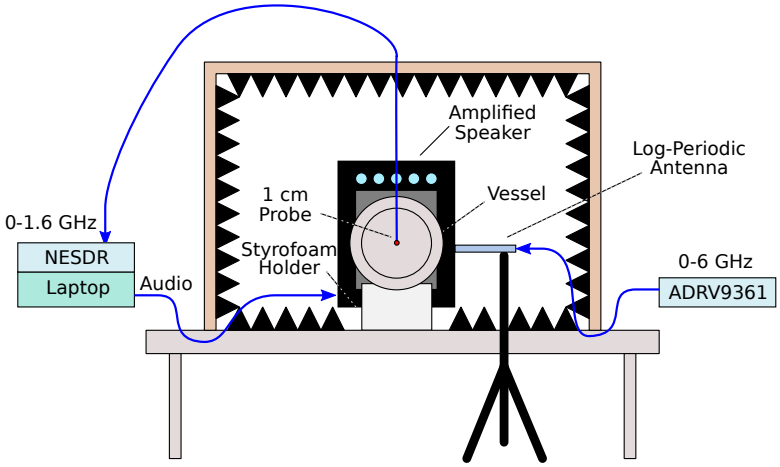

(a) Schematic

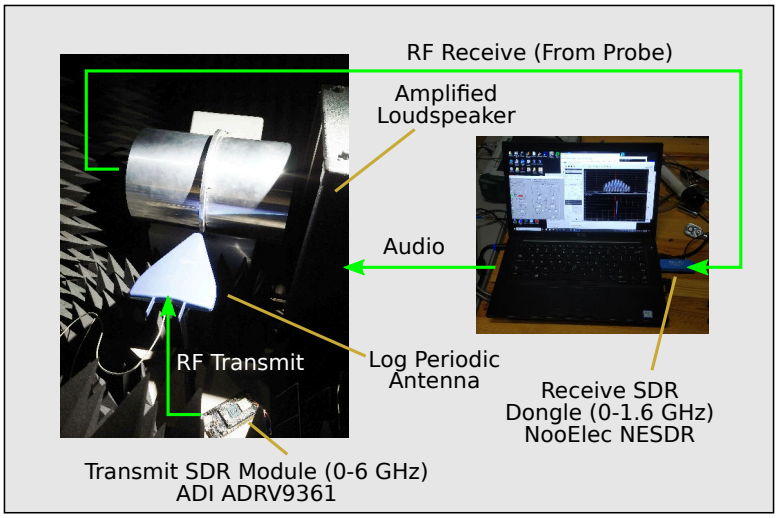

(b) Components

Figure 7-7. Measurement setup used to test the multitone probing idea in this work.

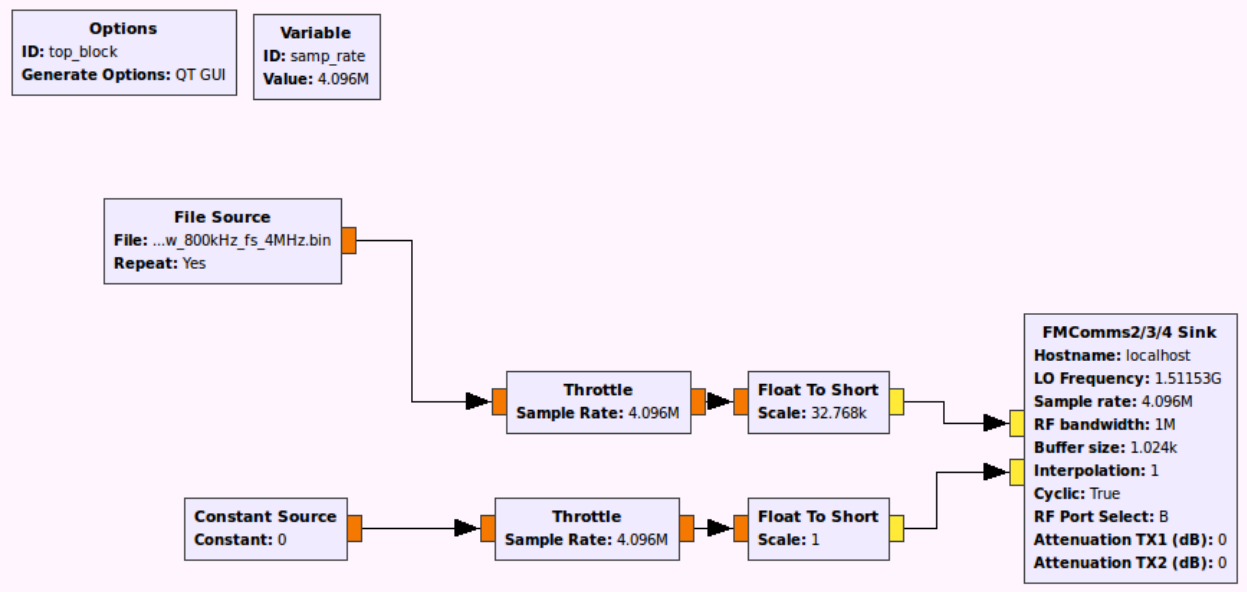

Figure 7-8. GNURadio block diagram that was used to control the transmit SDR module.

humming/rattling sound could be heard from the vessel. After identifying a coarse resonant frequency, steps in 0.1 Hz increments were performed to find a more exact resonant frequency. The existence of the mechanical resonances was more precisely identified by lightly touching the vessel walls with finger tips, where at resonance the vibration could be easily felt. Also, by probing with finger tips, it was possible to identify which part of the vessel was vibrating more strongly. At 415 Hz, strong vibrations were felt on the vessel sides and flange, and not on the vessel caps. At 853 Hz, vibrations were felt mainly on the top and bottom caps of the vessel and not on the sides of the vessel.

GNURadio was used to control the transmit SDR, and the GNURadio block diagram that was used is shown in Figure 7-8. The baseband input signal having a sample rate of 4.096 MS/s (see Figure 7-5) was used to drive the in-phase (I) channel of the transmitter. A constant value of 0 was fed to the quadrature (Q) channel. The FMComms Sink block was used to feed samples to the evaluation module, where the LO frequency was set successively to 753.218 MHz, 998.345 MHz, and 1511.629 MHz, which are three resonances of Vessel 2 that were found using a spectrum analyzer before this specific multitone experiment.

Figure 7-9 shows multitone output of the SDR for an LO frequency of 753.218 MHz as measured on a spectrum analyzer. The plot shows that the transmit signal scaling used in GNURadio provides LO feed through (the spur in the center of the spectrum) and out-of-band spurs that are 30 dB below the tones or better. Higher transmit scaling and signal power could be used, but it was found that this increased the spurs dramatically. Total transmit power in the multitone peaks is approximately 3.4 dBm, which gives an average of -12.9 dBm/tone. This relatively low transmit power per peak illustrates one of the tradeoffs of multitone probing: multiple frequency points can be simultaneously probed, but the SNR per frequency is lower than a swept measurement.

On the receive side, the freely available SDR# (SDR Sharp) program was used to control and

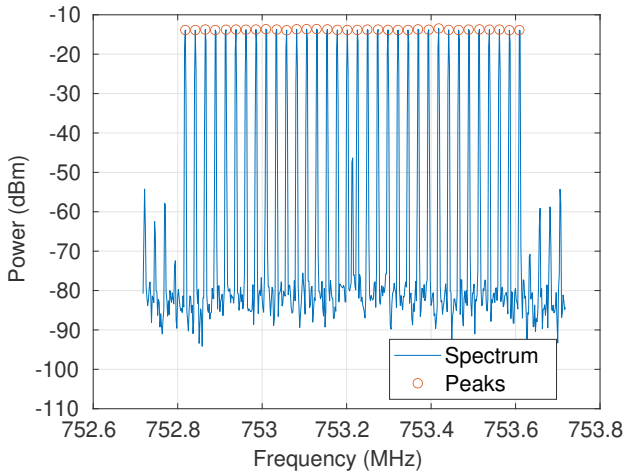

Figure 7-9. Multitone output of the SDR measured with a spectrum analyzer for an LO frequency of 753.218 MHz.

Parameter	Value
Sample rate	2.048 MS/s
RF gain	37.2 dB
Recording Mode	Baseband
Recording Format	16-bit PCM

Table 7-2. Key parameters used in the SDR# program with the NESDR receive dongle.

acquire data from the NooElec NESDR dongle. The LO frequency was chosen for each band to place the 18th tone as close as possible to zero frequency after down-conversion. Table 7-2 shows the parameters that were used with SDR#. The NESDR dongle only supports discrete sample rates up to 3.2 MS/s. The value of 2.048 MS/s was selected, sufficient to provide better than Nyquist sampling of the multitone signal, yet not too close to the limits of the hardware where performance may be poor. This receive sample rate then constrains the sample rate at the transmitter, where 4.096 MS/s was used to be twice the receive sample rate. The raw data acquisition mode of SDR# was used to stream I/Q data to an audio .wav file, which could then be processed in MATLAB.

7.4. Static Vessel Test

In this section, we check whether the multitone probing method can provide nearly the same information as a spectrum analyzer measurement. The setup in Figure 7-7 was used to measure the first resonance of Vessel 2 using the multitone parameters in Table 7-5. The through calibration procedure described in Section 7.2 was used to allow an absolute SE level to be obtained. The same probe, vessel, and antenna configuration was then measured using a spectrum analyzer with a tracking generator. In the following comparisons, five multitone snapshots are plotted to give an idea of the effective noise of the fast multitone probing.

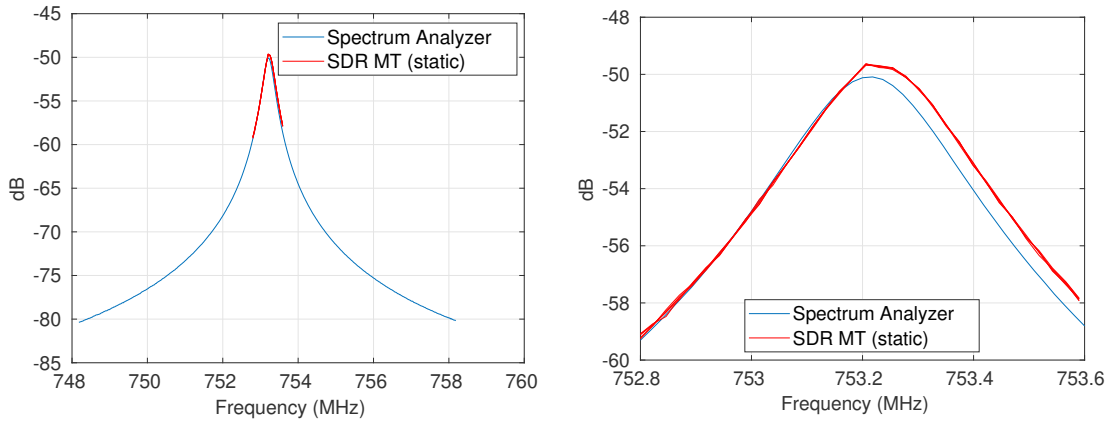

Figure 7-10. Comparison of multitone probing with a spectrum analyzer measurement of the first resonance of Vessel 2. Five consecutive snapshots of the multitone result are shown to give an indication of the effective noise level.

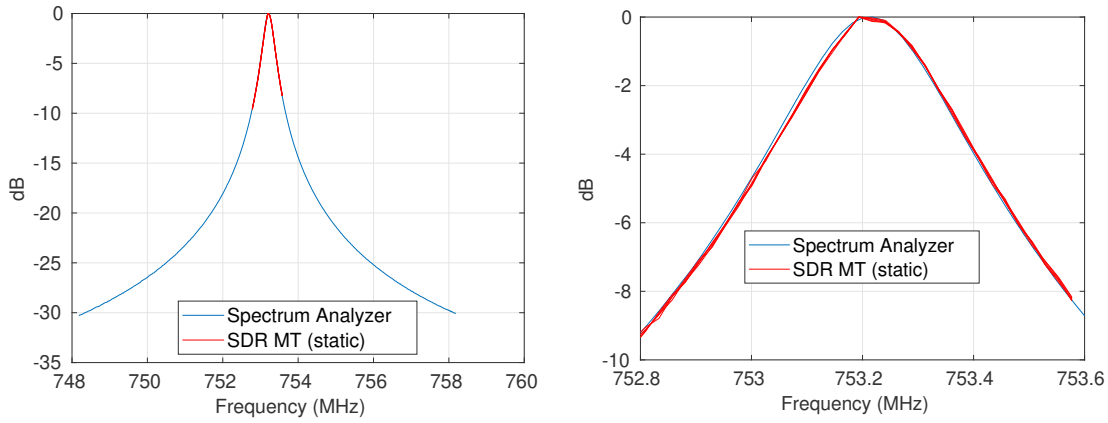

Figure 7-11. Normalized comparison of multitone probing with a spectrum analyzer measurement of the first resonance of Vessel 2. The center resonant frequency of the multitone result has been shifted to coincide with the peak of the spectrum analyzer measurement.

Figure 7-10 compares the multitone measurement with the spectrum analyzer measurement for the unnormalized case. Since some offset in frequency should be expected due to the lower cost crystal references used in the SDR hardware as compared to the instrument grade spectrum analyzer, the 30 kHz offset seen in frequency between the two methods is quite good. Approximately 0.5 dB of offset was seen in amplitude of the two methods in this comparison, which should be acceptable for most SE studies. Figure 7-11 shows the same data normalized with respect to amplitude and resonant center frequency, which shows that the multitone response faithfully captures the shape of the vessel's resonant response. Overall, the results for the five multitone snapshots are nearly identical, indicating that the effective noise level seen in our multitone probing is small. However, approaching the tails of the resonance, a slightly higher effect of noise can be seen, which should be expected due to the lower signal power there.

7.5. Vibration Measurements

Vibration measurements were performed with the multitone setup described in Section 7.3 using the multitone signal specified in Table 7-5. The transmit SDR LO was set at 753.218 MHz, 998.345 MHz, and 1511.629 MHz to probe the TM_{010}, TM_{012}, and TM_{014} cavity resonances, respectively. For each EM resonance, a measurement of the static vessel was performed, as well as measurements under mechanical vibration at 415 Hz and 853 Hz.

The through calibration procedure was used in measurements presented herein, which provides a power transmission coefficient from the transmit (log-periodic) antenna connector to the output connector of the 1-cm field probe in the vessel. The transmit antenna is in the near field of the vessel, and thus computing a traditional SE value requiring plane-wave incidence is not strictly possible. Since we are mainly interested in time variation of coupling into the vessel, we will simply compute and plot the time-varying power transmission coefficient. This quantity is similar to $|S_{21}(f)|^2$, representing a power gain from the transmit antenna input connector to the receive probe output connector, denoted "Transmission" in subsequent plots.

Figure 7-12 shows the calibration weights that were obtained for the three different bands probed and the effect of applying those weights to the mutlitone static vessel measurements. The calibration transmission value represents the transmission gain that would be observed for direct connection of transmit and receive with no additional attenuation. Our calibration uses a 50 dB attenuator, and +50 dB is therefore added to the calibration measurement to account for this. The calibration value includes any analog gain and scaling that is applied to the signal by the SDR hardware, SDR software, and MATLAB post-processing. Since this gain and scaling will be present for both the calibration measurement and the vibration measurements, it is removed by the through calibration procedure. Overall, the SDR hardware and cables present a nearly flat frequency response over these narrow bandwidths. The calibration corrects the overall transmission level, as well as small variation ($< \pm 1$ dB) over the band.

Figure 7-13 shows the resonant response extracted from the multitone measurement for the three different bands. The plots on the left show the frequency samples extracted only from the FFT bins corresponding to tones, which gives a useful, albeit coarse representation of the resonant response. Since we are studying individual resonances that are well separated, the method given in Appendix C can be used to fit the 34 frequency points to a parallel resonant response. Not only does this provide smoothing and interpolation of the signal, but also provides "de-noising" of the response to some extent. The plots on the right in Figure 7-13 show the result of applying resonant fitting and interpolation.

Computation of AM for the static case is shown in Figure 7-14. Ideally with no vibration present, AM should be zero, but numerically AM will be nonzero due to noise, instability of the SDR hardware, etc. Plots on the left in Figure 7-14 show the computation of AM using the raw data at the 34 tone frequency bins, whereas plots on the left show AM computed from the smoothed response. As much as 10% AM levels can be seen at the tails in the raw AM plots, which is reduced to around 2% or less when the resonant-fit data is used. The denoising effect described previously is clearly apparent. Given the advantage of using the resonant-fit data, only this data will be considered hereafter.

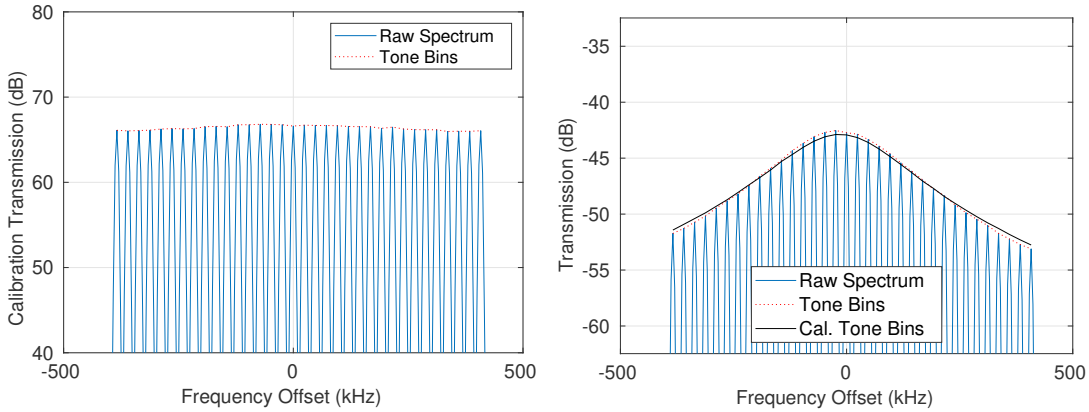

(a) 753 MHz

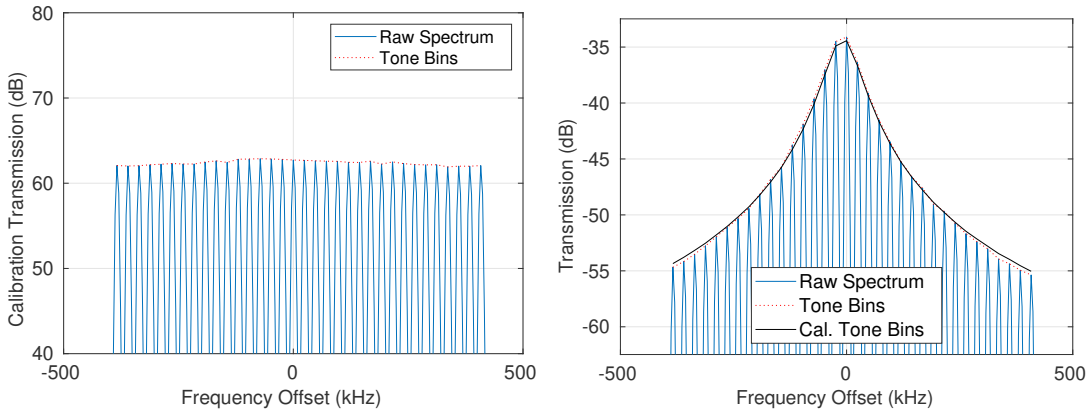

(b) 998 MHz

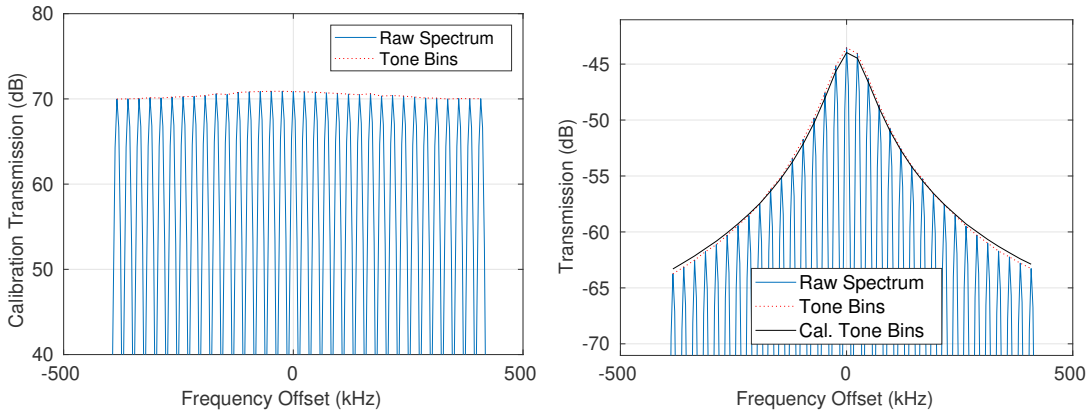

(c) 1512 MHz

Figure 7-12. Effect of calibration applied to vibe measurements. The plots on the left and right show the through calibration measurement, and the effect of applying the calibration to the static resonance measurement, respectively.

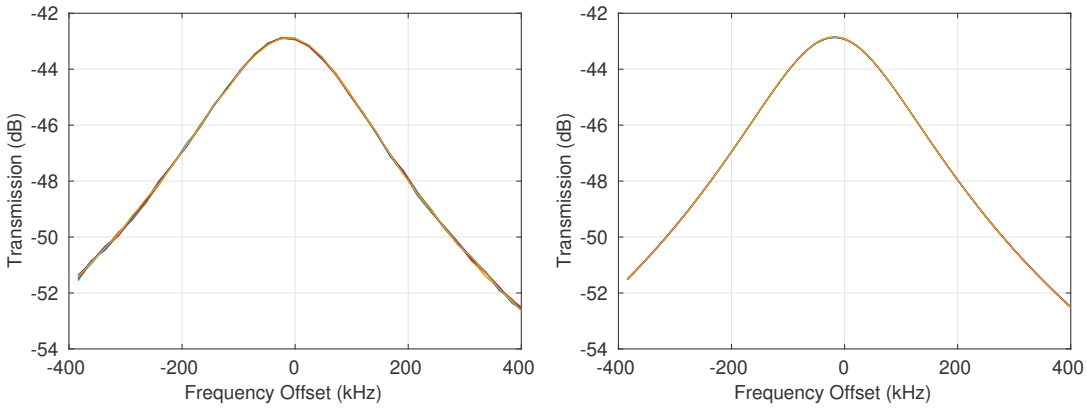

(a) 753 MHz

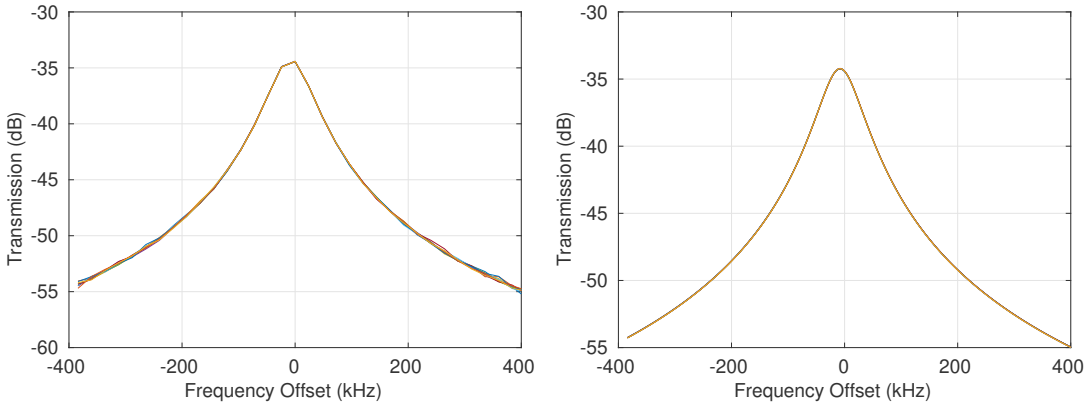

(b) 998 MHz

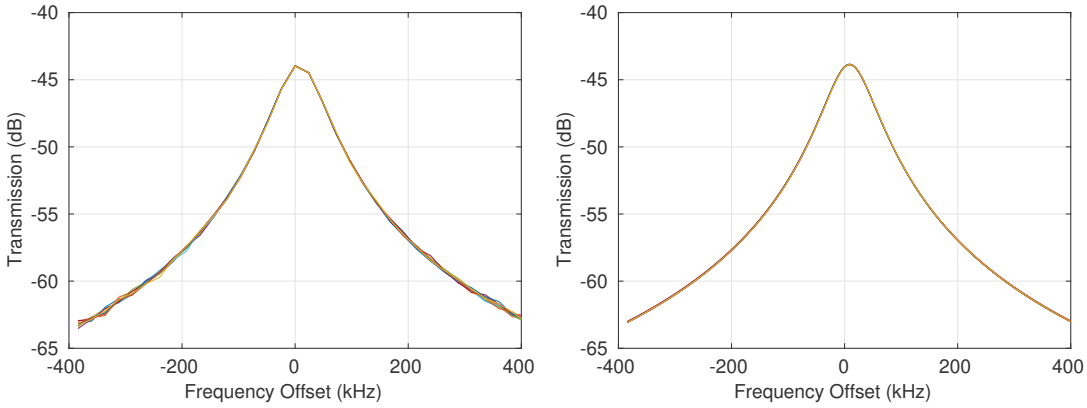

(c) 1512 MHz

Figure 7-13. Transmission response in the static measurement of Vessel 2 for three different EM resonances, where each plot shows 10 consecutive temporal snapshots. Coarse plots on the left show the data extracted from the 34 tones. The smoother plots on the right show the interpolated resonant responses obtained by fitting the data points to a single parallel resonance, and here the multiple plots are visually identical.

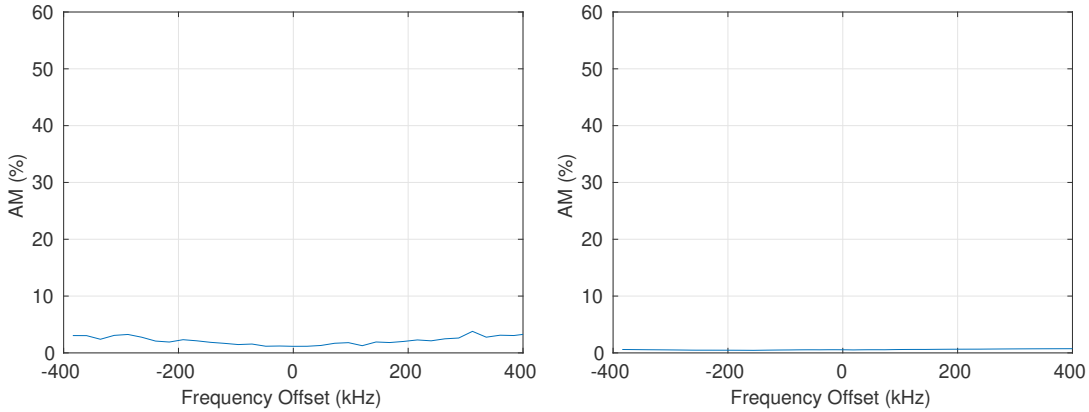

(a) 753 MHz

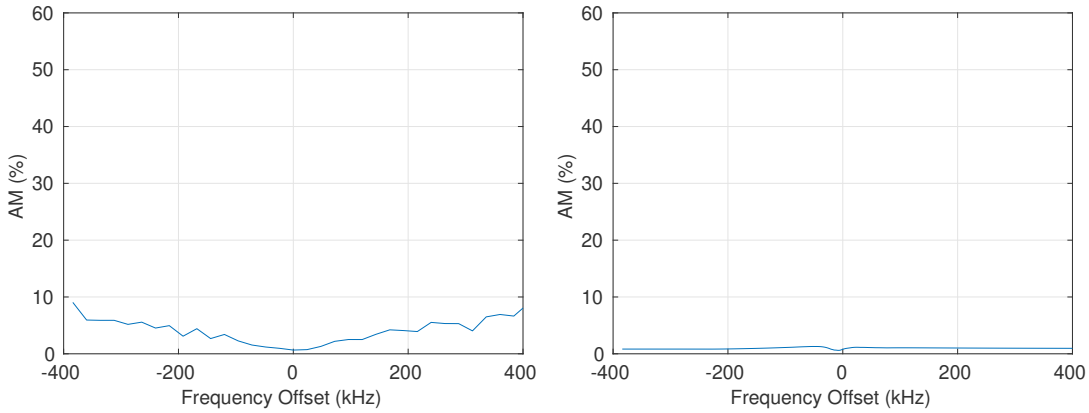

(b) 998 MHz

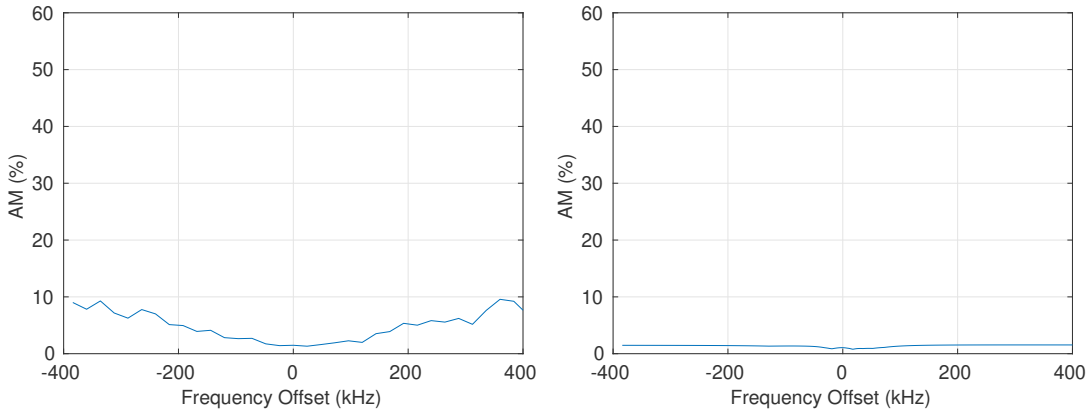

(c) 1512 MHz

Figure 7-14. Amplitude modulation (AM) computed from static measurements, indicating an effective AM noise floor for the present setup. Plots on the left show AM computed from the 34 discrete tones only. Plots on the right show AM computed from the resonant-fit smoothed data. AM was computed here using 50 temporal snapshots.

7.5.1. 415 Hz Vibration

As described previously, the 415 Hz acoustic excitation of the vessel produced strong vibrations on the vessel sides and flange. Figure 7-15 plots a single period worth of snapshots of the resonant response at the three EM resonances for the 415 Hz mechanical vibration. This mechanical resonance primarily produces a shift of the resonant amplitude (E_0) and very little change to the resonant frequency and quality factor, resulting in a very flat AM plot at all resonances. Intuitively, modulation of E_0 would arise due to changes in the contact resistance at contact points along the slot, or the slot opening/closing over time. On the other hand, the presence of vibrations that can be felt along the complete height of the vessel and flange suggests an "ovaling" mode, meaning a deformation of the circular circumference of the vessel. This would tend to not change the pressure present at the flange, and so the connection between ovaling modes and slot modulation requires further investigation.

So far, we have plotted multiple snapshots in time of the power transmission coefficient $|H(f,t)|^2$, but the time *evolution* of this quantity may also be of interest to understand the temporal correlation of the resonance parameters (E_0, ν_0, and Q). To this end, successive time samples of $H(f,t)$ were fit to a single parallel resonance to obtain $E_0(t)$, $\nu_0(t)$, and $Q(t)$. All possible pairs of these parameters are plotted for the 415 Hz mechanical resonance in Figure 7-16. The modulation amplitudes of the three parameters are given in Table 7-3.

Figure 7-16 and Table 7-3 illustrate that for the 415 Hz mechanical vibration, amplitude E_0 variation dominates over the other two parameters, where the peak-to-peak amplitude variation is decreasing with increasing EM resonant frequency. This correlates well with the peak AM that is also decreasing with increasing EM resonant frequency. Interestingly, modulation of ν_0 exhibits a doubled frequency compared to E_0 modulation. The variation of Q is very small and likely negligible from the standpoint of AM.

7.5.2. 853 Hz Vibration

Figure 7-17 plots a single period worth of snapshots of the resonant response at the three EM resonances for the 853 Hz mechanical vibration. Unlike the 415 Hz case, this 853 Hz mechanical resonance mainly produces significant change in the resonant frequency ν_0. Previously it was noted that the 853 Hz acoustic excitation produced the strongest vibrations on the vessel end caps and not on the sides. The presence of vibrations on the vessel end caps suggests a "drum head" mode, where the cylindrical end caps slightly deform outward and inward with time. This would change the volume of the vessel, which would modulate the resonant frequency of TM_{01p}, $p \geq 1$ modes as well. Interestingly, the TM_{010} mode has significant modulation of the resonant frequency, even though this should be independent of the vessel height. Having opposing axial forces on the two halves of the vessel would modulate the pressure present at the flange, possibly modulating the amount of contact resistance present and the size of the slot openings, and these effects could modulate all of the resonant parameters.

Figure 7-18 and Table 7-3 show that the 853 Hz mechanical vibration has a much stronger effect on resonant frequency ν_0 than was present at 415 Hz. The 753 MHz and 1512 MHz EM

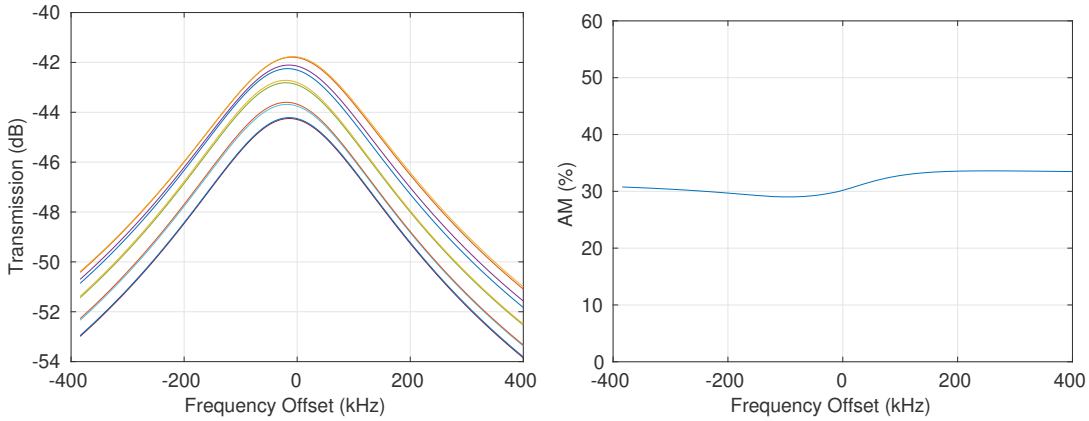

(a) 753 MHz

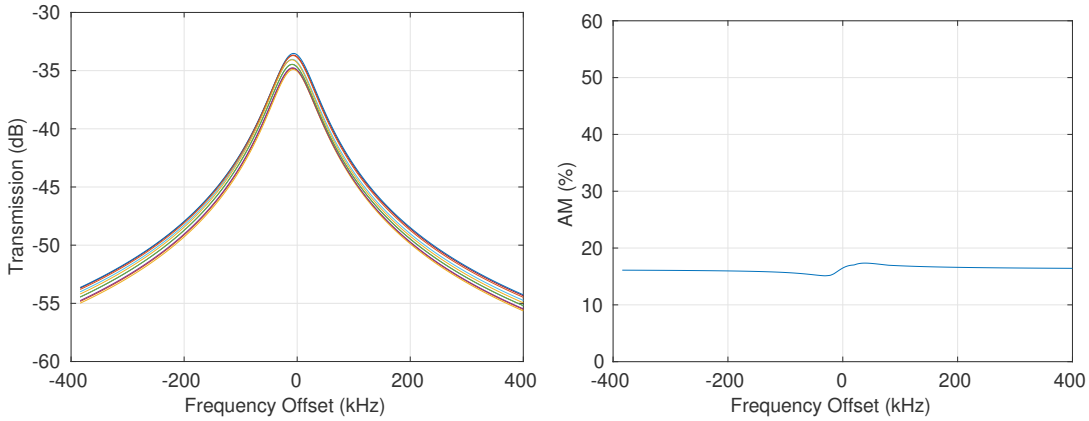

(b) 998 MHz

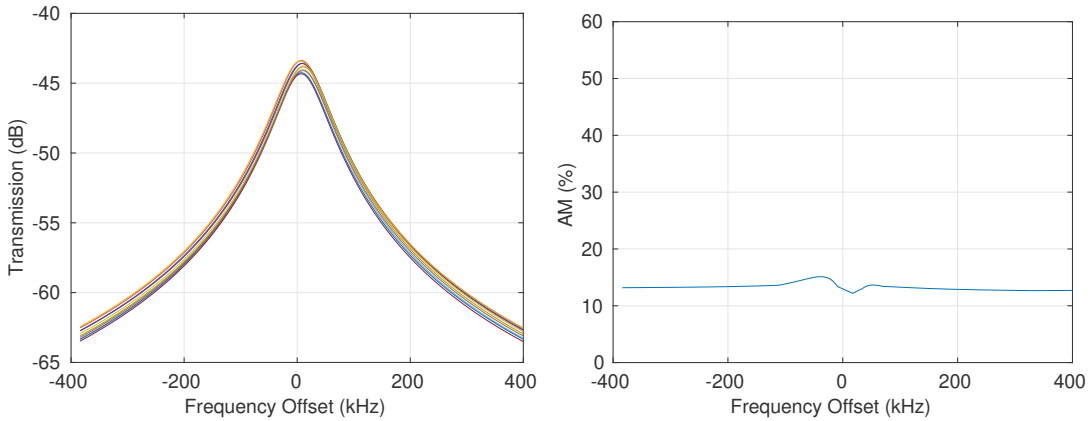

(c) 1512 MHz

Figure 7-15. 415 Hz vibe measurements. Plots on the left show multiple EM response snapshots covering a single period of the mechanical vibration. Plots on the right show AM computed from 50 temporal snapshots.

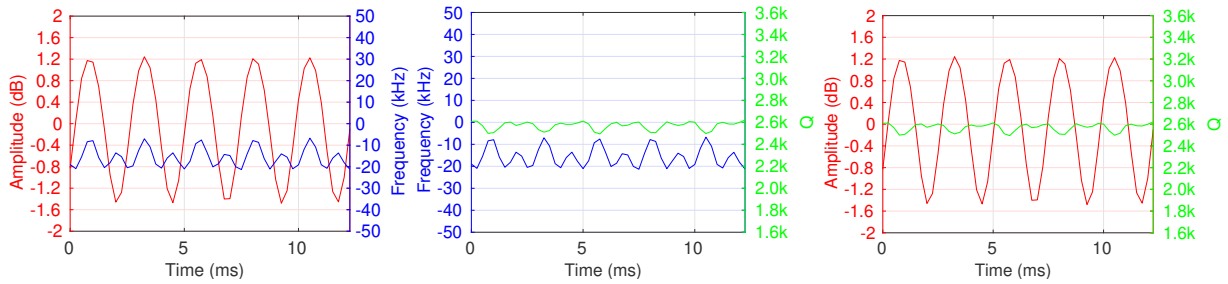

(a) 753 MHz

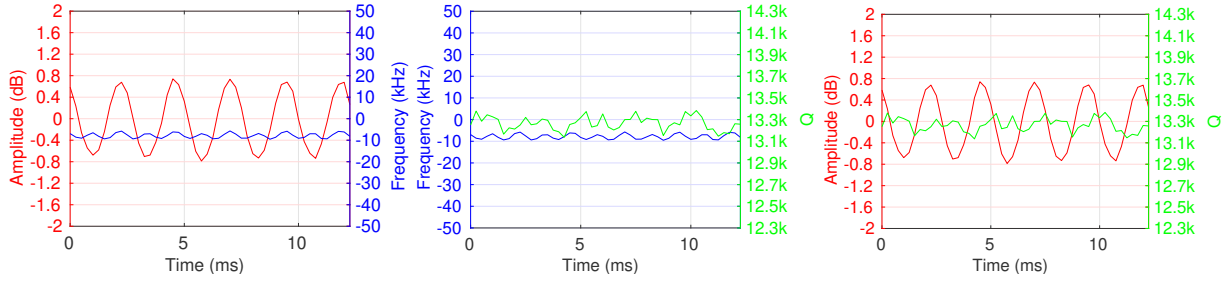

(b) 998 MHz

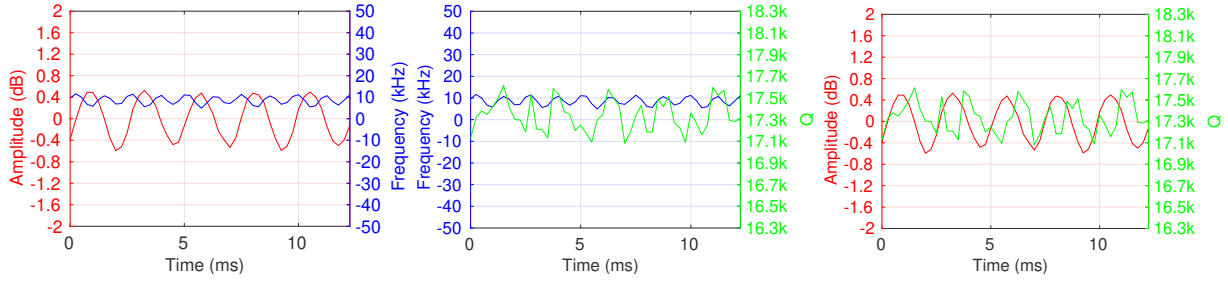

(c) 1512 MHz

Figure 7-16. Time evolution of resonant amplitude (E_0), resonant frequency (ν_0), and quality factor (Q), extracted from successive time snapshots of $H(f,t)$ for the three EM resonances at 415 Hz mechanical vibration.

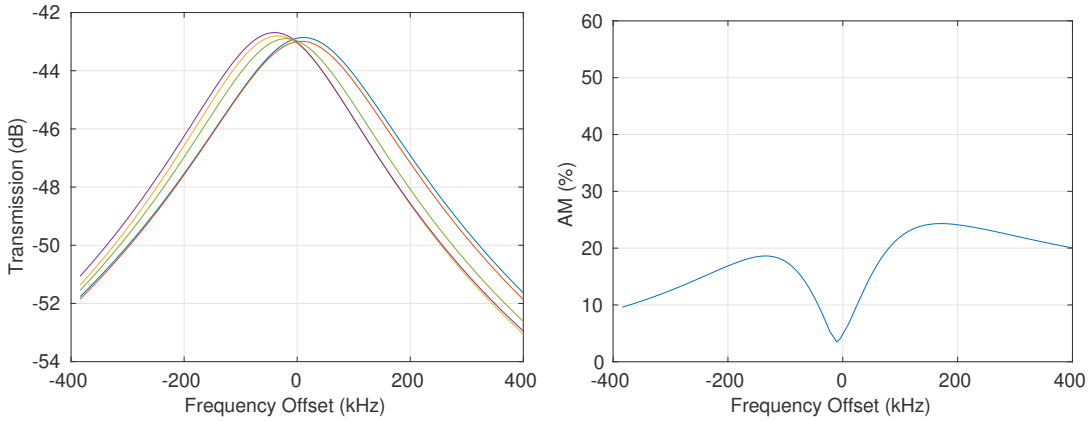

(a) 753 MHz

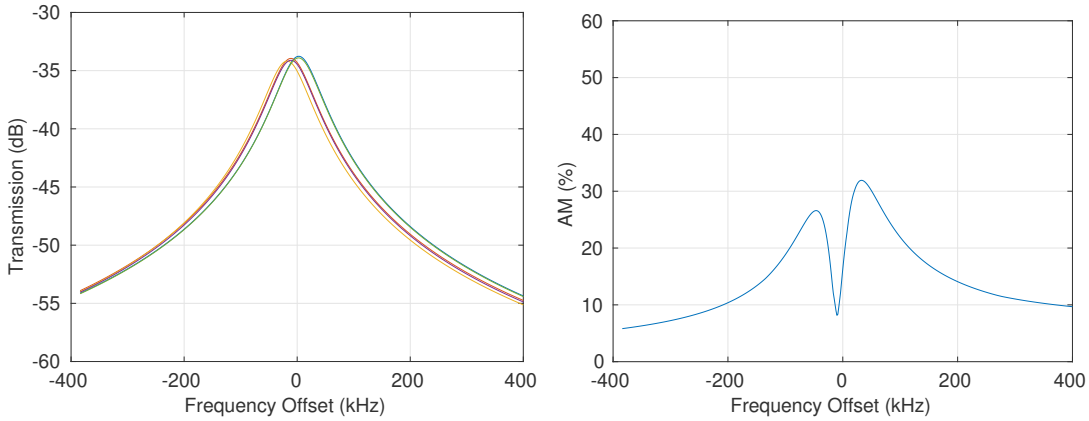

(b) 998 MHz

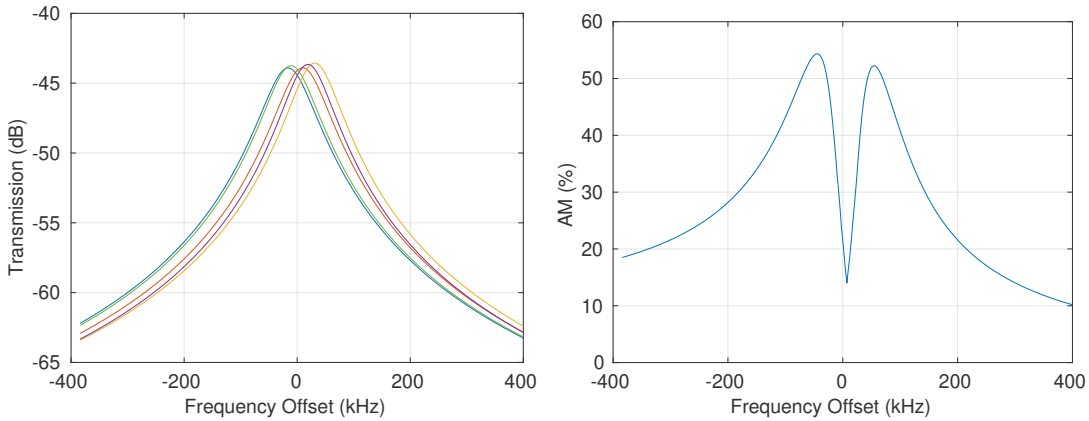

(c) 1512 MHz

Figure 7-17. 853 Hz vibe measurements. Plots on the left show multiple EM response snapshots covering a single period of the mechanical vibration. Plots on the right show AM computed from 50 temporal snapshots.

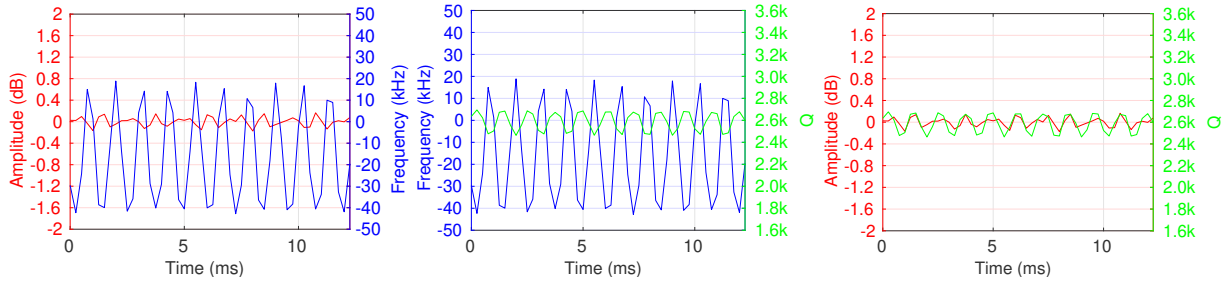

(a) 753 MHz

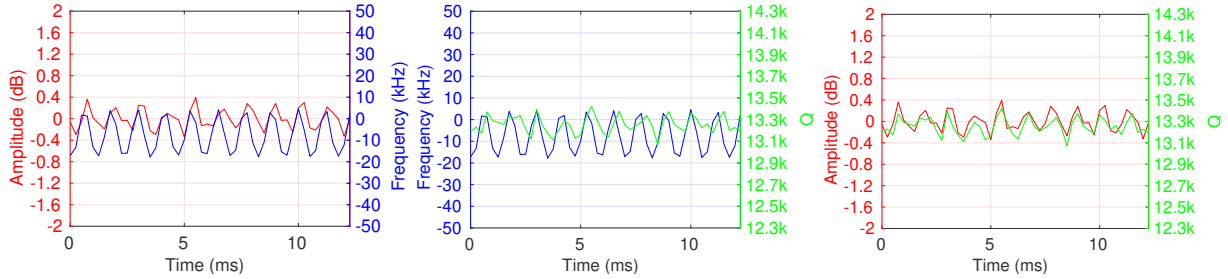

(b) 998 MHz

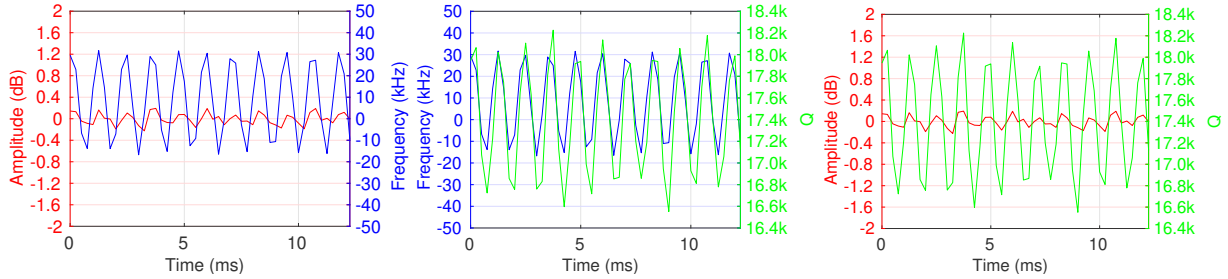

(c) 1512 MHz

Figure 7-18. Time evolution of resonant amplitude (E_0), resonant frequency (ν_0), and quality factor (Q), extracted from successive time snapshots of $H(f,t)$ for the three EM resonances at 853 Hz mechanical vibration.

415 Hz Vibration				
ν_0	ΔE_0	$\Delta\nu_0$	ΔQ	Peak AM
753 MHz (TM_{010})	2.7 dB	14.6 kHz	127 (4.9%)	34%
998 MHz (TM_{012})	1.5 dB	3.8 kHz	247 (1.9%)	17%
1512 MHz (TM_{014})	1.1 dB	6.7 kHz	534 (3.1%)	15%
853 Hz Vibration				
ν_0	ΔE_0	$\Delta\nu_0$	ΔQ	
753 MHz (TM_{010})	0.3 dB	61.7 kHz	232 (9.0%)	24%
998 MHz (TM_{012})	0.7 dB	22.4 kHz	351 (2.6%)	32%
1512 MHz (TM_{014})	0.4 dB	48.5 kHz	1675 (9.6%)	54%

Table 7-3. Peak-to-peak modulation of resonant amplitude E_0, resonant frequency ν_0, and quality factor Q for measurements at 415 Hz and 853 Hz mechanical vibration.

resonances have small amplitude variation, and high frequency/Q variation, whereas the 998 MHz resonance exhibits a moderate amplitude variation and moderate frequency/Q variation. Overall, peak AM is increasing with increasing EM resonant frequency, which is consistent with a drum-head mechanical mode that slightly elongates the vessel. In this case, higher axial mode orders would be more sensitive to the same displacement as compared to lower orders, leading to higher modulation of the resonant frequency and higher AM. It is interesting to also consider the correlation of changes in the resonant parameters for 853 Hz. Figure 7-18 shows that usually E_0, ν_0, and Q are in phase or have positive correlation. The exception occurs for the 753 MHz EM resonance, where ν_0 is 180° out-of-phase with the Q and amplitude.

7.6. Conclusion

This chapter has demonstrated a multitone probing method that allows the resonant response of vessels with slots to be tracked with high temporal resolution. The technique provides more information on how vessel deformation evolves during mechanical vibration than can be obtained with a traditional AM measurement. It is expected that the multitone probing technique could be combined with the near-field scanning concept presented earlier, allowing the time variation of slot coupling to be mapped spatially along slots. This knowledge could then be used to extract information about time-varying contact and associated resistance along slots, allowing detailed models of vessels that are subject to mechanical vibration to be developed.

8. CONCLUSIONS AND FUTURE WORK

This chapter summarizes this LDRD project, provides ideas on future extensions of this research, and highlights the expected impact of this work.

8.1. Project Summary

This report has described the results of an LDRD project whose aim was to develop methods for characterizing slot properties that cannot be obtained from CAD specifications, yet are critical for correctly simulating the shielding effectiveness of enclosures with joints. The report has focused on the application to weapon system cavities, which typically consist of multiple cylindrical or conical cavities connected at "joints." Several joint types, e.g. flanges, lap joints, and threaded joints, are possible, and may require a different approach for characterization and modeling. However, a common element of joints is the need to understand where contact occurs (contact points) and the electrical properties of the contacts (such as contact resistance).

The main effort in this project was to consider simple joints where the contact points and slot properties are as controlled as possible. Vessel 2 was created with this goal in mind, consisting of two top-hat like structures that connect at a simple bolted flange. Metal shims at the bolt positions ensure that contact occurs only at the bolts/shims and that the slot areas between bolts have a known slot length and a nearly constant slot width. The main unknown to be characterized in this case is the contact resistance that occurs at the bolt positions, and developing a method for measuring this resistance was the subject of Chapters 2-5.

The effort to develop a method for characterizing the bolt/shim contact resistance of Vessel 2 began with the conceptually simple idea of embedding coaxial probes in the flange, allowing slot voltages to be measured directly. Simulations in Chapter 2 demonstrated that embedded probes must be sensitive to changes in the signal on the order of tenths of a dB to provide useful estimates of contact resistance. Unfortunately, experiements in Chapter 3 revealed that mechanical placement of embedded probes leads to variation of probe response on the order of several dB, making it virtually impossible to measure the small variation necessary to estimate contact resistance at the bolts.

Chapter 4 developed a different method that indirectly measures slot voltages by scanning fields that are outside of (but in close proximity to) the slots. An electric field probe placed 5 mm away from the slot is able to collect information about slot fields continuously along the slot and around contact positions. Simulations in Chapter 2 showed that the variation in the near fields at 5 mm spacing can be on the order of 10s of dB near the bolt contact points, allowing a sensitive characterization of contact resistance to be obtained.

Experiments in Chapter 5 demonstrated the ability to extract useful estimates of the bolt/shim contact resistance of Vessel 2 for the controlled case (with shims). Given its rotational symmetry, near fields of Vessel 2 could be probed all around the circumference at a constant separation distance using a simple single probe arrangement with a rotation stage. Comparison of the measured near-field variation with simulations from Chapter 2 allowed the effective DC contact resistance at the shims to be estimated. Further, the usefulness of extracted contact resistance was demonstrated by showing good agreement between SE measurements and simulations incorporating the extracted contact resistance.

Important progress has been made on the problem of characterizing joints and improving SE predictions of enclosures in this LDRD project. However, these advances should be considered a first step, since the main vessel under consideration (Vessel 2) has a very simple controlled joint, and realistic joints are likely to have much more complicated behavior. For this reason Chapter 5 also explored the uncontrolled joint case, where the shims were removed and near fields were measured for various bolt torques. A much more complicated near-field structure was observed, consistent with a slot having many random contact points. Although it was not yet possible to extract contact points and associated contact resistance with certainty for this uncontrolled joint, it was demonstrated that multi-contact 1D and 2D circuit models of the slot were able to duplicate the measured behavior. Chapter 6 studied a lap joint vessel, that also does not control contact points of the slots. The scanned near-field pattern had a complexity similar to, but somewhat simpler than, Vessel 2 without shims, a result that was somewhat surprising given the more complicated "tortuous" nature of the slot.

In response to feedback from an LDRD review, Chapter 7 developed a method for scanning slot response with high *temporal* resolution. Combined with the previous spatial scanning techniques developed in this project, having the additional temporal dimension can potentially allow accurate spatial and temporal characterization of slots under vibration. Unlike traditional swept CW measurements performed with a VNA or spectrum analyzer, a multitone signaling approach was adopted, allowing the vessel's frequency response to be measured rapidly and at all frequencies simultaneously. The specific signal used in this work allowed 34 frequencies covering an 800 kHz band to be probed in 250 μs, providing better-than-Nyquist temporal sampling of two acoustic resonances. Observation of the time evolution of the resonant behavior under vibration is therefore possible, providing a wealth of information to understand the dynamics of vessels and slots in the presence of mechanical vibration.

8.2. Future Work

As described above, the main objective that was completed in this work is characterization of contact resistance for the controlled case of Vessel 2 with shims. Although an important step, much more work is needed to understand practical joints whose properties are more random in nature. Section 5.3 demonstrated that a flanged joint without shims can present a very complex near-field response, suggesting many random contact points, whose contact resistance would need to be extracted to provide a complete model. Although it was demonstrated that 1D and 2D slot

models can duplicate the behavior of the observed near fields, it is doubtful that models fitted this way accurately represent true contact patterns.

To allow the near-field scanning concept to be useful for uncontrolled joints, it is expected that more information needs to be extracted from scans. For example, since a contact point would create a point of axial current flow (at least for a flanged joint), it is expected that a magnetic field probe could provide a more direct indication of contact than an electric field probe. To this end, a small differential loop probe could be used to augment electric field scans. Likewise, more than a single component of the electric and/or magnetic field could be scanned, providing a more comprehensive picture of fields near the slot, thus reducing the ambiguity of the inversion procedure required to estimate contacts from fields. In the case that contacts exhibit frequency-independent behavior (at least within some range of frequencies), data for multiple vessel resonances could be used together to reduce model ambiguity. From the theoretical side, slot models combined with observability considerations could determine how much information is actually needed to extract unambiguous contact information from a near-field scan. This work could also consider more advanced inversion techniques to extract contact positions and contact electrical properties, rather than relying on the current brute-force GA-based fitting.

The embedded probe idea was abandoned in favor of near-field scanning due to the sensitivity of embedded probes to mechanical placement. However, it is possible that the behavior of some complex slots, like those with threaded connections or tortuous paths, may not be completely observable from the vessel exterior. This raises the question of whether some type of embedded probe may still be necessary to characterize complex slots. Perhaps a more advanced RF probe could be developed that does not suffer from the same sensitivity issues as a simple passive coaxial probe. For example, an active probe could possibly be developed that is sensitive to fields in a much smaller area, reducing sensitivity to vertical placement. A MEMS type sensor might be possible to fabricate, where field strength changes the force on small mechanical components, modulating electrical resistance or capacitance. Another probing technique that was briefly explored (but not reported on herein) is the possibility of developing electro-optical (EO) probes that could be placed directly on a slot aperture. Advantages of EO probes are the very wide bandwidth and the low disturbance to slot fields, since the probe materials are mostly non-conductive dielectrics. If an EO probe could be created on a thin film, it is conceivable that the probe could be sandwiched directly in the slot, similar to what is done with thin-film pressure sensors.

Combination of near-field scanning with multitone signaling appears to be a natural fit, but was not explored in this work. It is of high interest to scan slots under vibration both temporally and spatially to see the effect of mechanical modulation all along the slot. This could answer important questions: Are points of contact changing under vibration, or are contact points fixed and only the contact resistance of those points is changing? Is it mainly the resonant cavity or the slot that is changing in response to the vibration?

One important issue with spatio-temporal scanning is correlating the temporal responses at different spatial positions. One possibility is to use multiple probes to simultaneously obtain the temporal response at multiple spatial positions. One drawback of multiple probes is that only a few discrete spatial points are obtained. Additionally, a much more complex measurement system is required, due to the need to calibrate multiple probes and to have many receive ports. For

repetitive vibration waveforms, such as sinusoids, it is likely that multiple probes are not necessary, as long as the RF receive waveform can be synchronized with the audio vibration waveform. This synchronization could either be done during the measurement by aligning acquisition times and clocks in the audio vibration and EM domains, or it could be performed in post-processing if the acquisition hardware can sample both RF and audio signals simultaneously.

One drawback of the multitone signaling concept is the need for highly linear transmit hardware (power amplification) and the relatively low SNR per frequency per tone. It would be of interest to investigate extensions to CW probing that allow the response at multiple frequencies to be correlated. For example, for repetitive vibration waveforms, it may be possible to synchronize the RF acquisition with the audio vibration waveform to allow time-evolution of CW response at multiple frequencies to be properly synchronized. This would allow swept CW measurements to provide the same information as multitone signaling, yet with high SNR and low PA linearity requirements.

Investigations in these mentioned directions would likely allow slot characterization to reach a mature level, where even complex joints can be directly characterized. Models for both static slots and those subject to vibration could then be conveniently measured and captured into detailed models.

8.3. Project Impact

The central concrete result of this project is described in Section 5.2.5, where it was demonstrated that a good fit in SE predictions can be obtained by incorporating contact resistance estimated from near-field scans. Using this technique, error between measured and predicted SE was approximately 1 dB, which is comparable to the uncertainty of the measurement setup. The impact of this observation is that the current trial-and-error procedure of fitting the SE of models and measurements can be greatly reduced by incorporating near-field scanning and more direct characterization of joint properties. It is expected that these techniques could be adopted as part of future weapon characterization efforts to reduce model uncertainty and improve simulation predictions.

Demonstration of the multitone signaling concept for fast probing of EM coupling in cavities has not been considered previously, and is a secondary impact of this work. This technique has the potential to allow slots and cavities under vibration to be understood at a fundamental level, where the true time-evolution of resonant response can be observed. Although a method was suggested in Section 8.2 that could allow CW methods to provide the same information as multitone probing for repetitive waveforms, multitone probing still has the advantage of allowing temporal response to be probed for arbitrary (non-repetitive) signals.

Another potential impact of this project is to change current thinking on how EM characterization of weapon enclosures should be performed. In addition to characterizing the SE of a complete enclosure using far-field illumination, near-field scanning techniques allow individual parts of the system (such as slots/POEs) to be characterized separately. These measurements could allow

weak spots of the system to be identified directly through measurement, rather than requiring many measurement-simulation iterations to be performed to reveal the source of design shortcomings. Additionally, reciprocity considerations used in this work (see Appendix E) demonstrate that there are multiple ways to perform an SE measurement, and that a reciprocal configuration may provide for a more convenient measurement or reduce the number of simulations required.

APPENDIX A. Vessel Designs

This appendix provides specifications of the two vessels that were used in this work.

A.1. Vessel 2

Vessel 2 consists of two top-hat like aluminum structures that are bolted together at the 0°, 90°, 180°, and 270° positions around the flange, as depicted in Figure A-1. The wall thickness of the vessel is 0.25 inches. The width of the slots can be controlled by placing thin metal shims at the bolt locations, and in this work 5-mil shims were used when a controlled slot width was desired. The flange is 0.25 inches thick and extends 0.75 inches from the vessel surface, giving the slots a depth of 1 inch. The interior of the vessel is a cylindrical cavity with height and radius equal to 18 and 6 inches, respectively.

A detailed drawing of Vessel 2 is shown in Figure A-2.

A.2. Lap Joint Vessel

Limited analysis was performed of the Lap Joint Vessel, as shown in Figure A-3, which is similar to Vessel 2, but provides a more complex joint. When the two halves of the Lap Joint Vessel are bolted together, the joint forms a slot that follows a “tortuous path” from the outside to the inside, as shown in Figure A-1(b). As with Vessel 2, the interior of the Lap Joint Vessel is a cylindrical cavity with height and radius equal to 18 and 6 inches, respectively. Note that the two halves of the Lap Joint Vessel are different, which are shown in Figures A-4 and A-5, showing the top and bottom halves, respectively.

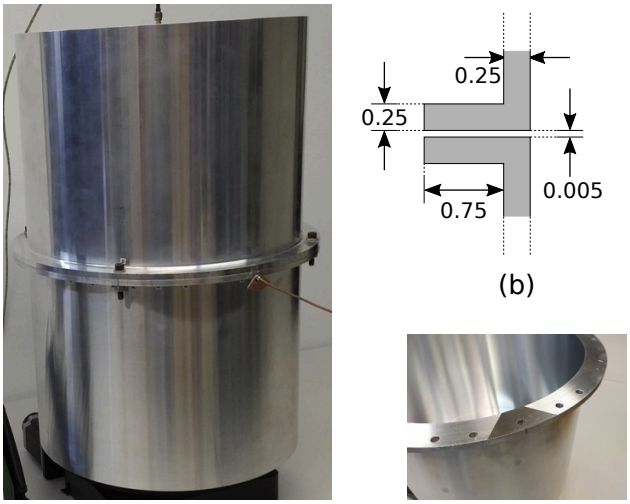

Figure A-1. Vessel 2 that was used in this work: (a) photo, (b) flange cross-section, and (c) shim spacer. Note that units in (b) are inches. When shims are used the width of the slot is 0.005 inch. When no shims are present, the slot width is much smaller, possibly 0.001 inch or less.

Figure A-2. Mechanical drawing of Vessel 2. Note that the full vessel is made from two identical halves.

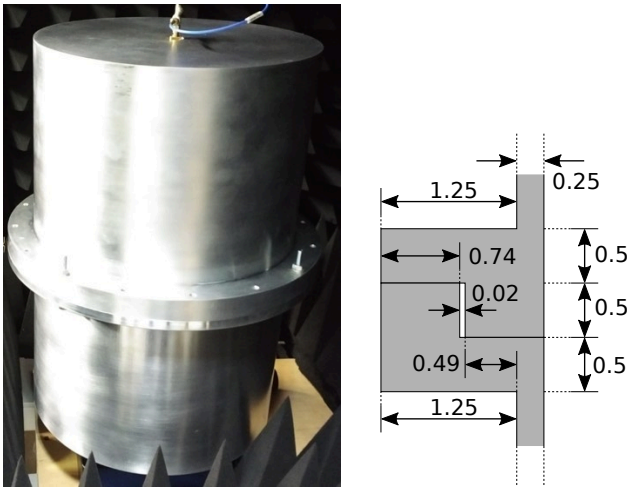

Figure A-3. Lap Joint Vessel that was used in this work: (a) photo, and (b) flange cross-section exhibiting a tortuous path. Note that units in (b) are inches.

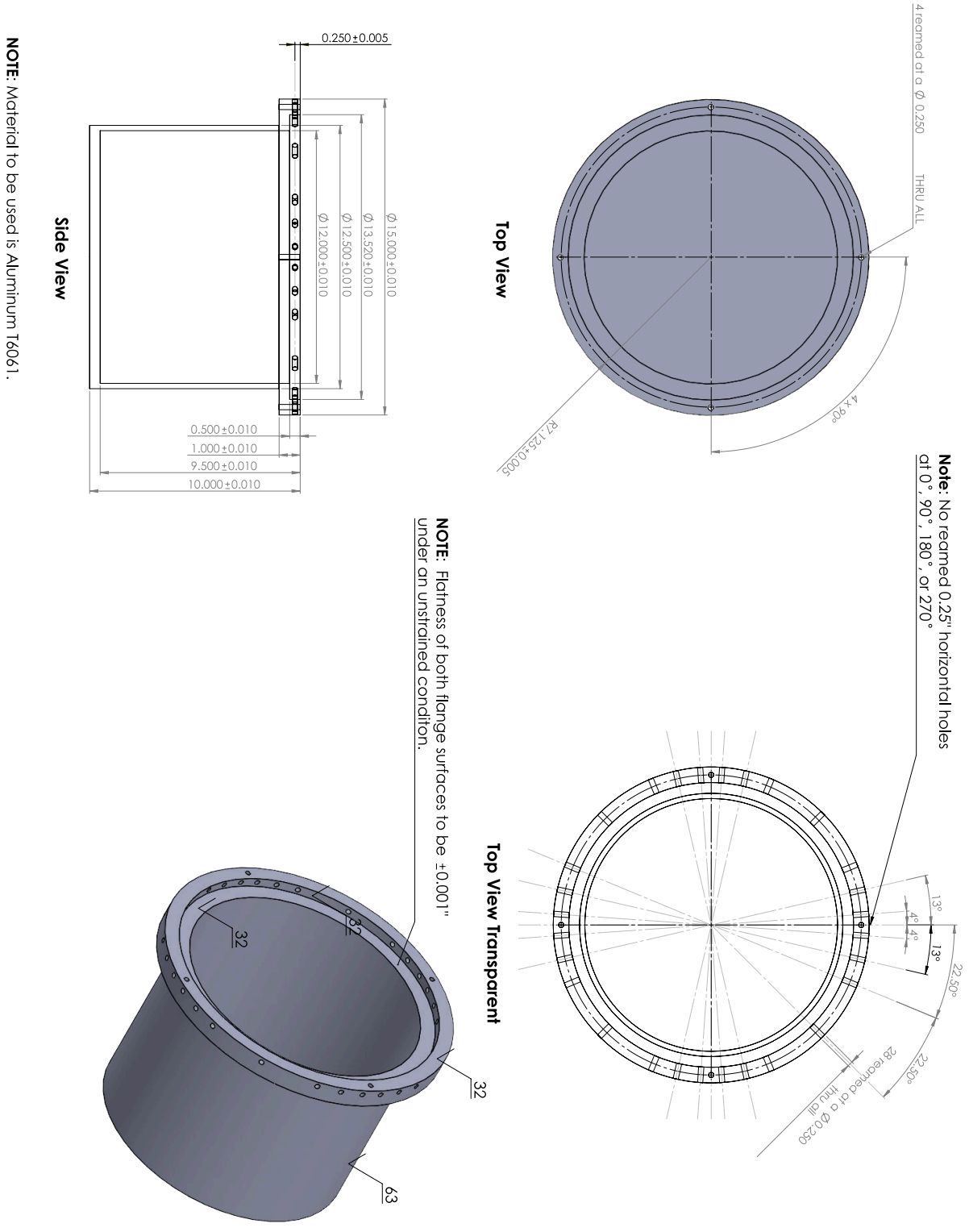

Figure A-4. Mechanical drawing of the top half of the Lap Joint Vessel.

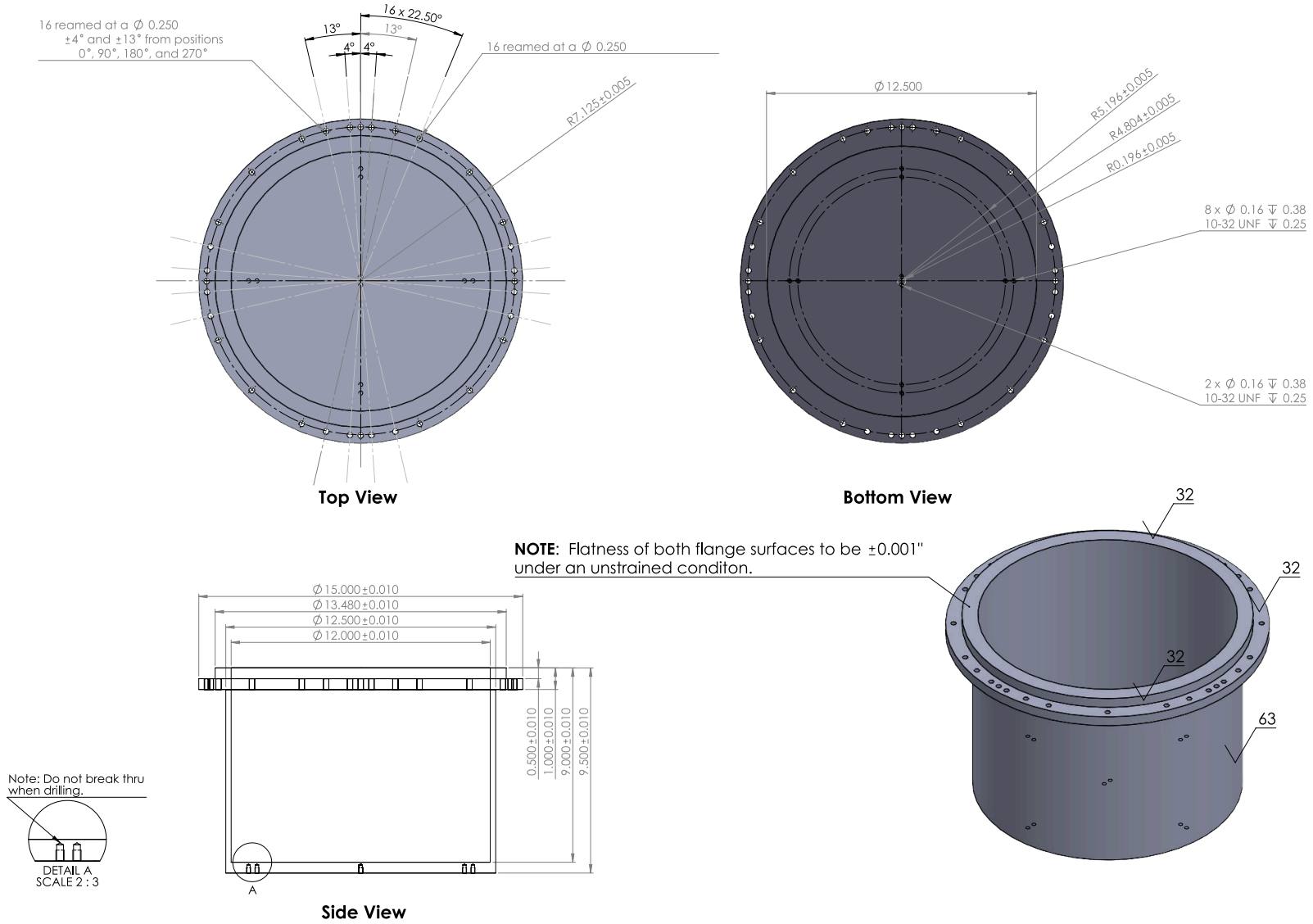

NOTE: Material to be used is Aluminum T6061.

Figure A-5. Mechanical drawing of the bottom half of the Lap Joint Vessel.

APPENDIX B. Cylindrical Cavity Modes

For completeness, this appendix summarizes resonant frequencies and field profiles for transverse magnetic (TM) modes for the cylindrical cavities encountered in this work. Figure B-1 shows the axes and dimensions of the cylinder considered herein.

B.1. Resonant Frequencies

We consider the TM_{nmp} mode, where the indices are

$n = 0, 1, \ldots$ Tangential mode index (variation in ϕ).
$m = 1, 2, \ldots$ Radial mode index (variation in ρ).
$p = 0, 1, \ldots$ Axial mode index (variation in z).

The resonant frequency of the TM_{nmp} mode is given by

$$f_{nmp} = \frac{c}{2\pi}\sqrt{\left(\frac{\xi_{nm}}{a}\right)^2 + \left(\frac{p\pi}{h}\right)^2}, \tag{B.1}$$

where c is the speed of light in the fill medium (for air $c = 2.99703 \times 10^8$ m/s), a is the vessel radius, h is the height of the vessel, and ξ_{nm} is the mth zero of the nth order Bessel function, i.e., the mth root that solves

$$J_n(\xi_{nm}) = 0. \tag{B.2}$$

Note that published tables of Bessel function zeros often show 4 to 5 decimal places, which may be insufficient to provide sub-MHz accuracy of cavity resonances. A MATLAB function that finds more accurate values was written and used to generate Table B-1 that gives Bessel function zeros to 12 decimal places.

n \ m	1	2	3	4
0	2.404825557696	5.520078110286	8.653727912911	11.791534439014
1	3.831705970208	7.015586669816	10.173468135063	13.323691936314
2	5.135622301841	8.417244140400	11.619841172149	14.795951782351
3	6.380161895924	9.761023129982	13.015200721698	16.223466160319
4	7.588342434504	11.064709488501	14.372536671618	17.615966049805

Table B-1. Bessel function zeros ξ_{nm}, where n is the Bessel function order and m is the root number.

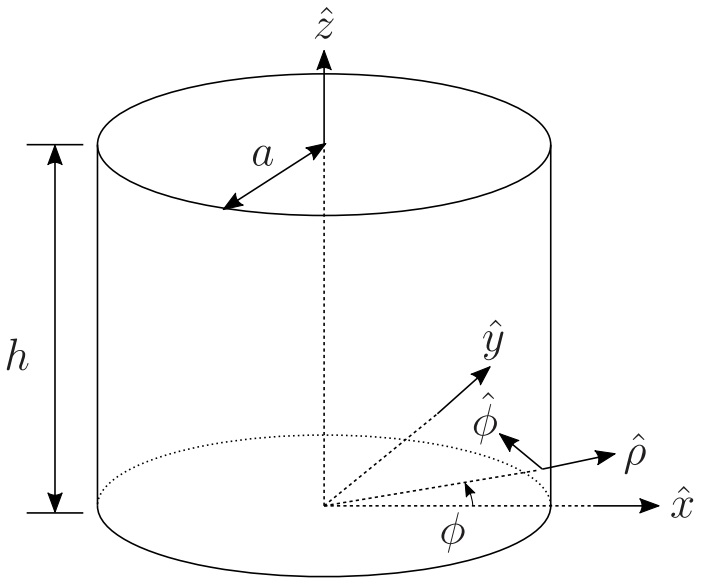

Figure B-1. Cylindrical coordinate system and dimensions used to define TM modes.

B.2. Modal Fields

The modal fields for the TM_{nmp} mode are given by

$$E_z = J_n(k_\rho \rho)\cos(n\phi)\cos(k_z z), \tag{B.3}$$

$$E_\rho = -\frac{k_z}{k_\rho} J_n'(k_\rho \rho)\cos(n\phi)\sin(k_z z), \tag{B.4}$$

$$E_\phi = \frac{k_z}{k_\rho^2}\frac{n}{\rho} J_n(k_\rho \rho)\sin(n\phi)\sin(k_z z), \tag{B.5}$$

$$H_\rho = -\frac{jk}{\eta k_\rho^2}\frac{n}{\rho} J_n(k_\rho \rho)\sin(n\phi)\cos(k_z z), \tag{B.6}$$

$$H_\phi = -\frac{jk}{\eta k_\rho} J_n'(k_\rho \rho)\cos(n\phi)\cos(k_z z), \tag{B.7}$$

$$H_z = 0, \tag{B.8}$$

where

$$k_\rho = \frac{\xi_{nm}}{a}, \tag{B.9}$$

$$k_z = \frac{p\pi}{h}, \tag{B.10}$$

$$k^2 = k_\rho^2 + k_z^2 = \frac{2\pi f_{nmp}}{c}, \tag{B.11}$$

and $\eta = \sqrt{\mu/\varepsilon}$. Note that the choice of $E_z \propto \cos(n\phi)$ in the expressions above arbitrarily places the peak of E_z at $\phi = 0$. In practice, the position of the modal peak can be at any angle, depending on how the mode is excited.

APPENDIX C. Resonant Response Fitting

This appendix provides a simple method for fitting the resonant response of cavities to a parallel RLC resonance. The method is appropriate in the case of discrete modes that do not appreciably overlap, since only a single resonant peak is being modeled. One advantage of this method over rational interpolation fitting is that no phase information is needed. The development here uses results from Chapter 6 of [7].

C.1. Parallel RLC Response

In terms of circuit component values, the parallel RLC input impedance may be written as

$$Z_{\text{in}} = \left(\frac{1}{R} + \frac{1}{j\omega L} + j\omega C \right)^{-1}, \tag{C.1}$$

where $\omega = 2\pi f$ is the circular excitation frequency. Power quantities are proportional to $|Z_{\text{in}}|^2$, which can be written as

$$P(f) = |Z_{\text{in}}|^2 = \frac{R^2}{1 + R^2 \left(\omega C - \frac{1}{\omega L} \right)^2}. \tag{C.2}$$

The resonant frequency and quality factor of the parallel RLC resonance can be found as

$$\omega_0 = \frac{1}{\sqrt{LC}}, \tag{C.3}$$

and

$$Q = \omega_0 RC, \tag{C.4}$$

respectively. This allows (C.2) to be written compactly as

$$P(f, Q, f_0, E_0) = \frac{E_0^2}{1 + Q^2 \Delta^2}, \tag{C.5}$$

with

$$\Delta = \frac{f}{f_0} - \frac{f_0}{f}, \tag{C.6}$$

where f and f_0 are the excitation frequency and resonant frequency, respectively, and $E_0^2 = R^2$ is the response power at the resonant peak. This final form of $P(f)$ is used in this work for fitting cavity resonances to find Q, f_0, and E_0, as well as to allow for convenient interpolation.

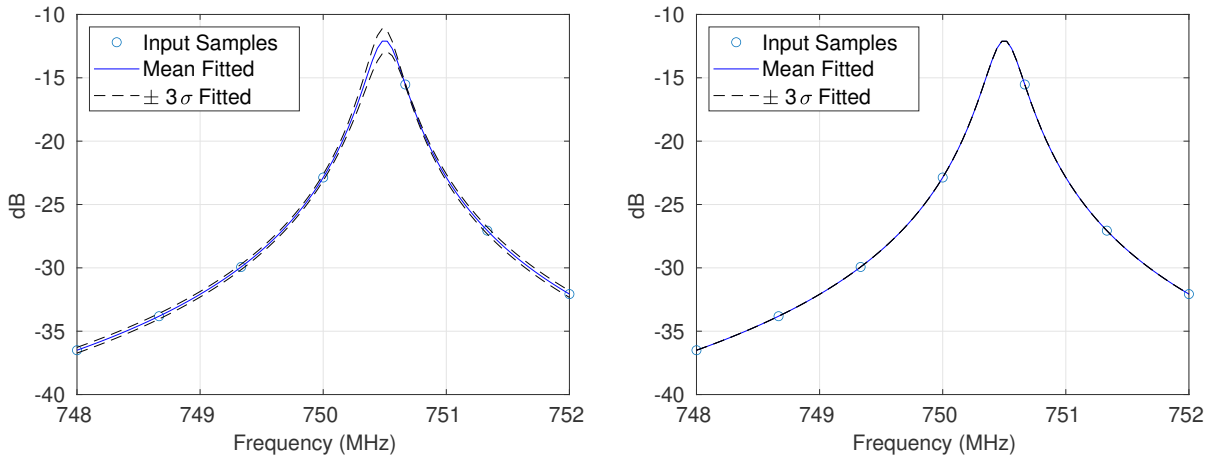

(a) SNR = 30 dB **(b) SNR = 100 dB**

Figure C-1. Example of the parallel RLC fitting method applied to an ideal generated response with $Q = 2500$, $f_0 = 750.5$ MHz, and $E_0 = 0.25$. Dashed curves show the envelope of the fitted response three standard deviations above and below mean fitted response.

C.2. Fitting Method

Resonant peak fitting is performed in MATLAB using the objective

$$\{Q, f_0, E_0\} = \arg \min_{Q, f_0, E_0} \sum_{\ell=1}^{N_F} \left[10 \log_{10} P_{\text{sample}}(f_\ell) - 10 \log_{10} P(f_\ell, Q, f_0, E_0) \right], \tag{C.7}$$

where N_F is the number of frequency points to fit, and $P_{\text{sample}}(f)$ is a measured or simulated response to be fitted. This work uses MATLAB's fminsearch() function to solve (C.7), which uses the Nelder-Mead algorithm. The initial guess for the search is found by taking the peak of $P_{\text{sample}}(f)$ for f_0 and E_0. The initial guess for Q is found by performing a simple linear interpolation of the input response and computing the Q based on the bandwidth 3 dB down from the peak.

Note that the objective in (C.7) fits the power response in dB as opposed to linear power. Given the large dynamic range of the power of samples around a resonant peak, fitting on a dB scale provides equal weight to all sample points, usually providing a better fit. However, care is required to ensure that sample points with very poor quality far from the resonant peak are not included when performing such fits.

Figure C-1(a) shows an example of applying the resonant fit to the case of a resonant peak with $Q = 2500$ centered at 750.5 MHz and sampled at 7 points from 748 MHz to 752 MHz. Statistics of the fit were found by running the fitting for 1000 random realizations and assuming 30 dB worst case SNR (relative to the lowest power tail sample). The plot shows the mean fitted response, as well as the fitted response three standard deviations above and below the mean fit. Note that fitted response curves were converted to dB *before* computing the mean response and error standard deviation. Figure C-1(b) shows the case for an assumed SNR of 100 dB (basically noiseless), showing that a near perfect fit is obtained.

Parameter	Actual	Fitted	
		Mean	Standard Deviation
Q	2500.0	2505.9	108.0
f_0	750.5000 MHz	750.5000 MHz	0.004 MHz
E_0	-12.04 dB	-12.03 dB	0.31 dB

Table C-1. Error in extracted resonance parameters for the resonant-fit example, where 30 dB worst-case SNR is assumed.

Table C-1 shows error of the extracted resonant parameters (Q, f_0, and E_0) for the case of 30 dB SNR. The results show that the fitting method is nearly unbiased, providing good estimates of the resonant parameters. The result also shows that Q is more sensitive to fitting error than center frequency (f_0) and peak amplitude (E_0). The result suggests that for a Q of 2500, we should not expect fits to Q factor that are better than about ± 100.

APPENDIX D. Slot Modeling

This appendix describes the reduced order slot models that were used in this work. Specifically, one-dimensional (1D) and two-dimensional (2D) models are developed in Sections D.1 and D.2, which are based on finite-difference transmission line representations. For this work, it is also important to understand how slot fields propagate outward to probe locations, which is treated by the Green's function derivation in Section D.4

We note that the circuit-based models are fundamentally related to power balance models for cavities that have been treated previously [2]. The major difference is that the goal in this present work is to use a numerical approach to allow the models to be as general as possible, avoiding analytical assumptions or requirements on the shape of slots and/or vessels.

D.1. One-Dimensional Slot Model

Figure D-1 depicts the 1D slot model that was used. The slot is represented as a parallel-plate transmission line that connects in a circle around the vessel. This transmission line is divided into N sections, where each section is modeled as the circuit shown in Figure D-1(b). Here, i_{src} is a source term used to modeled an incident wave present at the slot, and v_k and i_k are the nodal voltage and current. Along the propagation direction (around the slot circumference), we define the kth element to have inductance, capacitance, and conductivity given by L_k, C_k, and G_k, respectively. For simplicity, we make the length of each slot section (in the propagation direction) equal to a constant value Δz. Note that nonzero conductance is only used in the model where electrical contact is modeled, and it is assumed in this initial model that there is no loss term (resistance) in the propagation direction.

The slot is modeled as a parallel-plate transmission line, where the gap between plates is w and the slot depth (the plate dimension transverse to the propagation direction) is d. In this case, the inductance and capacitance of a single section are

$$L_k = \Delta z \, \mu_0 w/d, \tag{D.1}$$

$$C_k = \Delta z \, \varepsilon_0 d/w. \tag{D.2}$$

In the case of a contact, the conductance can be related to the conductivity of the effective fill material. Assuming an effective conductivity of σ_{eff},

$$G_k = \Delta z \, \sigma_{\text{eff}} d/w. \tag{D.3}$$

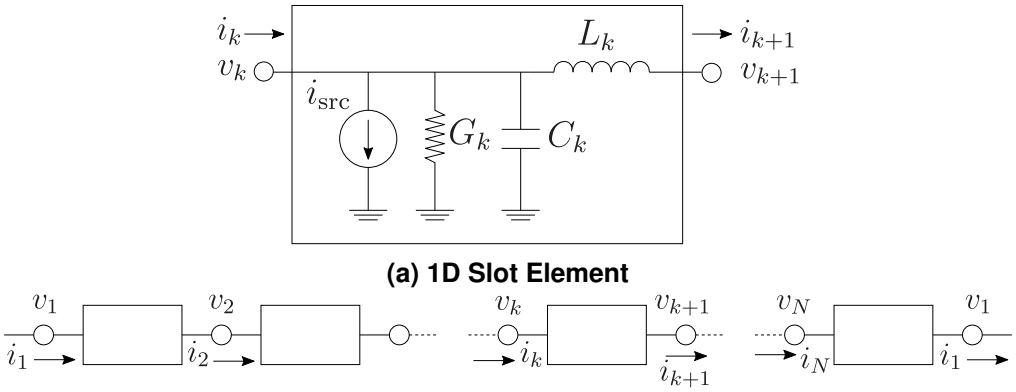

Figure D-1. 1D transmission line slot model: (a) single slot section, and (b) ensemble of connected slot elements. Figure (b) shows the configuration as a circumferential slot, where the last node connects back to the first node. However, a finite slot can also be modeled by connecting a shunt resistor or a short at the boundary nodes.

The governing equations for the transmission line section shown in Figure D-1(a) are easily derived using Kirchhoff's laws as

$$v_{k+1} = v_k - j\omega i_{k+1} L_k \tag{D.4}$$

$$i_{k+1} = i_k - v_k(G_k + j\omega C_k) - i_{\text{src}}. \tag{D.5}$$

For a circumferential slot with N sections, (D.4) and (D.5) form a set of $2N$ equations that can be written as the sparse matrix equation

$$\underbrace{\begin{bmatrix} \overline{\overline{A}}_{vv} & \overline{\overline{A}}_{vi} \\ \overline{\overline{A}}_{iv} & \overline{\overline{A}}_{ii} \end{bmatrix}}_{\overline{\overline{A}}} \underbrace{\begin{bmatrix} \bar{v} \\ \bar{i} \end{bmatrix}}_{\bar{x}} = \underbrace{\begin{bmatrix} 0 \\ \bar{i}_{\text{src}} \end{bmatrix}}_{\bar{x}_0}, \tag{D.6}$$

which can be solved using matrix inversion as $\bar{x} = \overline{\overline{A}}^{-1}\bar{x}_0$. In the case of a finite slot with N nodes, there are $N-1$ sections, and (D.4) and (D.5) provide only $2(N-1)$ equations. A simple boundary condition is to terminate the left and right boundaries with a shunt resistance, in which case we have the additional two equations

$$v_1 = -R_{\text{left}} i_1, \tag{D.7}$$

$$v_N = R_{\text{right}} i_N. \tag{D.8}$$

The source term in the 1D model can be found for normal plane wave incidence by considering Figure D-2. Here, the slot is driven by a relatively open parallel plate section having a large width w_{in}. A TEM wave is assumed to propagate inside this source parallel plate section from left to right toward the slot, where the slot has width w and depth d. We consider a single section of the 1D model, which means the length of the depicted section looking into the page is Δz. The voltage that is applied to the slot is given by

$$v_{\text{in}} = -E_{\text{inc}} w_{\text{in}}, \tag{D.9}$$

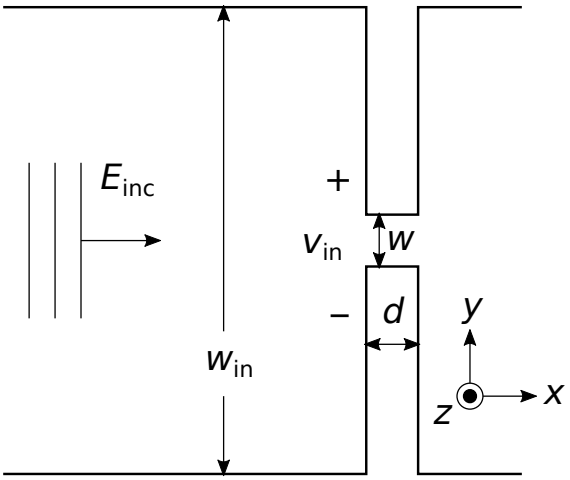

Figure D-2. Input source model used for normal plane-wave incidence on the slot. Note that x is the propagation of the incident plane wave, while z is the propagation direction of the wave along the vessel slot.

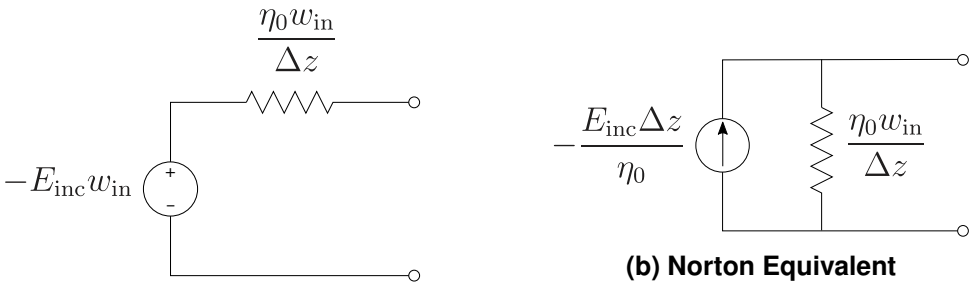

(a) Thevenin Equivalent

(b) Norton Equivalent

Figure D-3. Equivalent sources derived from the input parallel-plate transmission line model shown in Figure D-2.

where E_{inc} is the electric field intensity of the incident wave. The characteristic impedance of the source input line (the wide parallel plate transmission line) is

$$Z_{0,\text{in}} = \sqrt{\frac{L'_{\text{in}}}{C'_{\text{in}}}}, \tag{D.10}$$

where L'_{in} and C'_{in} are the inductance and capacitance of the parallel plate transmission line per unit length in the x dimension. We have

$$Z_{0,\text{in}} = \sqrt{\frac{\mu_0 w_{\text{in}}/\Delta z}{\varepsilon_0 \Delta z / w_{\text{in}}}} = \eta_0 \frac{w_{\text{in}}}{\Delta z}. \tag{D.11}$$

Thus, the parallel-plate input source can be represented as the equivalent Thevenin source shown in Figure D-3(a), or as the corresponding equivalent Norton source shown in Figure D-3(b). To transform the input parallel-plate line to a free-space plane wave, we can let the height w_{in} approach infinity, which has the effect of creating an infinite shunt resistance in the Norton model, allowing us to remove that element. This leaves just the Norton current source, which gives the value for i_{src} we should use for each section in the 1D equivalent circuit model.

Local Port	Global Node	
	Row (r)	Columns (c)
1	m	$2n+1$
2	m	$2n+2$
3	$m+1$	$2n+1$
4	m	$2n$

Table D-1. Local port index to global node row and column mapping for the 2D cell at location (m,n).

D.2. Two-Dimensional Slot Model

One of the limitations of the 1D model is that a contact point basically shorts the entire slot from the inside edge to the outside edge. Also, for increasing frequencies, variation of the slot fields with depth will become increasingly important. This section develops a 2D slot model based on transmission-line theory that is a natural extension of the 1D model presented in Section D.1. This type of 2D lattice to represent behavior in the slot is very similar to the *ladder network model* that is presented in [8], but the treatment here is made somewhat simpler by starting with a circuit-based approach.

Figure D-4 depicts the 2D slot model that was developed. The 2D slot element shown in Figure D-4(a) presents a shunt capacitance for the parallel-plate slot, along with a shunt conductance where contact needs to be modeled. A shunt current source is provided to allow incident fields to be modeled at the slot edge. Lateral connections with adjacent slot elements in the four cardinal directions are accomplished using inductances, representing a natural extension of the 1D model.

The connection arrangement for the 2D slot model is shown in Figure D-4(b), consisting of an $N_x \times N_y$ grid of elements, where the N_x elements are along the slot length dimension, and the N_y elements are along the slot depth dimension. Assigning global numbering to ports is complicated by the staggered port arrangement. To simplify global node assignment, a global node row and column arrangement is used as shown in Figure D-4(b). For the 2D cell at location (m,n), the local ports get mapped to global row and column indices as given in Table D-1. Given global row and column node indices of r and c, respectively, a single stacked global node index is computed as $k = r + c(2N_y + 1)$.

The governing equations for the 2D slot element are again derived using Kirchhoff's laws, giving the four equations

$$v_1 - j\omega L_1 i_1 - v = 0 \tag{D.12}$$

$$v_2 - j\omega L_2 i_2 - v = 0 \tag{D.13}$$

$$v_3 + j\omega L_3 i_3 - v = 0 \tag{D.14}$$

$$v_4 + j\omega L_4 i_4 - v = 0 \tag{D.15}$$

where the internal node voltage v is given by

$$v = \frac{i_1 + i_2 - i_3 - i_4 - i_{\text{src}}}{G + j\omega C}. \tag{D.16}$$

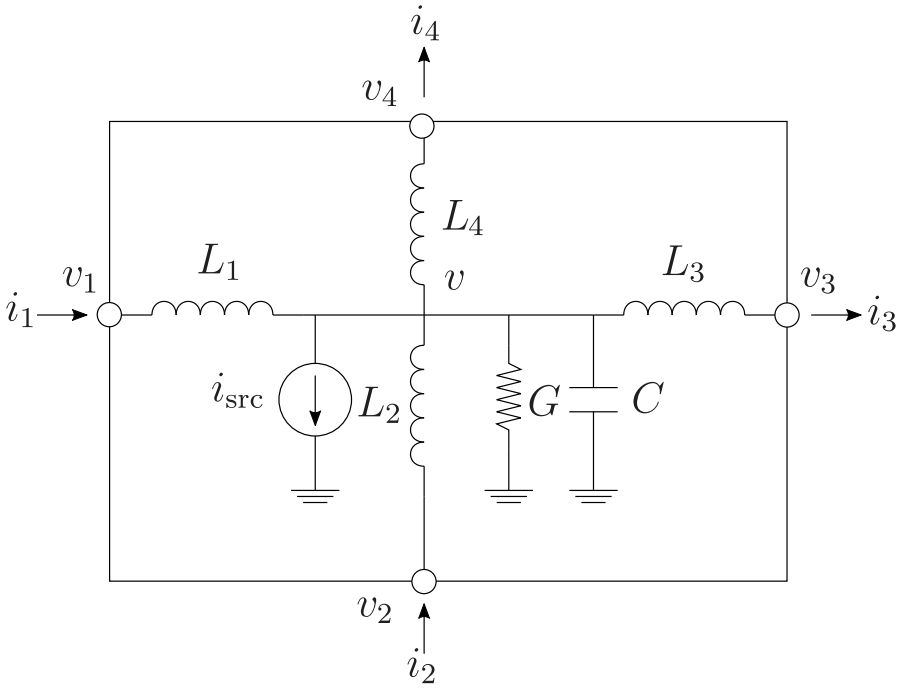

(a) 2D Slot Element

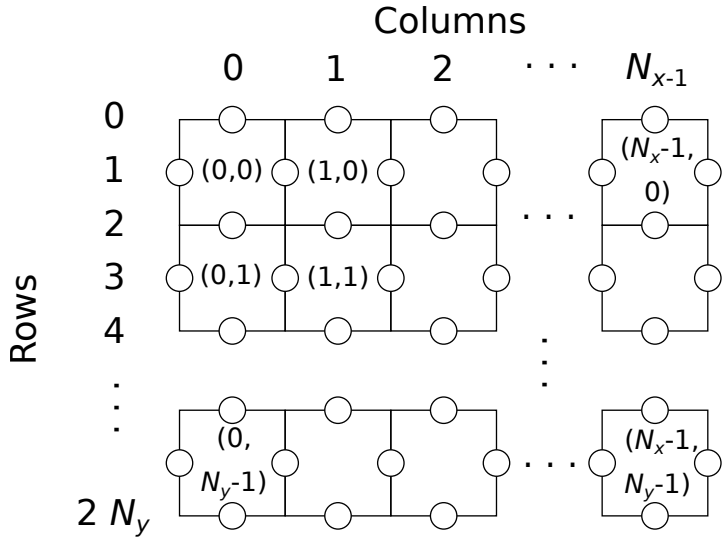

(b) 2D Slot Ensemble

Figure D-4. 2D transmission line slot model: (a) single slot section, and (b) grid showing the connection pattern of connected slot elements. Note that in (b), we will model the top and bottom rows as lying on the outside and inside slot edges, respectively. Also, zero indexing will be used for node and element numbers in the 2D model.

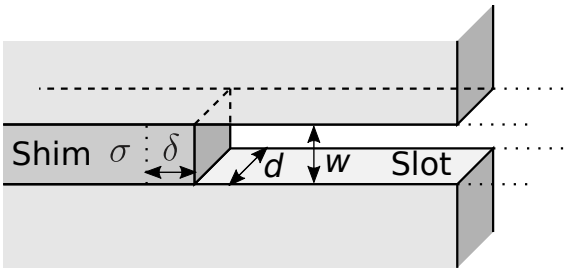

Figure D-5. Derivation of approximate RF shim resistance using the skin effect.

For a circumferential slot, we have $N_x(2N_y+1)$ total nodes and N_xN_y cells. Since we have an unknown voltage and current at each node, we have $4N_xN_y+2N_x$ unknowns. The open nodes on the inside and the outside slot edges have zero current, removing $2N_x$ unknowns. Since we have four equations per cell, this gives $4N_xN_y$ equations for the $4N_xN_y$ unknowns. The equations can be formed into a matrix equation as with the 1D model and solved using a matrix inverse.

D.3. Effective Shim Resistance

In CST modeling, an effective DC resistance was used for the shims, which has the advantage of being frequency independent. However, in the 1D and 2D slot models, an actual contact resistance is specified, which can be frequency dependent. Here we develop an approximate relationship between the shim DC resistance and the realized RF resistance at the edge of the shim, where this latter quantity should be the value used in the 1D and 2D modeling approach.

The unusual shim shape was chosen to create slots that have a constant length with depth. As was seen in the simulations in Chapter 2, slot fields tend to favor a field distribution that is uniform in *angle* for the cylindrical cavity, which is not uniform with respect to *length*. This causes the field at the shim to be changing with respect to depth, which complicates defining a mapping between the DC resistance of the shim and its realized RF resistance.

As a first-order approximation, we will compute the resistance mapping for the case of a shim having a constant angular extent with depth. Such a shim would support a nearly constant field at the slot edge width respect to depth, which allows simple computation of the skin effect and resulting resistance. Development of a more exact expression is left for future investigation.

We can relate effective contact resistance at the edge of the shim to the shim material conductivity by approximating the shim to be the rectangular slab shown in Figure D-5. The shim depth and width are equal to the slot depth and width, represented by d and w. Assuming a shim with good conductivity, the physical length of the shim will be considered semi-infinite, and the effective length will be set by the skin effect. The skin depth is given by

$$\delta = \sqrt{2/(\omega\mu_0\sigma)}, \tag{D.17}$$

where ω is the circular excitation frequency, μ_0 is the free-space permeability, and σ is the shim conductivity. The resistance of the slab at the slot edge is defined as

$$R = \frac{1}{\sigma}\frac{w}{\delta d} = \sqrt{\frac{\omega\mu_0}{2\sigma}}\frac{w}{d}. \tag{D.18}$$

Previously, we used the DC resistance of the shims as a parameter of interest, given by

$$\sigma = \frac{w}{A\,R_{\mathrm{DC}}}, \tag{D.19}$$

where R_{DC} is the DC shim resistance and A is the cross-sectional area of the shim. Relating (D.18) and (D.19) we have

$$R = \frac{1}{d}\sqrt{\frac{\omega\mu_0 A R_{\mathrm{DC}} w}{2}}. \tag{D.20}$$

D.4. Slot Radiation Green's Function

The 1D and 2D slot models predict slot voltage, which is the quantity of interest for embedded probes. However, for near-field probing with an external probe, fields near the slot are of interest. Fields that are radiated from the slot can be efficiently computed from the voltage (or field) at the slot edge using a Green's function. This section derives a simplified Green's function that can be used to predict observed fields in the plane of a slot at proximate observation distance. See [1] for related material on Green's function analysis and radiation from apertures.

Figure D-6(a) shows a radiating slot edge that is confined to the xy plane, but is otherwise arbitrary in shape. The coordinate of a source point along the slot edge is represented by the coordinate vector $\bar{r}'$, while the coordinate of a desired field observation point is given by the vector $\bar{r}$. Given that we know the voltage at the slot edge, given by $v(\bar{r}')$, the electric field at the slot edge is $\overline{E}_a(\bar{r}') = -v(\bar{r}')/w\,\hat{z}$, where w is the width of the slot at the edge, and $\overline{E}_a$ stands for electric field at the slot "aperture." Using image theory, the slot and metal walls can be replaced by a magnetic surface current ($\overline{M}_s$) in free space according to

$$\overline{M}_s = -2\hat{n}' \times \overline{E}_a, \tag{D.21}$$

where $\hat{n}'$ is the outward normal vector from the slot edge in the xy plane. For a curved slot, the normal vector changes with position $\bar{r}'$, which we will define in terms of components as

$$\hat{n}' = n'_x\hat{x} + n'_y\hat{y}, \tag{D.22}$$

where the dependence on $\bar{r}'$ has been suppressed. The effective magnetic current in the slot aperture becomes

$$\overline{M}_s = 2E_{a,z}(n'_x\hat{y} - n'_y\hat{x}). \tag{D.23}$$

A vector potential approach can be used to find fields radiated from the magnetic surface current according to [1]

$$\overline{F}(\bar{r}) = \int \overline{M}(\bar{r}')g(\bar{r},\bar{r}')dA' \tag{D.24}$$

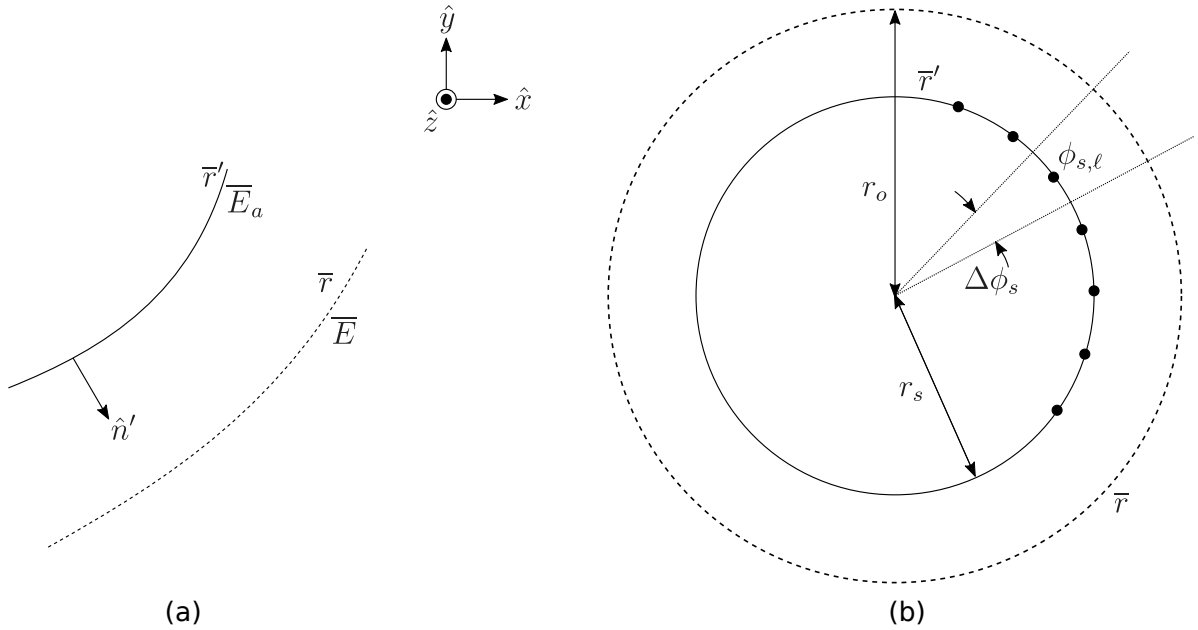

Figure D-6. Source and observation coordinates used for the derivation of a simplified slot Green's function. In (a), an arbitrary slot shape is considered, where slot aperture fields $\overline{E}_a$ at source coordinate $\overline{r}'$ radiate and are observed as $\overline{E}$ at observation coordinate $\overline{r}$. The work in this report considers cylindrical surfaces, which can be parameterized with respect to source and observation angle as shown in (b).

where the integration is over the area of the slot aperture, and the scalar Green's function is given by

$$g(\overline{r},\overline{r}') = \frac{\varepsilon}{4\pi}\frac{e^{-jkR}}{R}, \tag{D.25}$$

where ε and μ are the permittivity and permeability of the surrounding medium (usually free space), $k = \omega\sqrt{\mu\varepsilon}$ is the wavenumber, and $R = \|\overline{r} - \overline{r}'\|$. The radiated (or observed) electric field can be found from (D.24) according to

$$\overline{E} = -\frac{\nabla \times \overline{F}}{\varepsilon}, \tag{D.26}$$

where $\nabla\times$ is the curl operator. To simplify the computation of the Green's function, we note that the magnetic current $\overline{M}_s$ only has $\hat{x}$ and $\hat{y}$ components, which means that $\overline{F}$ will also only have $\hat{x}$ and $\hat{y}$ components. Also, for the probes of practical interest in this work, we will only observe the $\hat{z}$ component of the electric field and do so in the xy plane (i.e., $z = z'$). The curl operation in (D.26) can therefore be computed as

$$(\nabla \times \overline{F})_z = \begin{vmatrix} \hat{x} & \hat{y} & \hat{z} \\ \partial/\partial x & \partial/\partial y & \partial/\partial z \\ F_x & F_y & 0 \end{vmatrix}_z = \frac{\partial F_y}{\partial x} - \frac{\partial F_x}{\partial y}. \tag{D.27}$$

Substituting into (D.24) and (D.26) observed field is given by

$$E_z = \frac{1}{\varepsilon}\int \left[M_x(\overline{r}')\frac{\partial g(R)}{\partial y} - M_y(\overline{r}')\frac{\partial g(R)}{\partial x} \right] dA'. \tag{D.28}$$

The magnetic current components of (D.28) are given by

$$M_x(\bar{r}') = -2E_{a,z}n'_y, \tag{D.29}$$

$$M_y(\bar{r}') = 2E_{a,z}n'_x, \tag{D.30}$$

and the scalar Green's function derivatives are given by

$$\frac{\partial g(R)}{\partial p} = \frac{\varepsilon}{4\pi}\frac{p-p'}{R^2}e^{-jkR}\left(jk+\frac{1}{R}\right), \tag{D.31}$$

where $p \in \{x,y\}$. Combining these results simplifies (D.28) to

$$E_z = \frac{1}{2\pi}\int \frac{E_{a,z}}{R^2}e^{-jkR}\left(jk+\frac{1}{R}\right)\underbrace{\left[n'_x(x-x')+n'_y(y-y')\right]}_{\hat{n}'\cdot(\bar{r}-\bar{r}')}dA' \tag{D.32}$$

Typically in this work we are concerned with cylindrical vessels, as shown in Figure D-6(b). Source and observation locations are parameterized by the azimuthal angles ϕ_s and ϕ_o, respectively, where

$$\bar{r}' = r_s\left(\hat{x}\cos\phi_s + \hat{y}\sin\phi_s\right) \tag{D.33}$$

$$\bar{r} = r_o\left(\hat{x}\cos\phi_o + \hat{y}\sin\phi_o\right), \tag{D.34}$$

and r_s and r_o are the radii of the slot edge and observation circle, respectively. The outward normal on the source aperture is

$$\hat{n}' = \hat{x}\cos\phi_s + \hat{y}\sin\phi_s. \tag{D.35}$$

The integral in (D.32) can be computed with respect to the variables ϕ_s and z. Assuming constant aperture fields over an extent of Δz in the z direction, where zero field is assumed on the surface of the cylinder, we can compute the integration using a simple midpoint rule in ϕ_s, or

$$E_z(\bar{r}) = \frac{r_s\Delta z\Delta\phi_s}{2\pi}\sum_{\ell=1}^{N}\frac{E_{a,z}(\phi_{s,\ell})}{R_\ell^2}e^{-jkR_\ell}\left(jk+\frac{1}{R_\ell}\right)\hat{n}'_\ell\cdot(\bar{r}-\bar{r}'_\ell), \tag{D.36}$$

where

$$R_\ell = \|\bar{r}-\bar{r}'_\ell\|, \tag{D.37}$$

$$\bar{r}'_\ell = r_s\left(\hat{x}\cos\phi_{s,\ell} + \hat{y}\sin\phi_{s,\ell}\right), \tag{D.38}$$

$$\phi_{s,\ell} = \ell\Delta\phi_s, \quad \ell \in \{1,2,\ldots,N\}, \tag{D.39}$$

and $\Delta\phi_s = 2\pi/N$.

One problem with a curved aperture surface is that slot fields (and equivalent magnetic currents) on the back side of the cylinder will be shadowed, which is not taken into account in the Green's function integrations developed here. To partially correct this deficiency for cylindrical vessels, we can define a maximum separation angle of source and observation, above which aperture fields are assumed to be shadowed. More precisely we define a visibility function

$$P(\phi_s,\phi_o) = \begin{cases} 1, & |\phi_s-\phi_o| \le \phi_{\max}, \\ 0, & \text{otherwise}, \end{cases} \tag{D.40}$$

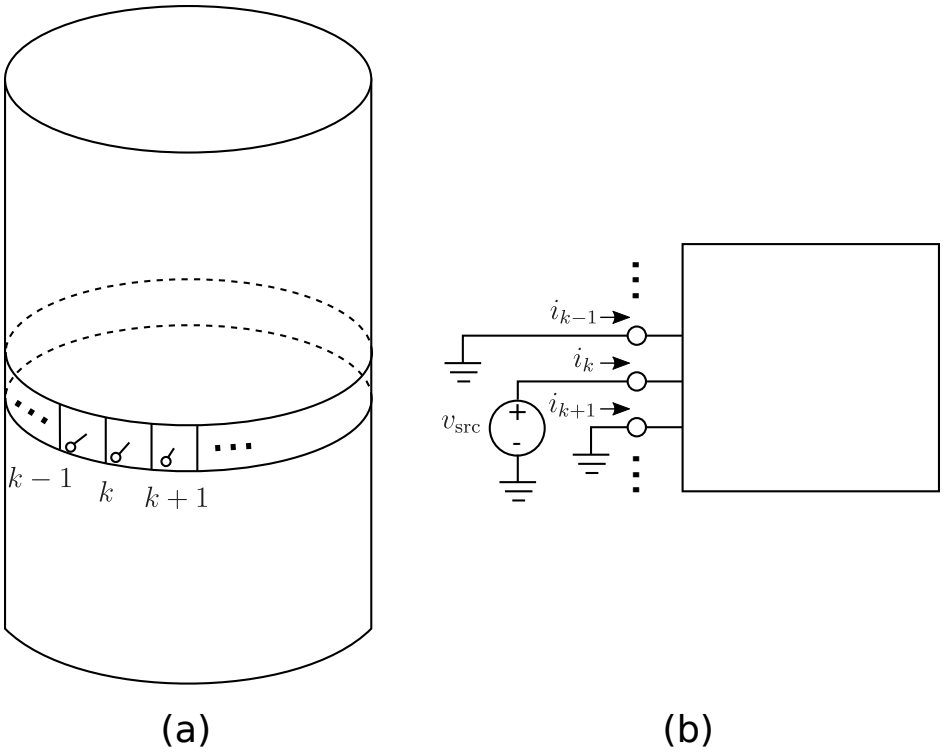

Figure D-7. Conceptual development of a circuit-based cavity model, where cavity walls in (a) are meshed into quads over the area of the slot aperture. Each mesh element becomes a port in the equivalent circuit model of the cavity in (b). The admittance matrix of the cavity circuit model can be found by successively exciting each port with a constant voltage and measuring the resulting short-circuit current on all the other ports.

where $\phi_{\max}$ is the maximum angular separation of source and observation for visibility of aperture fields. In this work we have used $\phi_{\max} = 90°$, allowing half of the cylindrical surface to be seen for each observation angle. Including the visibility function, we can rewrite (D.36) as

$$E_z(\phi_o) = \frac{r_s \Delta z \Delta \phi_s}{2\pi} \sum_{\ell=1}^{N} P(\phi_{s,\ell}, \phi_o) \frac{E_{a,z}(\phi_{s,\ell})}{R_\ell^2} e^{-jkR_\ell} \left(jk + \frac{1}{R_\ell} \right) \hat{n}'_\ell \cdot (\bar{r} - \bar{r}'_\ell). \tag{D.41}$$

D.5. Cavity Modeling

Sections D.1 and D.2 provide equivalent linear circuit models for slots in either 1D or 2D. The Green's function in Section D.4 allows radiation from slots to be computed. The missing piece is an equivalent circuit model for the interior of the cavity that properly loads and couples slot elements together. This section provides a sketch of how this could be accomplished, leaving implementation for future work.

Figure D-7(a) depicts a cylindrical cavity, whose slot area has been identified and meshed into N discrete ports. Note that the goal here is only to model the interior of the cavity, so the ports are connected to the inside cavity surface. For simple slot shapes, the ports could occupy small

rectangles on the inside cavity surface. Figure D-7(b) shows the circuit representation of the same cavity.

The admittance matrix of the cavity can be determined by performing analysis or numerical simulation, where the kth port is driven with a voltage v_{src}. In the physical cavity, this would correspond to driving the rectangular patch for that port with a constant z-directed tangential electric field (E_t), such that $E_t = -v_{\text{src}}/\Delta z$, where Δz is the height of the rectangular patch. PEC metal patches are placed at the other port locations, which correspond to short circuits in the circuit model. Measuring the currents that occur on all of the port patches (including the driven one) gives the kth column of the admittance matrix $\overline{\overline{Y}}$, or

$$Y_{\ell k} = i_\ell / v_{\text{src}}. \tag{D.42}$$

Performing this analysis or simulation for $k = 1, 2, \ldots, N$ then provides all the columns of the admittance matrix. If desired, the admittance matrix can be inverted to give the impedance matrix $\overline{\overline{Z}}$ for the cavity. The admittance or impedance matrix now provides the link between voltages and currents on the inner vessel boundary for either the 1D or 2D circuit model, or

$$i_\ell = \sum_k Y_{\ell k} v_k, \tag{D.43}$$

$$v_\ell = \sum_k Z_{\ell k} i_k, \tag{D.44}$$

where i_ℓ and v_ℓ are the inward flowing current and voltage on the ℓth cavity port. It is simplest to use these relations to augment the 2D circuit model. Instead of setting $i = 0$ on the inner N ports as was done previously, we now have N equations given by either (D.43) or (D.44).

Note that for large slots and cavities, simulating the vessel N times (once for each driven port) could be an expensive operation. However, vessels that have rotational symmetry like the cylinder would only require a single simulation to find a single column of $\overline{\overline{Y}}$. Due to symmetry, the remaining columns are circulant shifts of the one unique column.

D.6. Comparison of 1D Slot Model with EIGER

The validity of using the simple 1D model from Section D.1 was checked by comparing its predictions with high-fidelity simulations of Vessel 2 in EIGER. Figure D-8 shows the geometry of Vessel 2 that was simulated in EIGER. The shims have been removed, and the slot is modeled using EIGER's sub-cell slot model as a circumferential slot. The slot area is divided into 180 quads (one quad per 2° of arc), which matches the resolution to be used in the 1D slot model. EIGER allows the slot width and the conductivity of gasket material to be varied for each slot quad. The same parameters can be varied in a 1D slot simulation using the simple method in Section D.1 and the results can then be compared.

Simulations were performed at 753.4 MHz, which is the lowest resonance of Vessel 2. In EIGER, a 1 cm monopole probe in the center of one of the inside circular faces excites vessel fields. In the case of the 1D slot simulations, a constant current source ($i_{\text{src}} = 1$) drives all of the slot elements

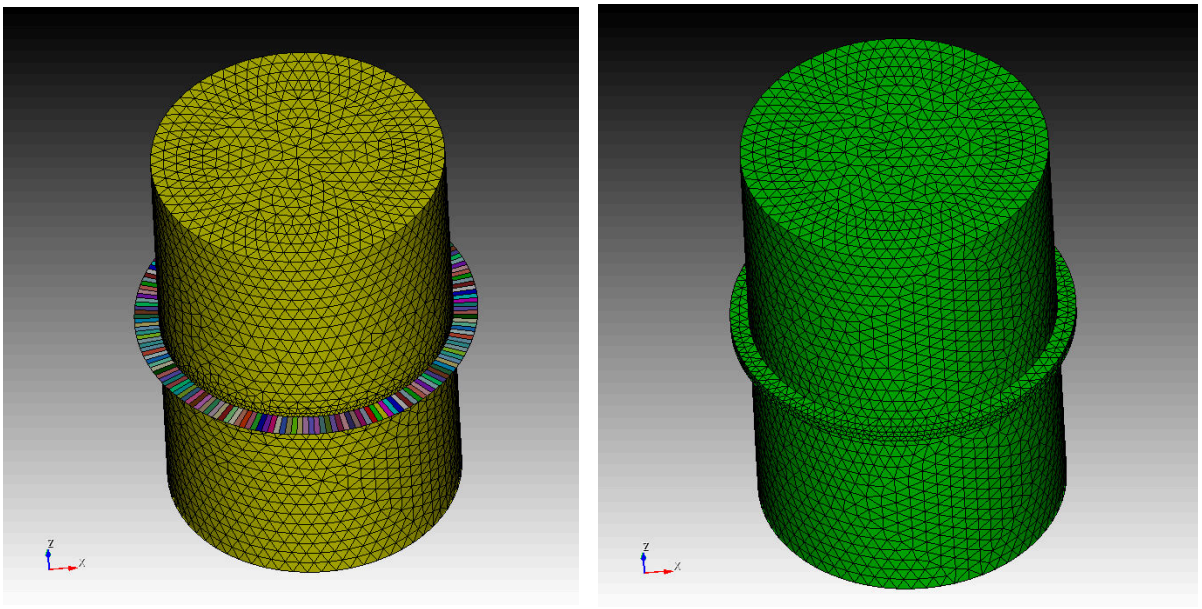

(a) Inside Surface and Slot Quads **(b) Outside Surface**

Figure D-8. CUBIT model of Vessel 2 that was simulated in EIGER. The inside and outside geometries are shown in (a) and (b), respectively. The slot area has been meshed with 180 quads, allowing a circumferential slot to be simulated with EIGER's sub-cell thick slot model.

with equal weight. In EIGER, near fields are computed using Moench at a distance of 5 mm from the slot flange. For the 1D slot simulations, we consider both the slot voltages as well as electric field 5 mm from the flange, where the latter is computed using the Green's function developed in Section D.4.

Figure D-9 shows the somewhat arbitrary physical parameters that were chosen for the example slot simulations. In these simulations bolts were assumed to be located at 45°, 135°, 225°, and 315°, where the shunt element resistance is set to $R = 0.01\ \Omega$ and the gap width is set to 0.1 mil. For the 1D slot model, element conductance is used, which at the bolts is $G = 1/R = 100\ \Omega^{-1}$. In EIGER, the shunt resistance is converted into a conductivity of the gasket fill material using

$$\sigma = \frac{w}{RA}, \tag{D.45}$$

where $A = 0.2269\ \text{inch}^2 = 1.4638 \times 10^{-4}\ m^2$ is the area of a single slot quad and w is the slot width. To include the effect of changes in slot width and distributed contacts, four 90° sectors around each bolt were defined, having element shunt resistances of 0.1, 0.2, 0.4, and 0.8 Ω, and slot widths of 1, 2, 0.5, and 2.5 mil.

Figure D-10 compares the resulting output of the 1D slot simulations and the 3D EIGER simulations. In the first EIGER simulations shown in Figure D-10(a), each bolt was simulated as a single filled quad, which is referred to as the "narrow bolt" case. The figure shows that the slot voltage at bolt locations exhibits somewhat deeper nulls than the fields at 5 mm separation from the slot aperture. The EIGER simulations have a similar trend in fields except at the bolt locations, where EIGER predicts a much shallower null.

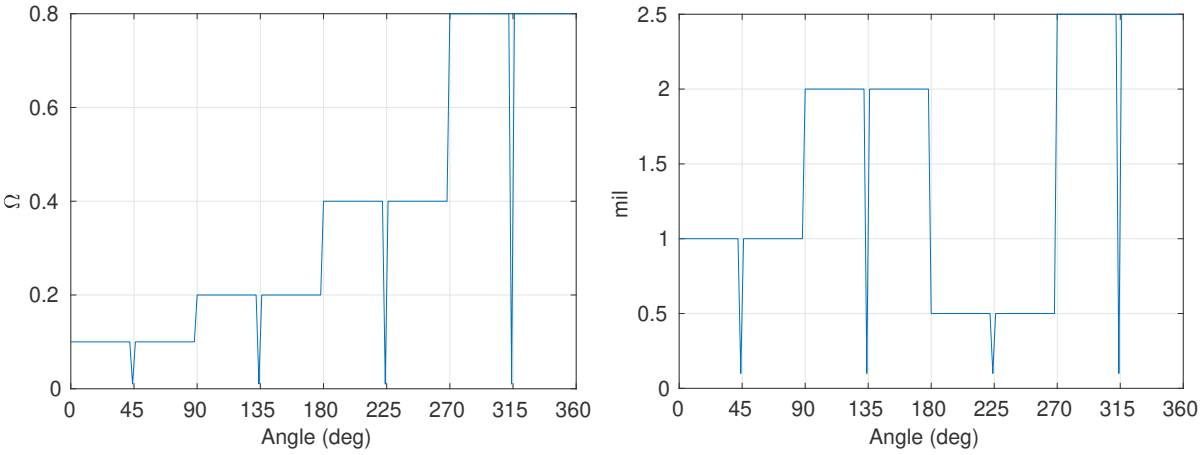

(a) Element Shunt Resistance **(b) Element Slot Width**

Figure D-9. Slot parameters versus angle that were specified for the EIGER and 1D slot simulations.

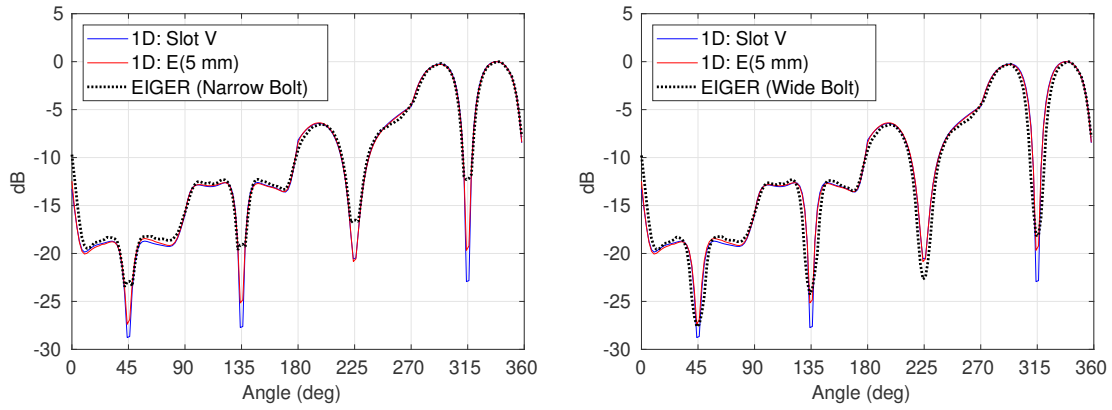

(a) Narrow Bolt **(b) Wide Bolt**

Figure D-10. Comparison of results from the 1D slot model with detailed 3D EIGER simulations. All curves have been normalized to a maximum value of 0 dB. Two outputs are shown for the 1D slot model: raw slot voltages (Slot V) and near-fields 5 mm from the flange, computed using the Green's function method (E(5 mm)). Figures (a) and (b) compare with EIGER simulation assuming a single slot quad per bolt, and three slot quads per bolt, respectively.

One mismatch between EIGER and the 1D slot model is that EIGER uses piecewise linear basis functions for magnetic currents on the slot elements, whereas the 1D slot model uses a piecewise constant representation. When a quantity changes abruptly at a point (such as at the bolts), this could cause a significant mismatch in the modeling results. To simulate something closer to a piecewise constant current at the bolt location, the EIGER simulation was changed so that the bolt parameters (high conductivity and narrow slot width) occupy *three* slot quads instead of a single quad. The results are shown in Figure D-10(b), showing that 1D slot simulations combined with the Green's function operator provide fairly close results to the modified EIGER simulation.

D.7. Conclusion

This chapter has developed reduced order models for slot modeling. 1D and 2D models based on transmission line equivalent circuits were given in Sections D.1 and D.2, respectively. The native output of the transmission line models is slot voltage, which can show slightly different behavior as compared to fields some distance from the slot. For this reason, a Green's function method for computing fields near radiating slots was derived in Section D.4. Predictions of the 1D slot model were compared with detailed 3D EIGER simulations in Section D.6, illustrating that near-field behavior of slots can be faithfully predicted with simple 1D simulations coupled with the Green's function operator.

APPENDIX E. Shielding Effectiveness Computation

This chapter gives expressions that were used in this work to compute measured and simulated shielding effectiveness (SE). Section E.1 develops the expression used for computing the usual *receive mode* SE value given a calibrated measurement and known gain of the illuminating antenna and vessel probe. Section E.2 provides a derivation that allows computation of SE using a *transmit mode* simulation or measurement by applying reciprocity considerations.

E.1. Receive-Mode SE Measurement

Figure E-1 shows the usual setup for performing a shielding effectiveness (SE) measurement. It is assumed that the cabling at Ports 1 and 2 have been calibrated out, so that the quantity P_R is the power from the vessel probe at Port 2 that would be delivered into a Z_0 load (i.e, available power). Likewise, P_T is the available power at the end of the cable attached to the illuminating antenna at Port 1 for a load of Z_0. If measurements are performed with a calibrated network analyzer, these definitions give the usual $|S_{21}|^2 = P_R/P_T$.

In this work, a spectrum analyzer with a tracking generator was used. A through calibration was performed by connecting the transmit signal at Port 1 directly to the receive cable input at Port 2 through a known attenuator gain of G_{atten} (note the gain is negative). This allows the combined transmit/receive gain of the system and cables to be estimated as

$$G_{\text{sys}} = \frac{P_{R,\text{cal}}}{G_{\text{atten}} P_{T,\text{gen}}}, \tag{E.1}$$

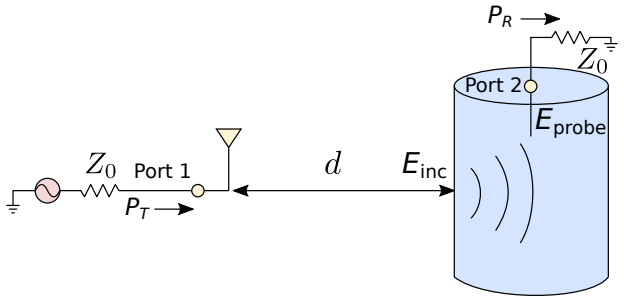

Figure E-1. Usual *receive mode* SE measurement setup. A transmit source is connected to Port 1 having an available power P_T, and the available receive power P_R at Port 2 is measured. The transmit antenna is placed a distance d from the vessel. SE is computed from the ratio of the internal electric field at the probe ($\overline{E}_{\text{probe}}$) to that incident on the vessel ($\overline{E}_{\text{inc}}$).

where $P_{T,\text{gen}}$ is the assumed transmit power level of the tracking generator (0 dBm in this work), and $P_{R,\text{cal}}$ is the receive power measured in the through calibration configuration. A raw receive power measurement of $P_{R,\text{raw}}$ can then be calibrated to get the transfer function with system losses removed according to

$$\frac{P_R}{P_T} = \frac{P_{R,\text{raw}}}{G_{\text{sys}} P_{T,\text{gen}}} = \frac{P_{R,\text{raw}} G_{\text{atten}}}{P_{R,\text{cal}}}. \tag{E.2}$$

Returning to Figure E-1, assuming that the transmit antenna has a gain G_T and is spaced a distance d from the vessel, incident power density at the vessel is

$$W_{\text{inc}} = \frac{\|\overline{E}_{\text{inc}}\|^2}{2\eta_0} = \frac{P_T G_T}{4\pi d^2}. \tag{E.3}$$

Available power from the vessel probe is given as

$$P_R = \frac{\|\overline{E}_{\text{probe}}\|^2}{2\eta_0} A_{eR} \tag{E.4}$$

$$P_R = \frac{\|\overline{E}_{\text{probe}}\|^2}{8\pi\eta_0} G_R \lambda^2, \tag{E.5}$$

where A_{eR} is the effective receive area of the vessel probe, which is related to the probe gain according to $A_{eR} = G_R\lambda^2/(4\pi)$, where λ is the wavelength. We may now divide (E.5) by (E.3) to obtain

$$\frac{\|\overline{E}_{\text{probe}}\|^2}{\|\overline{E}_{\text{inc}}\|^2} = \frac{P_R}{P_T} \frac{(4\pi d)^2}{G_R G_T \lambda^2}. \tag{E.6}$$

This final expression is the SE value at the probe in linear power units. Thus, SE in dB can be computed as

$$\text{SE}_{\text{dB}} = 10\log_{10}\left[\frac{P_R}{P_T}\frac{(4\pi d)^2}{G_R G_T \lambda^2}\right] \tag{E.7}$$

$$= S_{21,\text{dB}} - G_{T,\text{dB}} - G_{R,\text{dB}} + 20\log_{10}\frac{4\pi d}{\lambda}. \tag{E.8}$$

It is interesting to note that these final expressions are identical to the Friis transmission formula, with SE appearing an addition gain term.

E.2. Reciprocal Transmit-Mode SE Measurement

This section derives how shielding effectiveness (SE) can be measured or simulated in a vessel's *transmit mode*, which can be more convenient in some scenarios. For a standard SE measurement, we have an external antenna placed a distance d from the vessel that radiates a known incident field intensity $\|\overline{E}_{\text{inc}}\|$ at the vessel. We then measure the signal from a probe in the vessel, and use the known gain of the probe to obtain $\|\overline{E}_{\text{probe}}\|$, allowing SE computed as

$$\text{SE} = 10\log_{10}\frac{\|\overline{E}_{\text{probe}}\|^2}{\|\overline{E}_{\text{inc}}\|^2}. \tag{E.9}$$

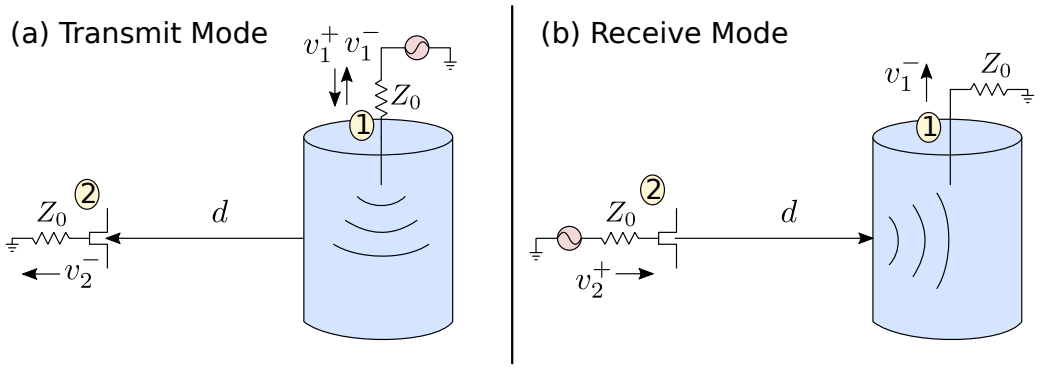

Figure E-2. Two SE measurement arrangements that are related in this section: (a) transmit mode measurement, where the probe in the vessel is used as a transmit antenna and fields are measured outside the vessel, and (b) receive mode measurement, where the external antenna is driven and signals from the vessel probe are measured to estimate internal field.

Since the probe is receiving, we will call this the *receive mode* case.

In the case of a reciprocal measurement, we excite the probe (now an antenna) that is inside the vessel and measure radiated fields outside. From this measurement we would like to still estimate (E.9) above. We will refer to this second measurement technique as the *transmit mode* case.

E.2.1. Transmit Mode

We will begin with the transmit mode which is often the more convenient measurement setup, and later relate this to the receive mode, which more directly gives the SE value we are interested in.

Figure E-2(a) depicts the transmit mode. We will assume a system with all ports terminated by impedance Z_0. Port 1 is the probe in the vessel, and forward and reverse waves v_1^+ and v_1^-, respectively, are present at the port. Signals from the probe propagate into the vessel, radiate out ports of entry (POEs), and eventually are received by a far-field receive antenna at Port 2. We assume this second antenna is far enough away from the vessel that it does not scatter significant energy back to the vessel and Port 1. Also, note that the type of far-field antenna and its properties are mostly arbitrary, since we are only using it to relate power radiated in the transmit mode to incident power in the receive mode.

The power incident (available power) into Port 1 is

$$P_{\text{in}} = \frac{1}{2}\frac{|v_1^+|^2}{Z_0}. \tag{E.10}$$

Assuming that no significant energy scatters from the far-field antenna back to the vessel probe at Port 1 ($S_{12} \approx 0$) and that the antenna at Port 2 is matched ($S_{22} \approx 0$), we have

$$v_1^- = S_{11}v_1^+ + S_{12}v_2^+ \approx S_{11}v_1^+ \tag{E.11}$$

$$v_2^- = S_{21}v_1^+ + S_{22}v_2^+ \approx S_{21}v_1^+. \tag{E.12}$$

The power delivered to the load at Port 2 is related to the radiated field from the vessel incident on that antenna according to

$$P_L = \frac{1}{2}\frac{|v_2^-|^2}{Z_0} \tag{E.13}$$

$$= \frac{A_{e2}\|\overline{E}_{\text{rad}}\|^2}{2\eta_0}, \tag{E.14}$$

where $\overline{E}_{\text{rad}}$ is electric field radiated to the far-field and A_{e2} is the effective receive area of the antenna at Port 2. These expressions allow us to find the load voltage at Port 2 as

$$|v_2^-|^2 = \frac{A_{e2}Z_0\|\overline{E}_{\text{rad}}\|^2}{\eta_0} \tag{E.15}$$

$$= |S_{21}|^2 \underbrace{|v_1^+|^2}_{v_A^2}. \tag{E.16}$$

Effective area is related to the antenna gain according to

$$G = A_e\frac{4\pi}{\lambda^2}. \tag{E.17}$$

Note that we define v_A^2 to be $|v_1^+|^2$ for the *transmit mode only*. This quantity is proportional to the power delivered to the vessel probe in the transmit case. This avoids later confusion, because when we later relate the transmit and receive modes, the meaning of v_1^+ is ambiguous.

E.2.2. Receive Mode

Now we switch to the receive mode shown in Figure E-2(b). The same antennas are used at Ports 1 and 2, but now Port 2 is driven with an input signal v_2^+ and the signal v_1^- coming from the probe at Port 1 is measured. Note that the value of signals is not necessarily the same as in the transmit mode. However, the measurement configuration is otherwise identical in terms of the antenna/probe characteristics and the distance d.

The incident radiated power density present at the vessel is given by

$$\frac{\|\overline{E}_{\text{inc}}\|^2}{2\eta_0} = \frac{|v_2^+|^2}{2Z_0}\frac{G_2}{4\pi d^2}, \tag{E.18}$$

where G_2 is the gain of the antenna at Port 2. The receive signal at Port 1 is then given as

$$v_1^- = S_{12}v_2^+, \tag{E.19}$$

$$= S_{21}v_2^+, \tag{E.20}$$

where the second equality follows from reciprocity. Combining (E.20) with (E.18), we have

$$\underbrace{|v_1^-|^2}_{v_B^2} = |S_{21}|^2\frac{Z_0}{\eta_0}\frac{4\pi d^2}{G_2}\|\overline{E}_{\text{inc}}\|^2, \tag{E.21}$$

where the variable v_B^2 is proportional to power delivered to the probe at Port 1 *in the receive mode*. Considering the receiving properties of the probe at Port 1 we have

$$\frac{v_B^2}{2Z_0} = A_{e1}\frac{\|\overline{E}_{\text{probe}}\|^2}{2\eta_0}. \tag{E.22}$$

We now relate the receive mode to the transmit mode by eliminating S_{21} in (E.16) and (E.21):

$$v_B^2 = \frac{A_{e2}}{v_A^2}\frac{Z_0}{\eta_0}\|\overline{E}_{\text{rad}}\|^2\frac{Z_0}{\eta_0}\frac{4\pi d^2}{G_2}\|\overline{E}_{\text{inc}}\|^2. \tag{E.23}$$

Using (E.22), this can be simplified to

$$\frac{\|\overline{E}_{\text{probe}}\|^2}{\|\overline{E}_{\text{inc}}\|^2} = \underbrace{\frac{A_{e2}}{G_2}}_{\frac{\lambda^2}{4\pi}}\underbrace{\frac{2Z_0}{v_A^2}}_{\frac{1}{P_{\text{in}}}}\frac{\|\overline{E}_{\text{rad}}\|^2}{2\eta_0}\frac{4\pi d^2}{A_{e1}}, \tag{E.24}$$

or

$$\frac{\|\overline{E}_{\text{probe}}\|^2}{\|\overline{E}_{\text{inc}}\|^2} = \frac{1}{P_{\text{in}}}\frac{\|\overline{E}_{\text{rad}}\|^2}{2\eta_0}\frac{4\pi d^2}{G_1}. \tag{E.25}$$

This last expression can then be used to do a transmit mode measurement, and then predict the usual receive mode quantities. Specifically, we have a generator providing available power P_{in} to the vessel probe (antenna) at Port 1. We then measure $\|\overline{E}_{\text{rad}}\|$ at a distance d from the vessel. SE can then be found using (E.25), where G_1 is the gain of the field probe in the vessel.

Although it was suppressed, note that $\overline{E}_{\text{rad}}$ is a function of observation angle (azimuth and elevation), meaning that in the recirpocal case, $\overline{E}_{\text{inc}}$ depends on the same far-field angles. Therefore, if far fields are obtained on the complete radiation sphere, a single transmit-mode simulation can be used to obtain SE for all possible incident field directions from a single simulation. This is one advantage of the transmit-mode SE approach when many angles of incidence need to be considered, and the number of probes is small.

References

[1] C. A. Balanis. *Antenna Theory: Analysis and Design*. Wiley, second edition, 1997.

[2] S. Campione, L. K. Warne, W. L. Langston, R. A. Pfeiffer, N. Martin, J. T. Williams, R. K. Gutierrez, I. C. Reines, J. G. Huerta, and V. Q. Dang. Penetration through slots in cylindrical cavities operating at fundamental cavity modes. *IEEE Transactions on Electromagnetic Compatibility*, 62(5):1980–1988, 2020.

[3] K. H. Cavcey and D. S. Friday. Aircraft field degradation and electromagnetic compatibility. Technical Report NBSIR 88-3083, National Bureau of Standards, Boulder, CO, 1988.

[4] M. B. Higgins and D. R. Charley. Electromagnetic radiation (EMR) coupling to complex systems : aperture coupling into canonical cavities in reverberant and anechoic environments and model validation. Technical Report SAND2007-7931, Sandia National Laboratories, Albuquerque, NM, 2007.

[5] B. T. Maharaj, J. W. Wallace, M. A. Jensen, and L. P. Linde. A low-cost open-hardware wideband multiple-input–multiple-output (MIMO) wireless channel sounder. *IEEE Transactions on Instrumentation and Measurement*, 57:2283–2289, Oct. 2008.

[6] T. M. North and J. Muccioli. Automotive EMC testing — the challenges of testing battery systems for electric and hybrid vehicles. *IEEE Electromagnetic Compatibility Magazine*, 1:97–100, Jan. 2012.

[7] D. M. Pozar. *Microwave Engineering*. Wiley, fourth edition, 2012.

[8] L. K. Warne, W. A. Johnson, B. F. Zinser, W. L. Langston, R. S. Coats, I. C. Reines, J. T. Williams, L. I. Basillio, and K. C. Chen. Narrow slot algorithm. Technical Report SAND2020-3979, Sandia National Laboratories, Albuquerque, NM, 2020.

[9] J. T. Williams, I. C. Reines, L. K. Warne, R. A. Jepsen, R. K. Gutierrez, B. C. Owens, R. S. Coats, and L. I. Basilio. Combined electromagnetic and mechanical vibration environments. Technical Report SAND2018-7338C, Sandia National Laboratories, Albuquerque, NM, 2018.

DISTRIBUTION

Hardcopy—Internal

Number of Copies	Name	Org.	Mailstop
1	Technical Library	9536	0899

Email—Internal [redacted]

Name	Org.	Sandia Email Address
Technical Library	1911	sanddocs@sandia.gov

Sandia National Laboratories

Sandia National Laboratories is a multimission laboratory managed and operated by National Technology & Engineering Solutions of Sandia LLC, a wholly owned subsidiary of Honeywell International Inc., for the U.S. Department of Energy's National Nuclear Security Administration under contract DE-NA0003525.